

Alma Mater Studiorum - Università di Bologna

DOTTORATO DI RICERCA IN
GEOFISICA

Ciclo XXIX

Settore Concorsuale di afferenza: 02/C1

Settore Scientifico Disciplinare: FIS/06

Study of processes influencing short-lived
climate forcers/pollutants (black carbon and
ozone) variability in the Himalayas

Presentata da: Davide Putero

Coordinatore Dottorato:
Prof. Nadia Pinardi

Relatore:
Dr. Paolo Cristofanelli

Esame finale anno 2017

A mia mamma ed a mio zio.

Contents

Abstract	vii
1 Introduction	1
1.1 Black carbon and tropospheric ozone	1
1.2 Impacts of BC and O ₃	3
1.3 The Himalayas and south Asia: climate “hot spots”	6
1.4 Overview of the thesis	8
2 SLCF/P variability at Paknajol, Kathmandu: a “hot spot” in the Himalayan foothills	11
2.1 Introduction	12
2.2 Materials and Methods	13
2.2.1 Measurement site and instrumental setup	13
2.2.2 Back-trajectories calculation	15
2.2.3 Recurrent model analysis	15
2.3 Results	16
2.3.1 Meteorological characterization	16
2.3.2 SLCF/P seasonal and diurnal cycle	18
2.3.3 SLCF/P behavior as a function of wind direction	23
2.3.4 Correlation analysis among SLCF/P	24
2.3.5 Influence of atmospheric synoptic circulation	28
2.4 Conclusions	32

3	Comparison of SLCF/P variability at the Kathmandu “hot spot” and at the southern Himalayas	35
3.1	Introduction	36
3.2	Materials and methods	37
3.2.1	Measurement sites and instrumental setup	37
3.2.2	Satellite datasets	38
3.2.3	Back-trajectories and PBL height	39
3.3	Results	39
3.3.1	Meteorological characterization and transport patterns	39
3.3.2	BC and O ₃ variations at both stations	41
3.3.3	Effects of PBL variability on BC and O ₃ concentrations at NCO-P	43
3.4	Conclusions	47
4	STEFLUX, a tool for investigating stratospheric intrusions, and its application to NCO-P	51
4.1	Introduction	52
4.2	Experimental dataset	54
4.3	The STEFLUX tool	56
4.3.1	Description of the tool	56
4.3.2	Illustrative case study	56
4.4	Results	59
4.4.1	STEFLUX vs. SIO	59
4.4.2	Long-term evaluation of SI occurrences at NCO-P	65
4.4.3	SI influence on O ₃ and BC concentrations at NCO-P	68
4.5	Conclusions	70
5	Conclusions	73
A	Supplementary material	77
	Bibliography	81
	Acknowledgments	97

Abstract

South Asia and the Himalayas are considered among the worldwide “hot spots” for the climate impacts of air pollution. Among the atmospheric pollutants are the short-lived climate forcers/pollutants (SLCF/P), i.e., those atmospheric substances characterized by short lifetimes, with harmful effects on climate, ecosystems and human health. The high levels of the SLCF/P derive from a variety of factors, both of anthropogenic and natural origin. In this thesis, several processes affecting the variability of two key SLCF/P (i.e., black carbon, BC, and tropospheric ozone, O₃) in the southern Himalayas are investigated and discussed. The characterization of one of the “hot spots” for air pollution in the Himalayan foothills, i.e., the Kathmandu Valley, is given, by analyzing BC and O₃ variability at the Paknajol urban measurement site, over February 2013–January 2014. Since the persistent poor air quality conditions of the valley could affect a broader area, up to the high Himalayan environment, the specific role of air-mass transport from the planetary boundary layer (PBL) over the Himalayan foothills to the southern Himalayas is investigated, by comparing BC and O₃ concentrations at Paknajol and at the high altitude WMO/GAW global station Nepal Climate Observatory-Pyramid (5079 m a.s.l.). Results show that 50 % and 65 % of the BC and O₃ variability at NCO-P can be explained by PBL variations occurring over Kathmandu, in days (9 % of the period under study) in which air-mass transport between the two measurement sites is observed. Lastly, the influence of a natural process at NCO-P, i.e., stratospheric intrusions, is assessed. The application of the Stratosphere-to-Troposphere Exchange Flux tool (STEFLUX), a novel methodology based on the trajectories from the ERA-Interim reanalysis dataset, indicates that 13 % of the 2006–2013 period at NCO-P was affected by this natural phenomenon, resulting in a significant change in O₃

and BC concentrations at the measurement site.

Introduction

1.1 Black carbon and tropospheric ozone

The term short-lived climate forcers/pollutants (SLCF/P) comprises those atmospheric substances, such as black carbon (BC), ozone (O₃) and methane (CH₄), that cause health and climate impacts, and are characterized by relatively short lifetimes, as compared to those of other pollutants (such as the carbon dioxide, CO₂). In the recent years, the scientific understanding of these compounds has improved, and a lot of measures to mitigate and reduce the SLCF/P concentrations have been studied and implemented (UNEP and WMO, 2011; UNEP, 2011; Schmale et al., 2014; Stohl et al., 2015).

Both BC and tropospheric O₃ have harmful effects on the human health and the ecosystems, and contribute to climate change. As previously mentioned, they are characterized by relatively short lifetimes in the troposphere, i.e., days for BC, and days to weeks for O₃.

BC is the primary component of soot, and derives from the incomplete combustion of fossil fuel and biomass. The complete combustion would turn all the fuel into CO₂; in reality, this never happens, so that also carbon monoxide (CO), volatile organic compounds (VOCs), organic carbon (OC) and BC particles are produced along with CO₂. BC is therefore emitted from a variety of sources; the dominant emitters of BC depend strongly on the location. As presented in Bond et al. (2013), the largest BC global sources are open burning of forests and savannas (generally referred to as “biomass burning”), and residential stoves (i.e., coal and biofuel), used both for cooking and heating. These two categories together contribute up to 60 and 80 % of emissions in Asia and Africa. Diesel emissions (both on-road and off-road) contribute nearly 70 % of emissions in

Europe, North and South America. All of these categories make up nearly 90 % of total BC mass emissions. The remaining percentage is composed of emissions from aviation, shipping and flaring in the oil and gas industry (nearly 9 %), or sources with very low BC emissions (1 %). BC can constitute up to 10–15 % of fine particulate matter (UNEP and WMO, 2011), and is called “black” because BC particles strongly absorb light at all visible wavelengths. In addition to this feature, BC is also different from other forms of carbon and carbon compounds in the atmosphere because: (i) it is refractory (i.e., retains its basic forms at very high temperatures), (ii) it is insoluble in water, in organic solvents and in other compounds of atmospheric aerosol, and (iii) it exists as an aggregate of small carbon spherules (Bond et al., 2013).

O₃ is a reactive gas that exists in two layers of the atmosphere: the stratosphere (approximate extension: 15–50 km a.g.l.) and the troposphere (between ground level and 10–15 km). While the O₃ in the stratosphere (nearly 90 % of the total O₃ in the atmosphere) is considered beneficial, as it absorbs the ultraviolet (UV-B) solar radiation, the tropospheric O₃ (hereinafter referred to as O₃, for simplicity) is a harmful pollutant, the third most important anthropogenic greenhouse gas after CO₂ and CH₄. In the troposphere, O₃ is a secondary pollutant, being produced via photochemical reactions of its precursors, such as CO, CH₄, non-methane volatile organic compounds (NMVOCs), and nitrogen oxides (NO_x) (Monks et al., 2015). It is then fundamental to understand and control the emissions of O₃ precursors, to assess correct mitigation measures for the high O₃ levels in the troposphere. Primary sources for NO_x include fossil fuel combustion deriving from power generators and road transportation. For CO production, it has been estimated that deforestation, savannah and agricultural waste burning contribute up to 50 %, while fuel combustion and biomass burning in the domestic sector, and road transport, account for the remaining percentage (Fowler et al., 2008). Although the estimates for CH₄ emissions are still affected by large uncertainties, they are mostly anthropogenic, including coal mining, the coal and gas industry, landfill, ruminant animals, rice agriculture and biomass burning. Despite all of the aforementioned anthropogenic sources, NO_x are also produced naturally by bacterial and volcanic activities, and lightning. Besides O₃ production via photochemical reactions, a non-negligible source of tropospheric O₃ (up to 40 %, see Monks et al., 2015, and references therein) comes via stratospheric intrusion events (SI). These phenomena, which will be deeply investigated in Chapter 4, can be caused by a number of different synoptic- and mesoscale features. A global overview of the stratosphere-to-troposphere exchange (STE), including SI events, is depicted in Fig. 1.1: despite a global-scale circulation characterized by rising air in the tropics and large-scale subsidence in the polar regions (i.e., the Brewer-Dobson circulation), strong perturbations of the

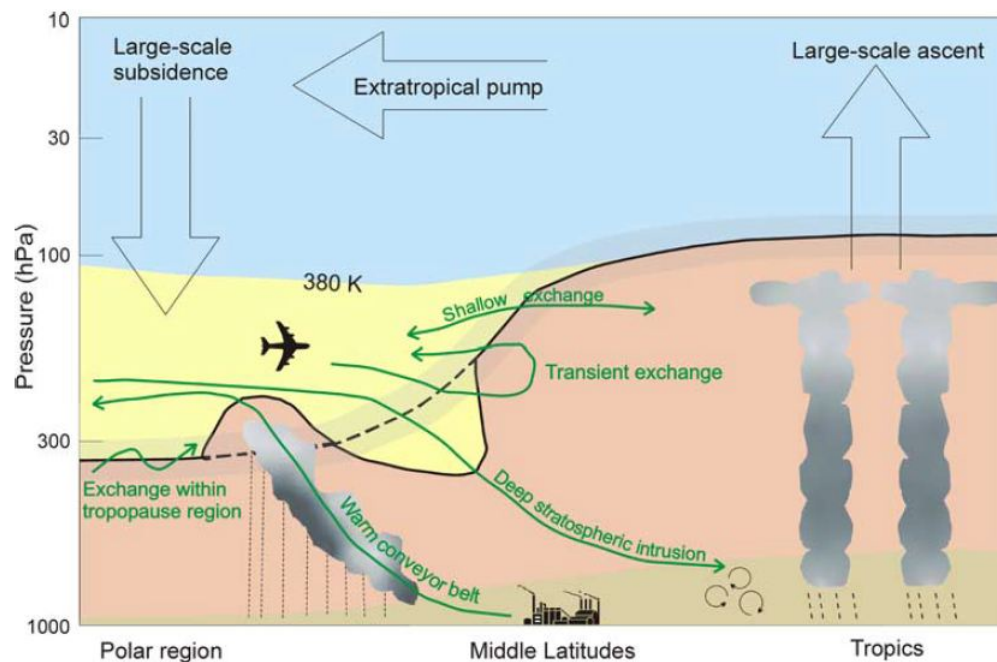


Figure 1.1: Global aspects of stratosphere-to-troposphere exchange (STE). The solid black line represents the tropopause, the blue region indicates the “overworld” (in which isentropes lie entirely in the stratosphere), the yellow area indicates the lowermost stratosphere, and the pink region identifies the troposphere (the planetary boundary layer is indicated as the brown layer). The green lines indicate all the possible exchange features, including stratospheric intrusion (SI) events. Figure taken from Stohl et al. (2003).

tropopause (the “barrier” that separates the troposphere from the stratosphere) from its average position can occur, generating the penetration of stratospheric air deep into the troposphere. SI events are capable of changing the oxidation capacity of the troposphere, and it has been estimated that the stratospheric O₃ input into the troposphere can be as large as the net photochemical production (Roelofs et al., 1997).

1.2 Impacts of BC and O₃

In this section, the BC and O₃ harmful effects on climate, ecosystems and human health are presented and discussed. Both BC and O₃ have a global warming effect on climate, as indicated by their radiative forcing values. Radiative forcing (RF), expressed in W m⁻², is the measure of how the energy balance of the Earth can

be modified, when some of the contributing climate factors are altered. Positive (negative) values of RF indicate warming (cooling) of the Earth-atmosphere climate system. Figure 1.2 shows the different components contributing to the global RF of climate between 1750 and 2011, as presented in the Fifth Assessment Report of the Intergovernmental Panel on Climate Change (IPCC, 2013).

BC causes positive RF (estimate value of $+1.1 \text{ W m}^{-2}$, see Bond et al., 2013) through direct and indirect effects; a non-negligible component of this positive RF is represented by the BC deposited on snow (median value of $+0.04 \text{ W m}^{-2}$, as reported in IPCC, 2013). In detail, the BC effects on climate can be listed as follows (for more details, see Bond et al., 2013; Gustafsson and Ramanathan, 2016):

- direct effect: BC particles absorb and scatter sunlight. The net incoming radiation is reduced because part of it is absorbed from BC, and another fraction is scattered back to space;
- indirect effect: via several complex processes, BC influences the cloud properties. The presence of BC changes the number of liquid cloud droplets, enhances changes in precipitation and lifetime of mixed-phase clouds and changes ice particle number and concentration. In addition to these processes, it has to be noted the semi-direct effect, by which BC increases the atmospheric heating rate and alters humidity profiles, consequently altering cloud distribution;
- BC deposition onto snow and ice: example of a positive feedback. By depositing on snow and ice, BC particles absorb solar radiation and thus enhance warming and melting rates.

Also tropospheric O_3 has a warming effect on climate (median value of $+0.40 \text{ W m}^{-2}$, see IPCC, 2013) and, since O_3 is a secondary pollutant, it has been estimated that two thirds of its RF may be attributed to increases in atmospheric CH_4 , while other precursors are characterized by smaller contributions to the O_3 RF (UNEP and WMO, 2011). It is interesting to note (see Fig. 1.2) that the stratospheric O_3 has an opposite behavior, leading to a cooling effect (median value of -0.05 W m^{-2} , see IPCC, 2013). As for BC, also O_3 can modify processes related to cloud formation and precipitation (Monks et al., 2015). Moreover, O_3 represents the most damaging air pollutant to agricultural crops and other plants. Its harmful effects on agriculture and vegetation include: (i) reduction in agricultural and commercial forest yields, (ii) reduced plant growth and increased plant susceptibility to disease, and (iii) long-term effects on forests and natural ecosystems, such as the climate feedback of decreasing CO_2 uptake by plants, leading to a reduction in photosynthesis (see, e.g., Mauzerall and Wang, 2001; Sinha et al., 2015).

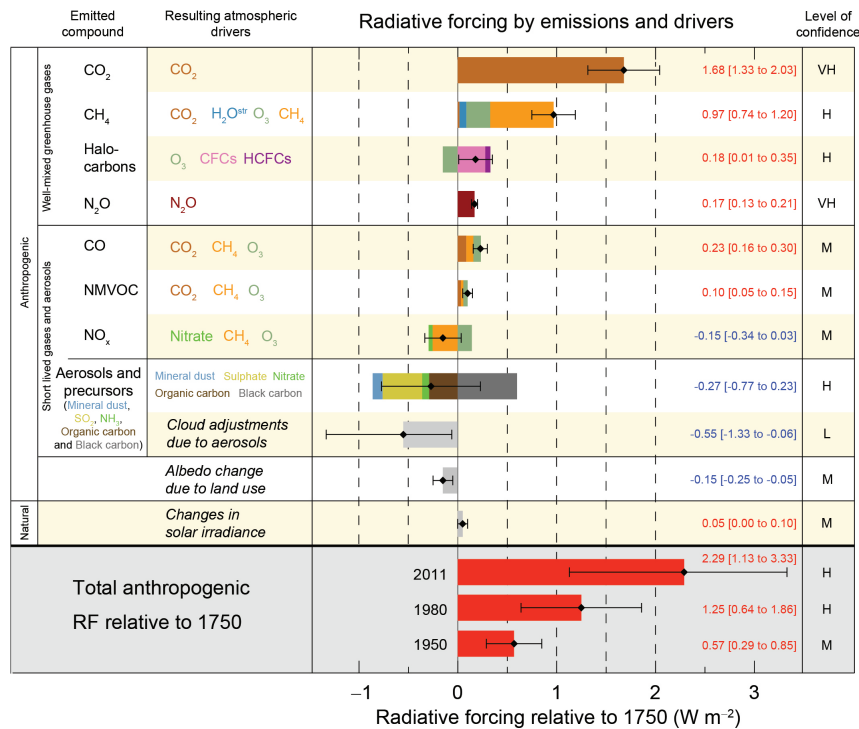


Figure 1.2: Bar chart for radiative forcing (RF) estimates in 2011 relative to 1750. The black diamonds represent the best RF estimates, with the corresponding uncertainty bars. Numerical values are provided on the right of the figure, along with the confidence level in the net forcing (VH – very high, H – high, M – medium, VL – very low). The displayed uncertainties represent the 5% and 95% confidence intervals. Figure taken from IPCC (2013).

Despite acting as positive climate forcers, BC and O₃ represent a serious threat for what concerns the human health. A systematic review of the health effects of BC is presented in Janssen et al. (2012). Epidemiological studies indicate that daily variations in BC concentrations are associated with short-term changes in health (all-cause and cardiovascular mortality, and cardiopulmonary hospital admissions). More generally, there is growing literature on these aspects, as well as on the potential benefits that may derive from the application of mitigation measures for BC (e.g., Jansen et al., 2005; Pope III et al., 2009; Anenberg et al., 2011, 2012). Often, these studies have not specifically considered BC alone, but rather it was analyzed together with particulate matter (PM), since it represents a non-negligible fraction, i.e., up to 15% (UNEP, 2011). As presented in Highwood and Kinnerson (2006), BC particles are composed of graphitic spheres of approximately 20–40 nm in diameter, aggregated in small clusters. They not only cause inflammation due to the production of free radicals, but, because of

their small size, they are also characterized by a higher rate of deposition into the lungs, resulting in a greater degree of active inhibition of phagocytosis, i.e., the process by which particles are removed from the deepest areas of the lungs (Borm et al., 2004). Moreover, BC particles can penetrate the lung lining and enter the blood, where they can have harmful effects, such as accumulation in other organs (e.g., liver, brain), increase the likelihood of thrombus formation, and increase plasma viscosity (Highwood and Kinnersley, 2006).

As for BC, O₃ has been associated to several human health effects, mostly related to the respiratory system. Because of its action as a powerful oxidizing gas, it causes oxidative stress/damage to cells in lungs once it has been inhaled (Romieu et al., 2008). The human beings react differently to O₃ exposure, and several factors affect the O₃ quantity that the organism inhales. As thoroughly reported in Fowler et al. (2008), both experimental and epidemiological studies have shed light on the O₃ effects on the human health, i.e., acute and chronic ones. Among the acute effects one can find reduced lung function, respiratory symptoms, airway inflammation and hyperactivity, and lung lining fluid antioxidant depletion; on the other hand, the chronic effects regard morphological changes in the airways and the development of asthma. In addition to this, O₃ exposure may have additional effects in combination with other environmental factors, such as pollutants, allergens, or temperature. Although the mechanisms for such effects are not fully understood, several studies have analyzed the link between short-term O₃ exposure and premature mortality (e.g., Bell et al., 2004; Levy et al., 2005; Bell et al., 2006).

1.3 The Himalayas and south Asia: climate “hot spots”

South Asia and the Himalayas are considered among the “hot spots” for the effects that air pollution has on climate. The region is often affected by wide areas of regional-scale atmospheric pollutants that extend from the Indian peninsula to the Himalayas and the Indian Ocean. This phenomenon is referred to as “Atmospheric Brown Clouds (ABC)”, after the terminology given by Ramanathan and Crutzen (2003). ABC have been extensively studied and described in a number of papers (e.g., Ramanathan and Crutzen, 2003; Ramanathan et al., 2005, 2007; Ramanathan and Carmichael, 2008; Gustafsson et al., 2009; Bonasoni et al., 2010; Engling and Gelencsér, 2010). An example of an ABC affecting the south Asian region is presented in Fig. 1.3. Here, one can clearly distinguish this huge layer of “haze”, which covers the northern India and Nepal, and can usually extend vertically up to 3 km in the dry season. ABC are composed by several pollutants: sub-micron aerosol particles and pollutant gases, such as NO_x, CO, O₃, sulphur dioxide (SO₂), ammonia (NH₃), acides, nitrates and mineral



Figure 1.3: Example of an Atmospheric Brown Cloud (ABC) extending from northern India towards the Himalayas and the Indian Ocean, occurred on December 11, 2008. The image was taken by the Moderate Resolution Imaging Spectroradiometer (MODIS) sensor on NASA Terra’s satellite.

dust. Many indoor and outdoor sources contribute to the development of the ABC: aerosol particles can be primarily emitted by (complete or incomplete) combustion processes, but can also form secondarily (the so-called secondary organic aerosol, SOA). It has been estimated that in south Asia nearly two-thirds of the observed aerosol in ABC derive from biomass burning, whereas one-third from biofuel and fossil fuel combustion (Gustafsson et al., 2009).

Being among the constituents and by-products of the ABC, and in view of the harmful effects that BC and O_3 have on climate, ecosystems and the human health (as presented in Sect. 1.2), the study of these SLCF/P becomes important in such a climate “hot spot”. As thoroughly reported in Lelieveld et al. (2015), most of the southeast Asian countries are listed in the top 25 ranked countries for premature mortality linked to air pollution. Globally, southeast Asia has the second highest premature mortality of the world, being India the main contributor (0.65 million premature deaths per year). By examining the different sources, residential and commercial energy use (referring to small combustion sources for heating and cooking, as well as waste disposal and gensets) is the leading category, contributing up to 50–60 % in India, Bangladesh, Indonesia and

Vietnam, and up to 70 % in Nepal. Secondary categories include natural sources, power generation by fossil fuel fired power plants, traffic and biomass burning.

Moreover, the Himalayas are generally referred to as the “third Pole” of the Earth, and the recent thinning of glaciers has raised concern, especially for the water supply to millions of people inhabiting the surrounding areas. Most Himalayan glaciers have retreated and lost mass since the mid-19th century; in particular, glaciers in the Mt. Everest region experienced an average mass budget of $-0.32 \pm 0.08 \text{ m yr}^{-1}$ w.e., over the period 1970–2007 (Bolch et al., 2012). One of the major factors attributed to this melting, and consequent ice mass loss, is the BC deposition onto ice and snow: the darkening effect is capable of decreasing the snow surface albedo, and likely causes glacier retreats (Flanner et al., 2007; Menon et al., 2010; Yasunari et al., 2013; Xu et al., 2016b). A recent modeling study by Ménégos et al. (2014) has estimated that BC deposition affect the Himalayan snow cover reducing its annual duration by 1 to 8 days, and that the deposited BC led to a localized warming between 0.05 and 0.3 °C, between 1998 and 2008. As presented in Hansen and Nazarenko (2004), the BC deposition onto ice and snow in south Asia can have implications for the global climate, via perturbations to the surface and planetary albedo.

This complex scenario makes it necessary to analyze the variability and the sources of such pollutants, as well as to implement efficient control measures to reduce the occurrence of such high pollution levels in these climate “hot spots”. Some recent studies (e.g., Shindell et al., 2012; Stohl et al., 2015) have shown that implementing efficient CH₄ and BC emissions reduction measures would have large benefits for the south Asian climate, health and agriculture (i.e., avoided surface temperature increases, avoided premature deaths, increase in the crop production, and decrease in the atmospheric forcing).

1.4 Overview of the thesis

In this thesis, the processes influencing BC and O₃ variability in the southern Himalayas are studied and analyzed.

First, Chapter 2 gives the complete characterization of such SLCF/P, in an area crucial for what concerns the Himalayan air quality, i.e., the Kathmandu Valley. For the first time, simultaneous measurements of BC and O₃ were performed over one year (February 2013–January 2014) at this “hot spot”, as part of one of the largest international air pollution measurement campaigns ever carried out in southern Asia (i.e., the SusKat-ABC campaign). The analyses presented in this chapter are fundamental to assess the SLCF/P variability in an area considered as a potential source region for the high levels of pollution affecting the southern Himalayas.

Chapter 3 focuses on assessing the role played by the transport of polluted air-masses from the planetary boundary layer (PBL) of the Kathmandu Valley, considered as a potential anthropogenic source area, in affecting the SLCF/P variability in the southern Himalayas. This was performed by comparing measurements collected both at Paknajol and at the Nepal Climate Observatory-Pyramid (NCO-P), a remote WMO/GAW global station sited at 5079 m a.s.l. in the high Khumbu valley, near the base camp of Mt. Everest.

The contribution of a natural process (i.e., the stratospheric intrusions, SI, as part of the stratosphere-to-troposphere exchange) on modulating O₃ and BC variability at NCO-P is assessed in Chapter 4. This was specifically done by using a tool, called STEFLUX, jointly developed during this PhD activity at CNR-ISAC and IAC-ETH in Zurich. The main purpose of STEFLUX is to obtain a fast and reliable estimation of the SI events occurring at a certain location and during a specific time window, by deploying a STE climatology, which uses as input the ERA-Interim reanalysis dataset. In this chapter, the STEFLUX outputs for the NCO-P area are compared to an observational dataset and carefully discussed; moreover, a climatological assessment of the SI events at NCO-P is provided.

Finally, the conclusions are drawn in Chapter 5.

SLCF/P variability at Paknajol, Kathmandu: a “hot spot” in the Himalayan foothills

The Kathmandu Valley in south Asia is considered as one of the global “hot spots” in terms of urban air pollution. It is facing severe air quality problems as a result of rapid urbanization and land use change, socioeconomic transformation, and high population growth. In this chapter, the first full year (February 2013–January 2014) analysis of simultaneous measurements of O₃ and BC and aerosol number concentration at Paknajol, in the city center of Kathmandu, is presented. The diurnal behavior of BC and aerosol number concentration indicated that local pollution sources represent the major contributions to air pollution in this city. In addition to photochemistry, the planetary boundary layer (PBL) evolution and wind dynamics play important roles in determining O₃ variability, as suggested by the analysis of seasonal changes of the diurnal cycles and the correlation with meteorological parameters and aerosol properties. Especially during pre-monsoon, high values of O₃ were found during the afternoon/evening. This could be related to mixing and entrainment processes between upper residual layers and the PBL. The high O₃ concentrations, in particular during pre-monsoon, appeared well related to the impact of major open vegetation fires occurring at the regional scale. On a synoptic-scale perspective,

A modified version of this chapter has been published as: Putero, D., Cristofanelli, P., Marinoni, A., Adhikary, B., Duchi, R., Shrestha, S. D., Verza, G. P., Landi, T. C., Calzolari, F., Busetto, M., Agrillo, G., Biancofiore, F., Di Carlo, P., Panday, A. K., Rupakheti, M., and Bonasoni, P.: Seasonal variation of ozone and black carbon observed at Paknajol, an urban site in the Kathmandu Valley, Nepal, *Atmos. Chem. Phys.*, 15, 13957–13971, 2015.

westerly and regional atmospheric circulations appeared to be especially conducive for the occurrence of the high BC and O₃ values. The very high values of SLCF/P, detected during the whole measurement period, indicated persisting adverse air quality conditions, dangerous for the health of over 3 million residents of the Kathmandu Valley, and the environment. Consequently, all of this information may be useful for implementing control measures to mitigate the occurrence of acute pollution levels in the Kathmandu Valley and surrounding area.

2.1 Introduction

The Kathmandu Valley in Nepal, the largest metropolitan region at the Himalayan foothills (one of the most polluted but still least sampled regions of the world), represents one of the regional hot spots in terms of air pollution. This area, having a cross section of about 20 km north to south and 30 km east to west, comprises of three administrative districts, Kathmandu, Lalitpur and Bhaktapur, and has undergone rapid but unplanned urbanization due to high population growth, dramatic land use changes and socioeconomic transformation, thus facing severe air pollution problems. Over the past quarter century the Kathmandu Valley's population has quadrupled to more than 3 million. Between 1990 and 2014 the total vehicle fleet grew from 45,871 to more than 700,000, with the number of motorcycles having the highest annual growth rate of 16 % during the period (Faiz et al., 2006; Shrestha et al., 2013). Furthermore, by using an energy system model, Shrestha and Rajbhandari (2010) indicated that the total energy consumption in the Kathmandu Valley is expected to increase at an average annual growth rate of 3.2 % in the period ranging from 2005 to 2050. By 2050, there will be an increase in the energy consumption of 30 %, 25 % and 22 % for the shares of transport, industrial and commercial sectors, respectively. In the Kathmandu city center the air quality is so bad that Nepal's own national ambient air quality standards are only met on about 40 days per year; during the rest of the period the particulate matter exceeds the national limit considered harmful. The Kathmandu Valley sizable emission of air pollutants is of concern for local and regional air quality and climate; however, it is still a manageable size in terms of potential interventions to address serious air pollution problems in the valley. The relative importance of local and regional emission sources has not been well quantified yet, making it difficult to design mitigation strategies that will have a large impact and still be cost-effective. Therefore, an improved scientific understanding of the main sources and impacts of air pollution in the region is a prerequisite for designing effective mitigation options.

In the recent past, a few studies have presented measurements of various

atmospheric compounds in the Kathmandu Valley (e.g., Sharma et al., 2012; Panday and Prinn, 2009; Panday et al., 2009; Pudasainee et al., 2006; Giri et al., 2006; Sharma, 1997; Shrestha and Malla, 1996), all suggesting that air pollution in Kathmandu has harmful effects on human health (leading to bronchitis, throat and chest diseases), crop productivity and also tourism income in Nepal, being Kathmandu the heart of the Nepalese culture, art and architecture. However, none of them presented simultaneous observations of key SLCF/P across seasons.

In order to provide continuous measurements of atmospheric composition variability, a measurement site was installed in 2013 at Paknajol, in the tourist area of the Kathmandu city. This has enabled us to achieve a more comprehensive understanding of the dynamics of air pollution and related emissions in the Kathmandu Valley, and to constitute the scientific basis in order to support the local implementation of mitigation actions. These measurements were carried out as part of the SusKat-ABC (A Sustainable Atmosphere for the Kathmandu Valley – Atmospheric Brown Cloud) campaign in Nepal, the second largest international air pollution measurement campaign ever carried out in southern Asia, which aim is to provide the most detailed air pollution measurements to date for the Kathmandu Valley and the surrounding region (Rupakheti et al., 2017).

2.2 Materials and Methods

2.2.1 Measurement site and instrumental setup

Kathmandu city is located in a broad basin at the foothills of the central Himalayas, with valley floor at an average altitude of 1300 m a.s.l. The mountains surrounding the valley have peaks ranging from 2000 to 2800 m a.s.l. Neighboring valleys to the west, north, northeast and south have substantially lower elevations. The Kathmandu Valley's meteorology is influenced by large scale features, i.e., western disturbances and the south Asian summer monsoon, as well as local mountain-valley circulations. As reported by Panday and Prinn (2009) and Panday et al. (2009) during the dry season the diurnal cycle of air pollutants (CO , O_3 , PM_{10}) is strongly affected by local meteorology connected to the evolution of the convective planetary boundary layer (PBL) and thermal wind flows along the flanks of the mountains surrounding the valley.

The Paknajol site is located ($27^{\circ}43'4''$ N, $85^{\circ}18'32''$ E, 1380 m a.s.l.) near the edge of Kathmandu's tourist district of Thamel. The sampling site stands on the terrace (about 25 m a.g.l.) of the Ev-K2-CNR representative office. This is the highest building in the block, thus having a 360° free horizon of at least 300 m. The instruments are located in an air-conditioned room, in order to maintain the

correct operating conditions; an UPS for uninterruptible power supply guarantees the continuous measurements in case of (frequent) blackout events, up to 18 hours a day power cut, especially during the winter months. The sampling heads are placed on the roof just outside this room. The measurement activities, including aerosol and trace gas measurements, were started on February 2013.

The following instruments are used for continuous measurements:

1. UV-absorption analyzer (TEI 49i, Thermo Environmental) is used to collect surface O₃ measurements. These are referred to the WMO/GAW reference scale (SRP#15, see Klausen et al., 2003) hosted at the GAW World Calibration Centre (WCC) at EMPA (Switzerland), via direct comparison with the CNR-ISAC laboratory standard hosted at the Mt. Cimone WMO/GAW global station (Italy). The experimental setup is similar to that described in Cristofanelli et al. (2010).
2. Aerosol light absorption and BC, derived by using the mass absorption efficiency of $6.5 \text{ m}^2 \text{ g}^{-1}$, are measured through a Multi-Angle Absorption Photometer (MAAP 5012, Thermo Electron Corporation). For more details, see Marinoni et al. (2010). The correction described in Hyvärinen et al. (2013) for the measurement artifact, affecting the instrument's accuracy at high BC concentrations, was applied. A PM₁₀ cutoff size was used in the sampling head.
3. Meteorological parameters (atmospheric pressure and temperature, wind speed and direction, relative humidity and precipitation) are monitored using an automatic weather station (WXT 425, VAISALA). Global solar radiation is monitored with a pyranometer (CMP21, Kipp&Zonen).
4. Aerosol number concentration and size distribution (in the range $0.28 \mu\text{m} \leq D_p < 10 \mu\text{m}$, D_p being the geometric diameter of particles) are measured using an Optical Particle Counter (OPC Monitor, FAI Instruments), which uses laser light scattering technique ($\lambda=780 \text{ nm}$). The OPC optical diameters (divided in 8 bins) are then converted into geometric diameters, assuming that particles are spherical. In order to minimize biases related to coincidence errors, but also to reduce relative humidity and dry aerosol particles, the air sample is subjected to a dilution process, whose dilution factor can be varied, by modifying the dilution flow rate (from 0 to 4 L min^{-1}).
5. On-line PM₁₀ and PM₁ are measured (with a 24 h resolution), using the β -absorption technique, with a medium-volume ($2.3 \text{ m}^3 \text{ h}^{-1}$) sampler (SWAM Dual Channel, FAI Instruments). The instrument is equipped with two 12V

back-up batteries, in order to complete measurements in case of electricity power breaks. From 1 April 2013 a PM₁ sampling head has been installed, replacing the PM_{2.5} one.

All measurements presented in this chapter refer to Nepal Standard Time (NST, UTC+05:45); data are stored and fully validated on a 1-min basis, then averaged to a common time base of 60 minutes, and expressed in STP (0 °C and 1013 hPa) conditions. With the purpose of aggregating data to hourly average values, 50 % data coverage criteria was used, i.e., at least 50 % coverage of the data sampling period was required to give a 1-h average.

2.2.2 Back-trajectories calculation

In order to describe the synoptic-scale atmospheric circulation scenarios over the Kathmandu Valley and the surrounding region, isentropic 5-day back-trajectories have been used, computed by the HYSPLIT model (Draxler and Hess, 1998) every 6 h (at 05:45, 11:45, 17:45, and 23:45 NST). With the aim of minimizing the effect of the complex topography and to provide a description of the large-scale circulation in the free troposphere, calculations were initialized at 600 hPa. The model calculations are based on the Global Data Assimilation System (GDAS) meteorological field produced by NCEP Reanalysis data, with a horizontal resolution of 1° × 1°. In order to aggregate the back-trajectories of common origin, and better characterize the synoptic-scale circulation occurring at Paknajol, a cluster aggregation technique (Draxler et al., 1999) has been applied to the back-trajectories. Basically, at each step of the process, the appropriate number of clusters was identified, based on the variations of several statistical parameters; by maximizing between-group variance and minimizing within-group variance, this methodology might identify similar air-mass back-trajectories and aggregate them.

2.2.3 Recurrent model analysis

To understand how photochemistry and atmospheric dynamics affect the variation of O₃ mixing ratios and to comprehend the origin of elevated O₃ levels in the afternoon and evening hours during the pre-monsoon period, a recurrent neural network model set up by University of L'Aquila was used. These models allow us to simulate the nonlinear relationship between O₃ and meteorological parameters that are proxies of photochemistry and dynamics (Lönblad et al., 1992; Elman, 1990). Considering the strong role of meteorological conditions and photochemistry on the variations of O₃ mixing ratios (Pudasainee et al., 2006; Di Carlo et al., 2007), and the fact that synoptic-scale meteorological effects

Table 2.1: Onset and decay dates of the different seasons for the period February 2013 – January 2014.

Season	Start day–end day
Pre-monsoon	1 February–12 May 2013
Monsoon	13 May–6 October 2013
Post-monsoon	7 October–26 October 2013
Winter	27 October 2013–31 January 2014

usually last for more than 1 day, the most complex architecture of the neural network that uses the recurrent approach takes into account the multi-day effect of meteorology, as well as diurnal boundary layer cycles (Biancofiore et al., 2015). The model uses the observed pressure, temperature, RH, solar radiation, wind velocity and direction, and BC concentrations as input to simulate the O₃ mixing ratio (Biancofiore et al., 2015). The inclusion of a sub-group of these proxies allows us to distinguish between the role of dynamics and that of photochemistry and local emissions (BC) in the observed variations of O₃ mixing ratio.

2.3 Results

2.3.1 Meteorological characterization

The Paknajol area is strongly influenced by local traffic and urban emissions, as it is located near the edge of Kathmandu’s tourist center, and near a major thoroughfare. Meteorological observations at the sampling site help in better describing the seasonal and diurnal variability of the air pollutants and SLCF/P in the Kathmandu Valley.

With the aim of identifying the regional transition of the monsoon seasonal regimes, meteorological observations carried out at the Nepal Climate Observatory-Pyramid (NCO-P, 5079 m a.s.l., Khumbu Valley, Nepal) were considered. As shown by Bonasoni et al. (2010), the variability of meteorological parameters (i.e., RH and meridional wind component) observed at NCO-P can be used to derive the onset and withdrawal dates of the different seasons on the south side of the Himalayan range (where NCO-P is located). Moreover, as described in the annual report of the India Meteorological Department (IMD, 2014), the seasonal advance of the south Asian monsoon cycle did not differ too much between the location of NCO-P and Kathmandu. Table 2.1 reports the start and withdrawal dates of each season (pre-monsoon, monsoon, post-monsoon, winter) for the period considered in this study.

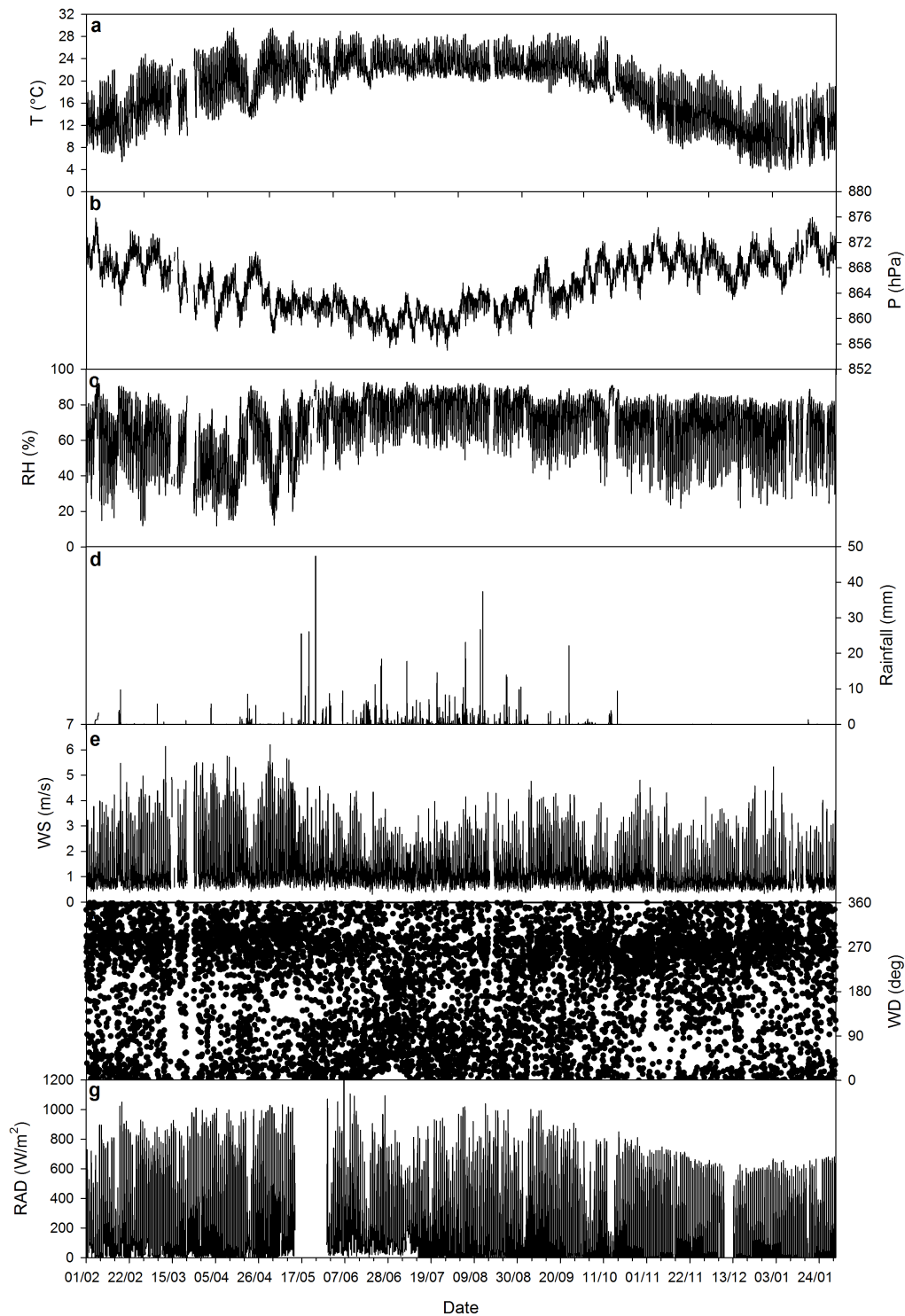


Figure 2.1: Time series of hourly atmospheric temperature (T , panel a), pressure (P , panel b), relative humidity (RH , panel c), precipitation (d), wind speed (WS , panel e), wind direction (WD , panel f) and solar radiation (RAD , panel g) measured at Paknajol.

Figure 2.1 shows the variability of the meteorological parameters measured at Paknajol from February 2013 to the end of January 2014. Hourly atmospheric temperature (T, Fig. 2.1a) values never exceeded 29.5 °C, while minima never dropped below 3.5 °C. Over the whole measurement period, T had an average value of 18.7 ± 5.6 °C (hereinafter, average values are indicated as average \pm 1 standard deviation). T was characterized by an evident diurnal cycle, with values peaking in the middle of the day and a minimum in the early morning. Atmospheric pressure (P, Fig. 2.1b, average value: 865.3 ± 4.1 hPa) showed its minimum values during the summer season, which is characterized by the presence of the monsoon trough over Nepal, accompanied by frequent and intense showers, reaching up to 47 mm h^{-1} (Fig. 2.1d). P is characterized by a semi-diurnal cycle, with two minima (at 04:00 and 16:00) and two maxima (at 10:00 and 22:00), with average amplitudes ranging from 1.2 hPa (pre-monsoon) to 3.5 hPa (post-monsoon). RH values (Fig. 2.1c, average value: 67.1 ± 17.0 %) were high during all of the measurement period, rarely decreasing below 20 % (50 % during the summer monsoon season); it has to be noted that during winter, RH values swing from very high to very low, thus presenting the widest diurnal cycle among all of the seasons. Saturation conditions (RH equal to 95 % or higher) were mainly reached during the most intense rainfalls. In agreement with rainfall reported in Panday and Prinn (2009), about 90 % of annual rainfall was observed during June–August. Figures 2.1e and 2.1f show wind speed and direction, respectively. The sampling site was characterized by low wind speeds, with the majority of winds from the W–NW sector and a secondary contribution from the W–SW sector (see Fig. A.1, Supplement). As shown in Panday and Prinn (2009) and Panday et al. (2009), nights were characterized by low wind speeds (maximum speed: 4 m s^{-1}) coming from several directions, mainly explained by katabatic winds descending from the mountain slopes at the edge of the Kathmandu Valley rim; however, during the afternoon, stronger winds (reaching up to 6.5 m s^{-1}) occurred at the measurement site, which was swept by westerly/northwesterly winds which entered through the western passes.

2.3.2 SLCF/P seasonal and diurnal cycle

The hourly average (along with daily averages) time series for O₃, BC, and particle number concentration are shown in Fig. 2.2. Figure 2.3 shows the diurnal variability of these pollutants across the seasons, while seasonal average values are presented in Table 2.2.

Similarly to other polluted cities, the rush hours and PBL dynamics result in the distinct morning and evening peaks: an increase in traffic activities and congestion, an increase in emissions from cooling/heating activities (LPG, kerosene,

Table 2.2: Average values (\pm standard deviation) of the pollutants, computed for the different seasons selected by the periods of Table 2.1 (PRE-M: pre-monsoon, MON: monsoon, POS-M: post-monsoon, WIN: winter, and ALL: the whole measurement period).

	O ₃ (nmol mol ⁻¹)	BC ($\mu\text{g m}^{-3}$)	Accum. (no. cm ⁻³)	Coarse (no. cm ⁻³)	PM ₁ ($\mu\text{g m}^{-3}$)	PM ₁₀ ($\mu\text{g m}^{-3}$)
PRE-M	38.0 \pm 25.6	14.5 \pm 10.4	668 \pm 383	4.2 \pm 2.5	98 \pm 83	241 \pm 134
MON	24.9 \pm 16.5	6.3 \pm 3.8	250 \pm 141	1.9 \pm 1.1	32 \pm 12	107 \pm 37
POS-M	22.8 \pm 17.0	6.2 \pm 3.9	–	–	26 \pm 10	101 \pm 38
WIN	20.0 \pm 19.8	18.3 \pm 14.1	–	–	74 \pm 26	320 \pm 75
ALL	27.0 \pm 21.3	11.6 \pm 10.7	505 \pm 372	3.3 \pm 2.4	48 \pm 42	169 \pm 113

and firewood), as well as a decrease in the PBL height. The primary emission indicators, i.e., BC and aerosol particle number, reveal such activities. Industries, especially brick kilns, and open garbage burning also contribute to poor air quality in the Kathmandu Valley.

The average value of BC (Fig. 2.2a) over the whole measurement period was $11.6 \pm 10.7 \mu\text{g m}^{-3}$. The highest BC concentrations were observed during pre-monsoon and winter seasons (Table 2.2), with daily values often exceeding $20 \mu\text{g m}^{-3}$; while the lowest values occurred during the monsoon season (the lowest daily value recorded was $2.5 \mu\text{g m}^{-3}$). These levels are slightly higher than what is reported in a previous study by Sharma et al. (2012) at Pulchowk Campus, in which they reported an average BC of $8.4 \pm 5.1 \mu\text{g m}^{-3}$, over a year-long study period spanning between May 2009 and April 2010. Another study by Shrestha et al. (2010) reported far lower values of elemental carbon concentration ($1.7 \pm 0.6 \mu\text{g m}^{-3}$) for an urban site 30 km southeast (downwind) of the Kathmandu Valley, during the 2009 pre-monsoon season. The highest seasonal values, observed during winter/pre-monsoon, can be attributed to several factors: an increase in emissions from domestic heating, the use of small but numerous gensets during extended hours with power cuts, the operation of over 100 brick kilns in the valley, garbage burning, as well as lower PBL and lower wet deposition of pollutants in winter months compared to the summer months with intense heat and rainfall. The average diurnal variation in BC concentrations in the different seasons is shown in Fig. 2.3a. The typical diurnal variation for BC, as also shown in Sharma et al. (2012), reflects the BC profile for an urban site, presenting two daily maxima, with a prominent peak in the morning (between 07:00 and 08:00), and a second one in the evening (between 20:00 and 21:00), as well as two minima at night (between 01:00 and 02:00) and in the afternoon (between 14:00 and 15:00). These two daily peaks reveal the start and build-up of emissions due to local anthropogenic activities, such as traffic and cooking activities. Moreover, also a meteorological component

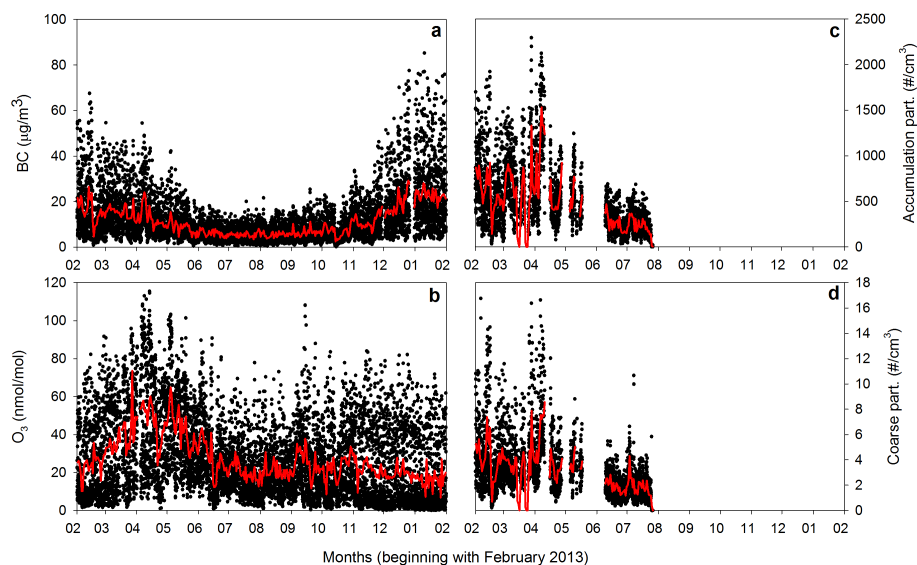


Figure 2.2: Time series of hourly concentrations of equivalent black carbon (a), surface ozone (b), accumulation (c), and coarse particles (d) recorded at Paknajol. Red lines denote daily averages.

cannot be ignored: this is due to the presence of katabatic winds that lead to the uplift of surface polluted air-masses during the night. The following build-up of the morning mixed layer favors the downward mixing of pollutants back to the bottom of the valley (Panday and Prinn, 2009; Panday et al., 2009). This diurnal cycle was observed in all four seasons but the peak values were much higher in winter and pre-monsoon seasons (morning peaks: 41.4 and $33.3 \mu\text{g m}^{-3}$, respectively) compared to the post-monsoon and monsoon seasons (12.9 and $11.4 \mu\text{g m}^{-3}$, respectively).

Surface ozone (O_3) had an average value of $27.0 \pm 21.3 \text{ nmol mol}^{-1}$ (1 nmol mol^{-1} is equivalent to 1 ppb) over the whole measurement period (Fig. 2.2b). The highest O_3 was observed during the pre-monsoon season, while the lowest values were reached during the winter season (Table 2.2). This spring peak is a feature widely present in south Asia and the Himalayas (see e.g., Cristofanelli et al., 2010; Agrawal et al., 2008). Pudasainee et al. (2006), using measurements made at Lalitpur, an adjacent city to the Kathmandu municipality, suggested that variations of solar radiation, ambient temperature, and precursors (such as NO_x and VOCs) can together explain 93 % of the variation in measured ground level O_3 at Kathmandu. Following Chevalier et al. (2007), with the aim of attributing the fraction of O_3 , BC, accumulation, and coarse particles variability related to day-to-day and diurnal-scale processes, the ratio of daily/hourly standard

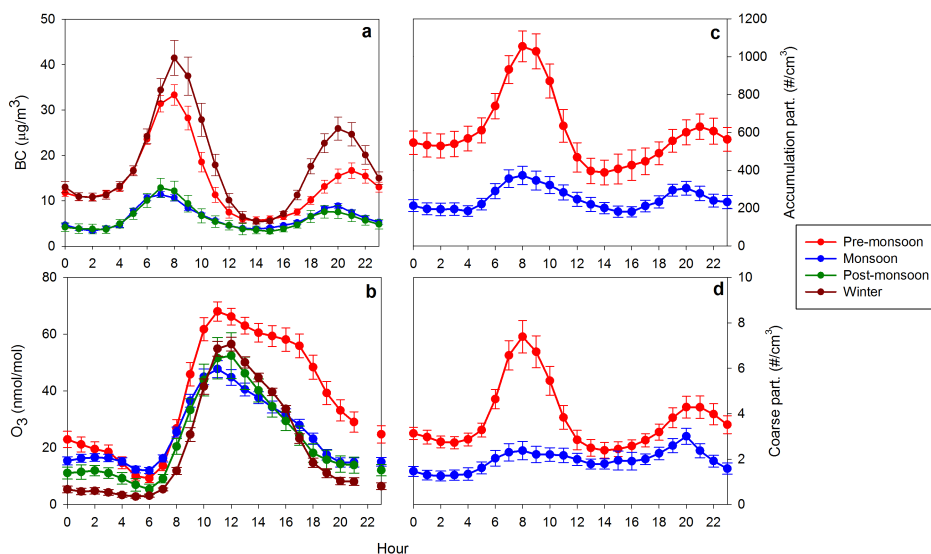


Figure 2.3: Average seasonal diurnal variation for equivalent black carbon (a), surface ozone (b), accumulation (c), and coarse particles (d) recorded at Paknajol. The error bars denote the expanded uncertainties ($p < 0.05$) of the mean.

deviations was calculated. The obtained values (0.54 for O_3 , 0.59 for BC, 0.81 for accumulation, and 0.71 for coarse particles) indicated that both diurnal and day-to-day variations are important to explain O_3 , BC, and particle number variations at Paknajol. O_3 diurnal variation is shown in Fig. 2.3b: a peak in O_3 mixing ratios characterized the central part of the day (between 11:00 and 13:00), while a minimum was observed in the morning (between 05:00 and 06:00). This diurnal variation is typical for polluted urban sites (Jacobson, 2002) and can be explained in terms of local O_3 photochemistry production and removal processes as well as PBL dynamic and vertical air-mass mixing, as discussed in Sect. 2.3.4.

Particle number concentrations of accumulation ($0.28 \mu\text{m} \leq D_p < 1 \mu\text{m}$) and coarse ($1 \mu\text{m} \leq D_p < 10 \mu\text{m}$) particles are reported in Fig. 2.2 (panels c and d, respectively). Unfortunately, due to instrumental failures, no measurements were available after 27 July 2013; only two seasons were covered, i.e., pre-monsoon and monsoon. The average values over the available time period were $505 \pm 372 \text{ cm}^{-3}$ for the accumulation particles and $3.3 \pm 2.4 \text{ cm}^{-3}$ for the coarse particles. Accumulation and coarse particle concentrations were high during the pre-monsoon season and far lower during the monsoon (Table 2.2). The average seasonal diurnal cycles (Fig. 2.3c for accumulation and Fig. 2.3d for coarse) were somewhat similar to that of BC, presenting two daily peaks, in correspondence to the start of working activities and traffic rush hours, thus

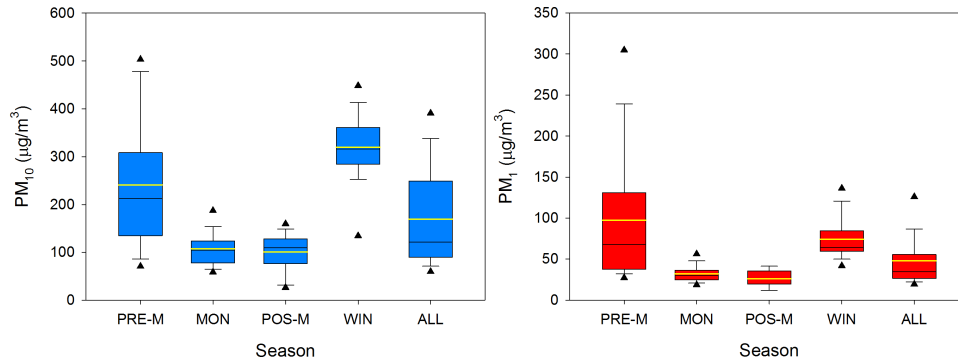


Figure 2.4: Box-and-whisker plot for PM_{10} (left panel) and PM_1 (right panel) concentrations at Paknajol, segregated by season (PRE-M: pre-monsoon, MON: monsoon, POS-M: post-monsoon, WIN: winter, and ALL: the whole measurement period). The boxes and whiskers denote the 10th, 25th, 75th, and 90th percentiles of PM values; triangles denote the 5th and 95th percentiles. The median (mean) value is denoted by the black (yellow) line.

indicating common anthropogenic emission sources and similar meteorological influences. The similar behavior between accumulation and coarse particle number concentrations suggests likely common origins, indicating that the main fraction of coarse particles is linked to the resuspension of road dust or ash from local combustion and not to mineral dust transport from desert areas of the Indo-Gangetic Plain (Duchi et al., 2014). During the pre-monsoon, the morning peak was higher (1054 cm^{-3} for accumulation and 7.4 cm^{-3} for coarse) than the one recorded in the evening (629 and 4.3 cm^{-3} , respectively). The same was true for the accumulation mode even during the monsoon season, although the difference between the two peaks showed smaller amplitude. For coarse particles, however, the evening peak appeared to be higher than the morning peak during the wet season. This can be possibly explained by considering the wet conditions which usually characterized Kathmandu during nighttime in this season; moreover, it has to be noted that this phenomenon may be combined with aerosol drying from the dilution system of the OPC that is not sufficient. Most of the rain occurs during the nighttime, and the wet surface in the early morning prevents emission of roadside dust and soil. As the day evolves, moisture is more efficiently evaporated, leaving dry dust and soil to be resuspended by traffic or winds, thus leading to the appearance of a larger evening peak for coarse particle number.

Figure 2.4 shows the seasonal box-and-whisker plot for PM_{10} and PM_1 recorded at Paknajol. Prior to 1 April 2013, a $PM_{2.5}$ sampling head was installed

in place of the PM_{10} one. By considering the whole sampling period, PM_{10} had an average value of $169 \pm 113 \mu\text{g m}^{-3}$, which is comparable to the value found by Giri et al. (2006), $133.7 \pm 70.3 \mu\text{g m}^{-3}$, computed over the period 2003–2005 for the Thamel measurement site (not far from Paknajol), or to the values found in Aryal et al. (2008), which range from 170 to $230 \mu\text{g m}^{-3}$ (annual averages) for two busy traffic area stations in Kathmandu. Our value appears slightly higher than those of Giri et al. (2006). This is in line with the increasing urbanization and the growth of the total vehicle fleet which occurred in the Kathmandu Valley. The maximum seasonal average of PM_{10} was found during winter, while minima occurred during monsoon and post-monsoon seasons (Table 2.2). $PM_{2.5}$ presented an average value of $195 \pm 83 \mu\text{g m}^{-3}$ over its short time period (17 days), while PM_{10} had an average value of $48 \pm 42 \mu\text{g m}^{-3}$, with the maximum values during the pre-monsoon and winter seasons and significantly lower values during monsoon and post-monsoon (Table 2.2). Over the whole measurement period, the ratio $PM_{10} / PM_{2.5}$ was 0.29 ± 0.10 , indicating a large contribution of coarse particles to the total aerosol mass. This aerosol mass concentration ratio, whose values were the highest during the pre-monsoon (0.39 ± 0.09) and lowest during winter (0.21 ± 0.05), is similar to the ratios observed for arid sites (Shahsavani et al., 2012; Lundgren et al., 1996), for sites affected both by dust storms originating in Asia (Claiborn et al., 2000), strong African dust outbreak episodes (Alastuey et al., 2005), and dusty roads (Colbeck et al., 2011). Similar ratios were observed also in other large municipalities in south Asia, such as Bilaspur (0.24, Deshmukh et al., 2010) or Raipur (0.28, Deshmukh et al., 2013) in India, or Nanjing (0.34, Wang et al., 2003) in China. In the European cities this ratio is generally higher than in Asia.

2.3.3 SLCF/P behavior as a function of wind direction

The wind sector which mostly contributed to the occurrence of high SLCF/P values at the measurement site was highlighted, as presented in Fig. 2.5. Here, the angular distribution of the pollutants averaged over WD intervals of 10° (green lines) is shown. Also reported in the figure are the distributions of the frequency of wind directions (blue) and the relative abundance of the pollutants (red), weighted by the wind directions, computed according to Gilge et al. (2010). These analyses refer to the whole investigation period and no significant differences were observed, neither by categorizing data as a function of the different seasons, nor by the time of day. WD behavior has already been presented in Sect. 2.3.1; BC and aerosol particle number (both accumulation and coarse) average values did not show any dependence as a function of wind direction. This is conceivable considering that Paknajol is located in the middle of several pollution sources. O_3 angular mean values (green line) showed enhanced values from the W–NW

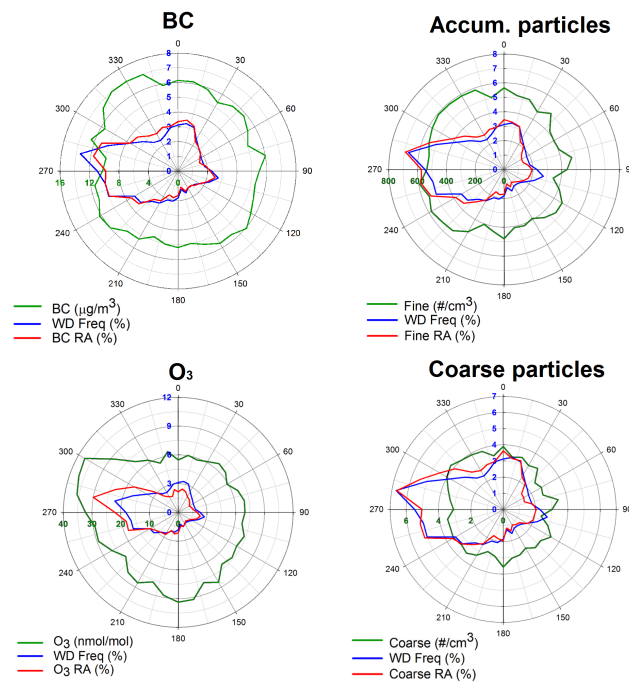


Figure 2.5: Relation between BC, O₃ (left column), accumulation, and coarse particles (right column), and wind direction for Paknajol. The green line represents the mean of the respective pollutant per 10° WD interval, the blue line is the relative frequency of WD, and the red line is the relative abundance of the chosen pollutant, weighted by the WD frequency, as explained in Gilje et al. (2010).

sector (35 nmol mol^{-1} on average). This leads to a small distortion of the O₃ contribution away from the distribution of the wind directions (peaking at 270°). 48 % of the total O₃ recorded at Paknajol station was enclosed in the 240–320° wind sector, which perfectly matches the direction from a mountain pass from where, according to Panday and Prinn (2009), air-masses can be transported during daytime towards Kathmandu due to thermal transport, indicating the arrival of regional polluted air-masses.

2.3.4 Correlation analysis among SLCF/P

By looking at the diurnal variations presented in Fig. 2.3, the first peak in BC and aerosol particles can be explained in terms of increased emission (traffic and cooking activity) under atmospheric stable conditions and low PBL height or with an additional contribution of down-mixing as the nighttime stable boundary layer breaks up (Panday and Prinn, 2009). Dilution within the higher PBL, arrival

Table 2.3: Correlation coefficients (r) between several parameters (BC, O₃, accumulation and coarse particles, WS, T, and solar radiation (RAD)) for hourly and daily (in parentheses) values, over the whole sampling period.

	O ₃	BC	Acc.	Coarse	WS	T	RAD
O ₃	–	–0.21 (–0.04)	0.11 (0.43)	0.07 (0.41)	0.54 (0.65)	0.51 (0.32)	0.71 (0.56)
BC	–0.21 (–0.04)	–	0.86 (0.78)	0.87 (0.74)	–0.35 (–0.21)	–0.56 (–0.58)	–0.10 (–0.15)
Acc.	0.11 (0.43)	0.86 (0.78)	–	0.86 (0.91)	–0.22 (0.12)	–0.39 (–0.38)	–0.02 (–0.06)
Coarse	0.07 (0.41)	0.87 (0.74)	0.86 (0.91)	–	–0.21 (0.18)	–0.31 (–0.35)	–0.07 (–0.03)
WS	0.54 (0.65)	–0.35 (–0.21)	–0.22 (0.12)	–0.21 (0.18)	–	0.45 (0.41)	0.40 (0.56)
T	0.51 (0.32)	–0.56 (–0.78)	–0.39 (–0.38)	–0.31 (–0.35)	0.45 (0.41)	–	0.43 (0.31)
RAD	0.71 (0.56)	–0.10 (–0.15)	–0.02 (–0.06)	–0.01 (–0.03)	0.40 (0.56)	0.43 (0.31)	–

of cleaner air from west of the Kathmandu Valley, and decrease of emissions can explain the daily minimum in aerosol and BC observed from 11:00 to 17:00. Conversely, the peak in O₃ can be explained in terms of enhanced photochemical production (with respect to nighttime or early morning), as well as in terms of downward vertical mixing of polluted regional air-masses from the free troposphere or the nighttime residual layer. When the PBL height starts to decline due to the diurnal decrease of solar radiation and soil heating, along with the increased emissions of evening traffic and cooking activities, a secondary peak in BC aerosol is observed from 18:00 to 22:00. Titration with NO, dry deposition, and less efficient vertical mixing within a more stable PBL lead to the decrease of O₃ which finally results in the nighttime minimum, when BC and aerosol particles also present the lowest concentrations due to the decrease of traffic and domestic emissions. Moreover, since measurements were taken on the roof of a tall building, in the presence of a stable nighttime atmosphere, it may be difficult to capture near-surface pollution. These behaviors led to a negative correlation between hourly BC and O₃ (Table 2.3), which was almost constant over all of the considered seasons. The O₃ decrease after the noon peak was faster during winter and post-monsoon seasons, while it was more gradual during pre-monsoon and monsoon. Moreover, during the pre-monsoon season, a “bump” in O₃ mixing ratios (>50 nmol mol^{–1}) was observed during the afternoon (between 11:00 and 17:00; Fig. 2.3). The simultaneous decreases of BC and aerosol particle concentrations support a strong role of downward vertical mixing in enhancing O₃ and decreasing primary pollutants (BC and aerosol particles). The important role of dynamics in influencing SLCF/P variability is confirmed by the negative (positive) correlation between wind speed and BC (O₃). The correlation coefficients (r) are higher by considering daily average values (Table 2.3), supporting the role of day-to-day meteorology in influencing the SLCF/P.

BC showed significantly higher hourly correlation with accumulation and coarse particles (0.86 and 0.87, respectively), which was lower during the wet season (0.66), strongly supporting common sources and processes that influence their variability (i.e., traffic sources and PBL dynamics). The lower summer

correlation can be explained in terms of different hygroscopicities of BC with respect to other aerosol particles (see Marinoni et al., 2010), which can lead to a lower scavenging efficiency of BC, with respect to other inorganic and organic species, that has been proved especially for non-aged BC (Cozic et al., 2007). Due to the lack of data, no information about the variation of the correlation coefficients computed between accumulation and coarse particles could be given other than during pre-monsoon and monsoon seasons. The high correlation coefficient between BC and accumulation (and coarse) particles could however indicate that BC can be used as an indicator of primary pollution, even when measurements by the OPC are lacking.

O₃ showed high correlation with solar radiation (0.71 for hourly and 0.56 for daily values) and temperature, which is considered as a proxy for seasons (0.51 and 0.32); this is somewhat expected for an urban site like Kathmandu, where photochemistry and PBL dynamics (indirectly driven by solar radiation and temperature behavior) play an important role in determining O₃ variability (Pudasainee et al., 2006). The correlation with solar radiation exhibited some variability during the year, giving the lowest values (0.59 for hourly values and 0.06 for daily values) during the pre-monsoon season, possibly supporting the enhanced role of atmospheric transport and dynamics in influencing O₃ with respect to photochemistry. Apparently, this agrees only in part with the results shown in Pudasainee et al. (2006), in which the authors argued that the “flat peak” in O₃ concentrations during the pre-monsoon is mainly due to abundance of solar radiation and higher temperature (justified by high correlation coefficient values).

In order to distinguish the chemical effects from the boundary layer dynamics, the correlation coefficients limiting the data to convective hours only (i.e., between 11:00 and 17:00, according to the wind speed and solar radiation diurnal variations) were also computed. The slightly weaker correlation between BC and accumulation particle number and, conversely, the increase in correlation between O₃ and accumulation particle number, may indicate the role of other processes (e.g., secondary aerosol production) occurring in the air-masses which characterize this specific time span (Table A.1, Supplement). In particular, it is likely that aged air-masses rich in secondary pollutants (i.e., O₃ and aerosol) can be transported to the measurement site in the afternoon mixed layer (see also Sect. 2.3.5).

Mixing processes with upper residual O₃ layers can explain this behavior. Sensitivity tests with a recurrent neural network model, using different subgroups of proxies, have been carried out and the results are shown in Fig. 2.6, where the observed and different simulated average diurnal O₃ mixing ratios are compared. The simulation that included all the proxies reproduced the observed

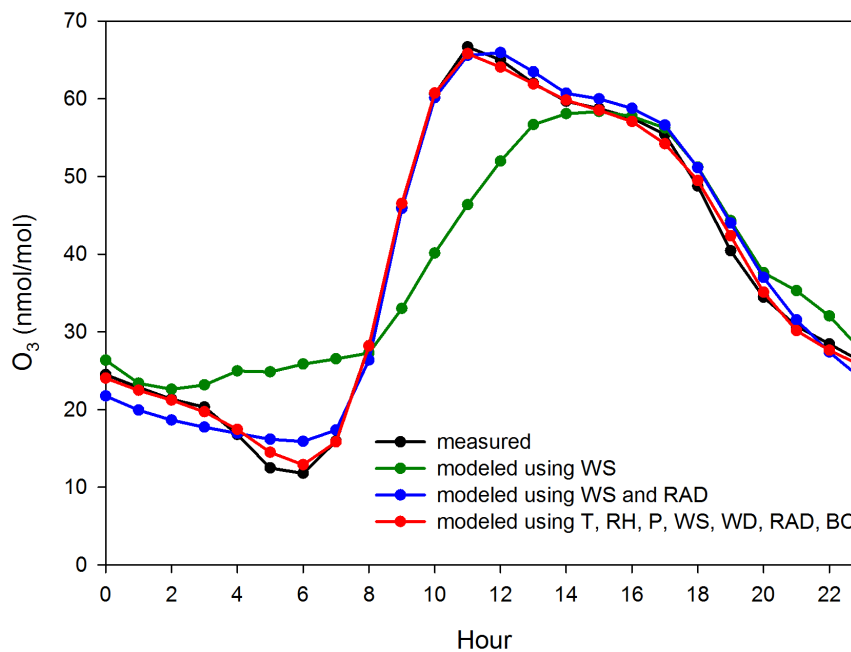


Figure 2.6: Average seasonal diurnal variation of O_3 concentrations for the pre-monsoon period, compared with modeled O_3 using different input parameters (T, RH, P, WS, WD, RAD, and BC).

O_3 mixing ratios for all hours of the day quite well, whereas a simulation that included only wind speed (a good proxy of atmospheric dynamics) reproduced the afternoon (after 15:00) and evening levels of O_3 with accuracy, missing the main O_3 peak before noon completely. In contrast, by using both wind speed and solar radiation as input parameters, the model reproduced the peak before noon and the high levels of afternoon–evening O_3 well. Putting together the results of these two simulations, it is evident that the high level of O_3 during the afternoon is mainly due to dynamics (vertical intrusion from upper atmospheric layers and/or horizontal advection), for the following two reasons. (i) In the model, the wind speed used as input is enough to reproduce the afternoon concentrations of O_3 and (ii) the inclusion of solar radiation does not improve the agreement between measured and modeled O_3 during the afternoon, but substantially enhances the agreement between measurements and simulations before noon, when photochemistry, as expected, plays a larger role. The photochemistry contribution, obtained by comparing these simulations (Fig. 2.6), varied as a function of the hour of the day, ranging from 6 to 34 %.

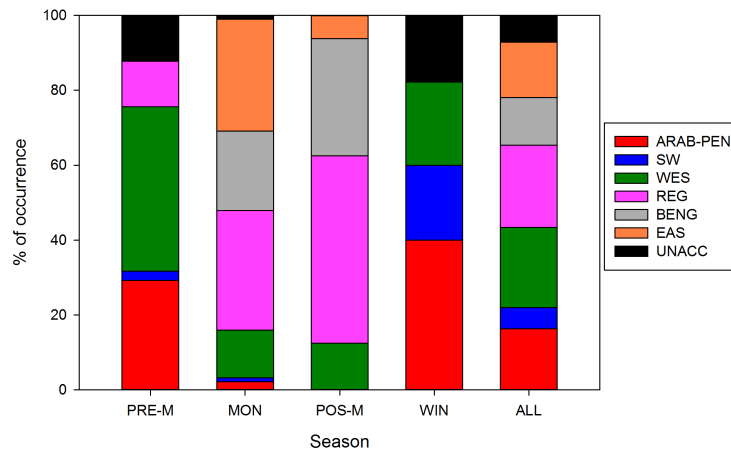


Figure 2.7: Percentage of occurrence registered by the six different back-trajectory clusters considered in this work, divided by season (PRE-M: pre-monsoon, MON: monsoon, POS-M: post-monsoon, WIN: winter, and ALL: considering the whole measurement period). Abbreviations for clusters are as follows: ARAB-PEN – Arabian Peninsula, SW – southwesterly, WES – western, REG – regional, BENG – Bay of Bengal, EAS – eastern, and UNACC – unaccounted for.

2.3.5 Influence of atmospheric synoptic circulation

Synoptic-scale air-mass circulation scenarios

With the purpose of investigating the variability of large-scale atmospheric circulation affecting the region of interest, the HYSPLIT 5-day back-trajectories were clustered. Here, it should be clearly stated that this analysis has been carried out with the aim of providing information about the synoptic-scale circulation scenarios which affect the region where the Kathmandu Valley is located, therefore investigating the link among these scenarios with the SLCF/P variability. In order to retain robust information, only the days for which the same cluster was observed for at least three-quarters of daily observations were considered in this analysis. Overall, nine clusters were identified; Fig. 2.7 shows the percentage of occurrence for each cluster for the whole investigation period, as a function of the different seasons. Three clusters out of nine had a very small percentage of occurrences (i.e., less than 5% of air-masses was recorded for each of these clusters), thus were not retained for further analysis. “Regional” (REG, 21.9%) and “western” (WES, 21.4%) clusters showed the highest occurrence values. The first encompasses trajectories within a $10^\circ \times 10^\circ$ area centered on the region of interest, thus indicating the occurrence of regional-scale atmospheric circulation: trajectories from this area were present in every season, except winter.

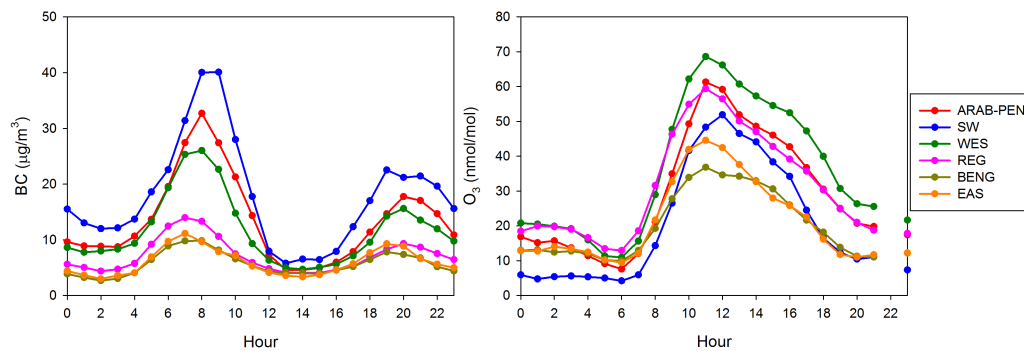


Figure 2.8: BC (left) and O₃ (right) diurnal variations as a function of the different air-mass clusters shown in Fig. 2.7. Abbreviations are as follows: ARAB-PEN – Arabian Peninsula, SW – southwesterly, WES – western, REG – regional, BENG – Bay of Bengal, and EAS – eastern.

WES, on the other hand, represents westerly air-masses which originated (5 days backward in time) at a longitude around 60° E. The cyclonic behavior of these back-trajectories indicated that synoptic-scale westerly disturbances could steer air-masses under these scenarios. A significant fraction of trajectories (16.3%), mostly observed during pre-monsoon and winter, showed westerly transport at the synoptic scale again (even if presenting higher horizontal velocities with respect to WES): 5-day back-trajectories originated or traveled over desert areas of the Arabian Peninsula (ARAB-PEN). The larger latitudinal span of these back-trajectories suggested that synoptic-scale disturbances and subtropical jet stream latitudinal excursions could steer the air-masses towards the region of interest. During the monsoon and post-monsoon seasons, the atmospheric circulation was strongly affected by the summer monsoon and by the occurrence of low pressure areas in the Bay of Bengal, which enhanced the possibility to observe easterly circulation: i.e., “Bay of Bengal” (BENG, 12.8%) and “Eastern” (EAS, 14.8%) clusters. Finally, a non-negligible fraction of days (5.6%, occurring mostly during winter) can be characterized by a southwesterly circulation (SW), which can be related to the passage of synoptic-scale disturbances over the western Indian subcontinent (Böhner, 2006).

Influence of atmospheric circulation on O₃ and BC diurnal variations

The BC and O₃ diurnal variations, as a function of the different synoptic-scale air-mass circulation scenarios are shown in Fig. 2.8. The BC diurnal variation was only partly dependent on the air-mass clusters: the shape was the same for all of the clusters, although a difference in the amplitude of the cycles was recorded. In

particular, regional air-masses or on the eastern regions (BENG and EAS) were associated to smaller BC values both during peaks and minimum levels. This is because air-masses from these regions were retrieved only during monsoon and post-monsoon seasons, when BC concentrations were at their minimum (no occurrences at all were registered during winter) due to enhanced wash-out. On the other hand, during winter and pre-monsoon, the highest values of BC were recorded under ARAB-PEN, WES, and SW air-mass circulation. Particularly, the diurnal cycle of BC and the relative 24 h averaged peak values in the morning and in the evening were maximized when SW circulation affected the measurement site.

Concerning O₃ diurnal variation, significant differences can be observed as a function of different synoptic-scale circulation scenarios. Despite a moderate diurnal cycle of BC, the highest diurnal peak value and the largest amplitude of daily cycle were observed for the WES circulation; air-masses from the free troposphere or those that overpass polluted regions above the Indo-Gangetic Plain could supposedly contribute to the appearance of these high values. It is interesting to note that for the three synoptic-scale scenarios, most frequent during pre-monsoon and winter (i.e., WES, ARAB-PEN, and SW), very different results were obtained for BC and O₃. In particular, the diurnal peaks were maximized (minimized) for O₃ (BC). This can be tentatively explained by suggesting that under this circulation, meteorological conditions should favor the dilution of polluted air-masses emitted from surface sources and transport of O₃-rich upper layers by vertical entrainment processes (e.g., Kleinman et al., 1994). Similar diurnal cycles but lower mixing ratios were tagged to ARAB-PEN and REG circulations. As for BC, the smallest O₃ diurnal cycles were linked to the typical monsoon circulations EAS and BENG: this is in agreement with Agrawal et al. (2008) who indicated that due to widespread rain precipitation and cloudy conditions, summer monsoon is not favorable to photochemical O₃ production and to the occurrence of elevated O₃ regime. With respect to other atmospheric circulation, the average O₃ diurnal cycles for ARAB-PEN, REG, and WES were characterized by high values from 13:00 to 21:00, while an intermediate condition was observed for the SW circulation.

Influence of open vegetation fires on BC and O₃ values

As shown in Putero et al. (2014), the BC and O₃ values in Nepal are partly influenced by the emissions from open vegetation fires, occurring across broad regions. In order to evaluate the contribution of large open fires emissions to the BC and O₃ variations observed at Paknajol, the daily total number of fires by the MODIS product has been retrieved and used. This is an important point to assess the impact of external pollution sources to air quality in the urban megacity.

Fire pixels (with a confidence value $\geq 75\%$) were derived from the MODIS Global Monthly Fire Location Product (MCD14ML); these have been “filtered” by means of the MODIS Land Cover Climate Modeling Grid product (MCD12C1), in order to retain only fires occurring over specific land use categories (i.e., vegetation, croplands, forests; for more details on such products, see Justice et al., 2002; Friedl et al., 2010). This methodology did not allow us to account for the fraction that came from “residential” burning (e.g., garbage burning occurring in urban areas, or domestic burning). The study area for the open vegetation fires occurrences was the southern Himalayas box, 26–30° N, 80–88° E, considered in Putero et al. (2014) as the main contributor for Nepal. Over the whole period, the correlation coefficient between the number of fires and the delayed (from t to $t - 3$ days) BC concentrations showed almost null correlation (0.10), pointing out that, in general, the BC fraction could be mainly influenced by other (local) anthropogenic emissions, also including the contribution from domestic and garbage burning. A sensitivity study was carried out by considering slightly different spatial domains for fire detection, without significant changes of the results. Nevertheless, some BC peaks have been superimposed to periods of high fire activities. During these events, the large-scale synoptic scenario, as deduced by HYSPLIT, showed WES and REG circulation, thus supporting the presence of regional-scale transport, and the possible influence from specific distinct (major) events of open vegetation fires. However, several limitations of the use of back-trajectories and MODIS data (which can miss short-time events, small fires, and fires under clouds) have to be taken into account; for this reason, the use of chemical transport modeling outputs would be required for investigating these events in deeper detail. Figure 2.9 shows the diurnal BC and O₃ variations for the period of study (Fig. 2.9a–b) and the time series of total daily fires over the southern Himalayas box (as defined above) retrieved by MODIS (Fig. 2.9c).

BC diurnal variation seemed to remain quite constant over the entire time period, thus suggesting no prominent influence by fire emissions. During high fire activity periods (e.g., during the pre-monsoon season), BC showed increased concentrations, even though no shift of the daily maxima position occurred, thus indicating that local emissions (traffic and/or domestic, including open garbage burning) and PBL dynamic are the main factors influencing BC concentrations at Paknajol, further supported by the high ratio BC / PM₁. The same could not be said considering O₃ measurements. When the number of fires was at its highest, the O₃ peak was “shifted” in time and appeared in the late afternoon (between 16:00 and 18:00). This period almost perfectly matched with the “bump” in O₃ observed at the diurnal scale during the pre-monsoon season (Sect. 2.3.4). Biomass burning plumes that were enriched in O₃, photochemically produced after enhanced emission of precursors (e.g., CO, VOCs), could supposedly be

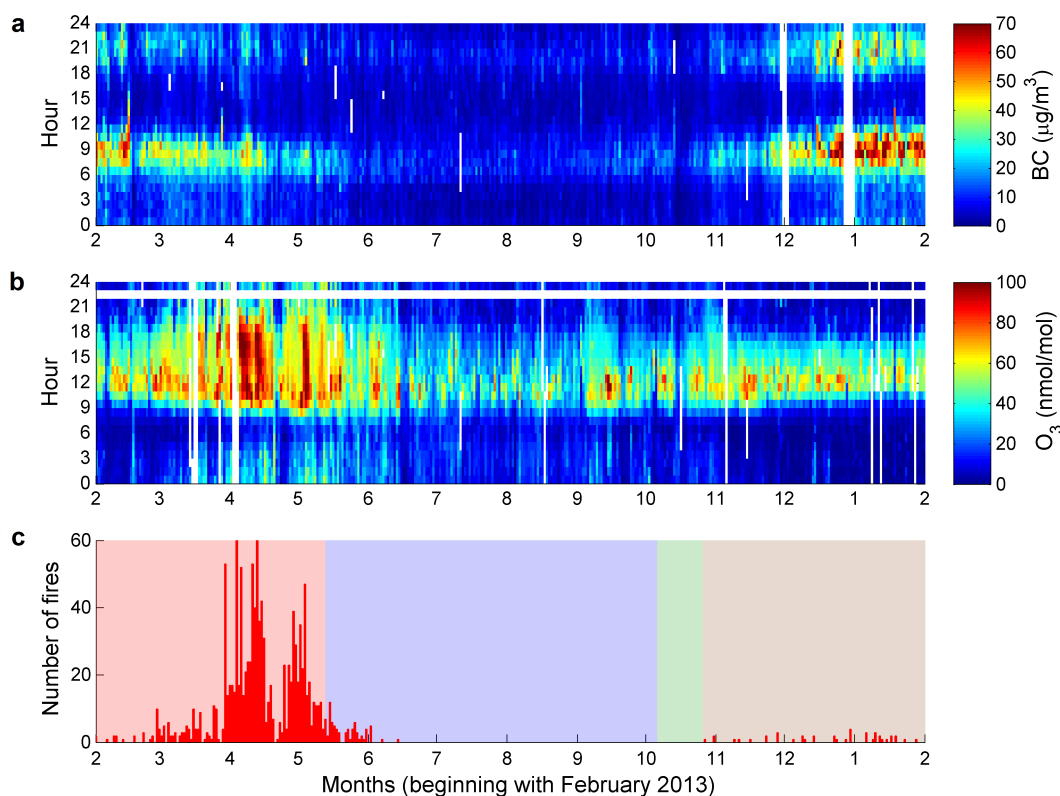


Figure 2.9: BC (a) and O_3 (b) diurnal variations over the entire sampling period. The color scale has been set to a maximum of $70 \mu\text{g m}^{-3}$ and $100 \text{ nmol mol}^{-1}$ for BC and O_3 , respectively. Panel (c) shows the total daily number of fires found in the southern Himalayas box (see Putero et al., 2014); note that the y axis has been limited to a maximum value of 60. Shaded areas in panel (c) indicate the different seasons (red: pre-monsoon, blue: monsoon, green: post-monsoon and brown: winter).

transported over Kathmandu and possibly mixed within PBL due to efficient vertical mixing between upper ozone layers and surface layer.

2.4 Conclusions

In this chapter, one full year of hourly-resolution data (February 2013–January 2014) of SLCF/P (BC and O_3), as well as aerosol number and mass concentration, was analyzed. Measurements were collected at Paknajol, an urban site in the city center of Kathmandu, Nepal. Very high values of SLCF/P were detected during the whole measurement period, indicating persistent poor air quality conditions, dangerous for human health and the environment, including an influence on

local/regional climate.

Equivalent BC, aerosol number concentration and aerosol mass concentration exhibited seasonal cycles, with the highest values during winter and pre-monsoon, and minima during the summer. Surface O₃ was characterized by maximum values during the pre-monsoon and a diurnal cycle (daytime maxima) opposite to what was observed for aerosol (midday minimum and maximum early in the morning and late evening). The diurnal behavior of BC and aerosol number concentration indicated that local pollution sources, mostly related to road traffic or domestic emissions, represent the major contribution to air pollution in Kathmandu.

Concerning O₃, the analysis of the seasonal change of the diurnal cycle and correlation with meteorological parameters and aerosol properties suggested that apart from photochemistry (whose contribution ranges from 6 to 34 %), PBL dynamics and wind circulation have a significant role in determining O₃ variability: during midday, air-masses richer in O₃ appeared to be transported to the measurement site by flows through the mountain passes located at the western rim of the Kathmandu Valley. Especially during pre-monsoon, high O₃ values were observed during the afternoon. Mixing and vertical entrainment processes between upper layers and PBL could partially explain the occurrence of these high values and can lead to favorable conditions for O₃ production that will often result in exceedance of guideline values set by the World Health Organization (WHO).

The possible impact of emissions by major open vegetation fires occurring at the regional scale has been assessed by analyzing MODIS fire distribution. A significant impact has been observed only for O₃ and during specific episodes, which is able to affect day-to-day variability. Despite the limitations of the methodology (e.g., garbage and domestic burning were not considered in this analysis and small or short-lasting open fires can be missed by satellite detection), this indicates that the occurrence of widespread biomass burning emissions can represent, in particular during the pre-monsoon season, a non-negligible source of precursors for photochemically-produced O₃ in the Kathmandu Valley.

The analysis of large-scale atmospheric circulation demonstrated a significant impact of the background synoptic-scale circulation on diurnal cycles of BC and O₃ in Kathmandu. In particular, atmospheric circulation related to westerly (WES, ARAB-PEN, SW) and regional (REG) circulations appeared to be especially conducive for the occurrence of the high BC and O₃ values.

Considering the 24 h limit of 120 $\mu\text{g m}^{-3}$ proposed for PM₁₀ measurements by the Government of Nepal (Giri et al., 2006), a total of 124 exceedances were found for the 2013 period, 51.4 % of the available PM₁₀ data. In 2003, the Nepali Ministry of Population and Environment (MoPE) has also defined five different quality

descriptions (classes) based on PM_{10} levels (see HMG/MOPE, 2003). During our observation period, following these references, 12 days (5 % of data) were categorized as “good” (range $0\text{--}60\ \mu\text{g m}^{-3}$), 105 as “moderate” ($61\text{--}120\ \mu\text{g m}^{-3}$), and 103 days were tagged as “unhealthy” ($121\text{--}350\ \mu\text{g m}^{-3}$), representing 43.6 and 42.7 % of data, respectively. A total of 21 days (8.7 %) were classified as “very unhealthy” ($351\text{--}425\ \mu\text{g m}^{-3}$, 13 days) or “hazardous” ($> 425\ \mu\text{g m}^{-3}$, 8 days). Therefore, these data reveal the poor air quality in Kathmandu, also considering that the WHO guideline defines the limits of $20\ \mu\text{g m}^{-3}$ per year and $50\ \mu\text{g m}^{-3}$ per 24 h. WHO (2006) also defined air quality guidelines for O_3 based on the analysis of the daily maximum 8 h concentrations: high levels (HL: $240\ \mu\text{g m}^{-3}$), interim target-1 (IT-1: $160\ \mu\text{g m}^{-3}$), and air quality guidelines (AQG: $100\ \mu\text{g m}^{-3}$). Based on Paknajol data, 13 days that exceed the IT-1 (3.5 % of the data set) and 125 days (34 % of the data set) that exceed the AQG were found. It should be noted that WHO associated “important health effects” with IT-1 exceedances, indicating that exposures to the IT-1 level increase the number of attributable deaths by 3–5 %. Conversely, the exceedances of the AQG are related to an estimated 1–2 % increase in daily mortality (WHO, 2006). The totality of IT-1 exceedances were recorded during the pre-monsoon season; while AQG exceedances were observed for 62 % during the pre-monsoon, 22 % during the monsoon, and the remaining exceedances during post-monsoon (4 %) and winter (12 %). Roughly, the total number (97 %) of exceedances (IT-1 and AQG) were observed from 10:00 to 18:00. It is worth noting that 37 days (all detected during the pre-monsoon) were affected by the occurrence of major open vegetation fire activity during the investigated period. By neglecting these days, all of the IT-1 exceedances for O_3 at Paknajol were removed, and 88 AQG exceedances were retained (all the days with fire activity were tagged to AQG exceedances), representing a 29 % (47 %) decrease on a yearly (seasonal) basis.

The information of this study, developed in the framework of the SusKat-ABC project, may be useful for implementing control measures to mitigate the occurrence of acute pollution levels in the Kathmandu municipality, as well as for improving regional climate conditions. This is important for the wider area that lies at the Himalayan foothills.

Comparison of SLCF/P variability at the Kathmandu “hot spot” and at the southern Himalayas

In this chapter, the role played by air-mass transport from the planetary boundary layer (PBL) over the Himalayan foothills in affecting BC and O₃ variability in the southern Himalayas is investigated. The analysis is performed by comparing the first full year (February 2013–January 2014) of simultaneous BC and O₃ measurements at two sites in Nepal, characterized by very different conditions, i.e.: Paknajol (1380 m a.s.l.) in the Kathmandu Valley (one of the regional urban “hot spots”), and the WMO/GAW global station Nepal Climate Observatory-Pyramid (NCO-P, 5079 m a.s.l.) near the base camp of Mt. Everest, representative of the background conditions of the high Himalayas and the free troposphere. The correlation study between the PBL height (derived from the ERA-Interim reanalysis) over the Kathmandu urban area and the BC and O₃ concentrations at NCO-P indicated that these parameters are linearly correlated ($r^2 = 0.27$ for BC, and $r^2 = 0.25$ for O₃). BC and O₃ concentrations at NCO-P also showed linear correlation with the variability of two tracers (i.e., CO and tropospheric NO₂, retrieved by satellite datasets) in the pixel area that comprises Kathmandu. Moreover, when introducing an additional constraint in the analysis (i.e., back-trajectories), 50 % and 65 % of BC and O₃ variability can be explained by the PBL variations over the Kathmandu urban area, in days in which air-mass

A modified version of this chapter is in preparation as: Putero, D., Marinoni, A., Bonasoni, P., Calzolari, F., and Cristofanelli, P.: Comparison of black carbon and ozone variability at the Kathmandu “hot spot” and at the southern Himalayas, *Aerosol Air Qual. Res.*, in preparation.

transport between the two measurement sites is observed, thus supporting the role of vertical transport of polluted air-masses to SLCF/P variability over the Himalayas.

3.1 Introduction

Several works have recently shown that the transport of BC, O₃, and other pollutants from the highly polluted areas in south Asia (e.g., the Indo-Gangetic Plain and the Himalayan foothills) to the Himalayas may occur, due to the regional and local meteorology, and the specific mountain/valley breeze systems that characterize these areas (e.g., Bonasoni et al., 2010; Hyvärinen et al., 2011; Lu et al., 2011; Cristofanelli et al., 2014; Putero et al., 2014; Raatikainen et al., 2014; Dumka et al., 2015; Lüthi et al., 2015). All of these studies pointed out that the large amounts of SLCF/P reaching the southern Himalayas originate within the planetary boundary layer (PBL) of central Pakistan, northwestern Indo-Gangetic Plain, and Himalayan foothills. In these areas, besides anthropogenic emissions (transportation, domestic uses, industrial emissions and garbage burning), open fire emissions (both related to crop management and forest fires) can represent a significant source of SLCF/P transported to the Himalayas, especially during the pre-monsoon season.

However, due to the limited (both in time and space) observations still available, the studies aimed at assessing the role of transport of polluted air-masses from the foothills up to the Himalayas are still incomplete, especially for what concerns the evaluation of the interannual variability of these SLCF/P at different measurement sites, and the specific role played by anthropogenic and natural emissions occurring within the PBL in determining their variability in the southern Himalayan region.

This chapter provides the first attempt of linking the BC and O₃ variability in the Himalayas with the emissions occurring within the PBL over the Himalayan foothills. This is performed by comparing the first full year (February 2013–January 2014) of BC and O₃ concentrations at two measurement sites in Nepal, i.e., Paknajol in the Kathmandu Valley and the Nepal Climate Observatory-Pyramid (NCO-P) in the southern Himalayas. While the Kathmandu Valley in Nepal represents one of the regional urban “hot spots” in terms of air pollution, as well as a source for the high levels of these SLCF/P, due to the increasing population and consequent rapid but unplanned urbanization (see Chapter 2), NCO-P is a remote site representative of the conditions that characterize the southern Himalayas. The distance between the two sites is just 150 km as the crow flies, with an altitudinal distance of ~3700 m (Fig. 3.1). This represents a good opportunity to investigate the possible role of emissions occurring in

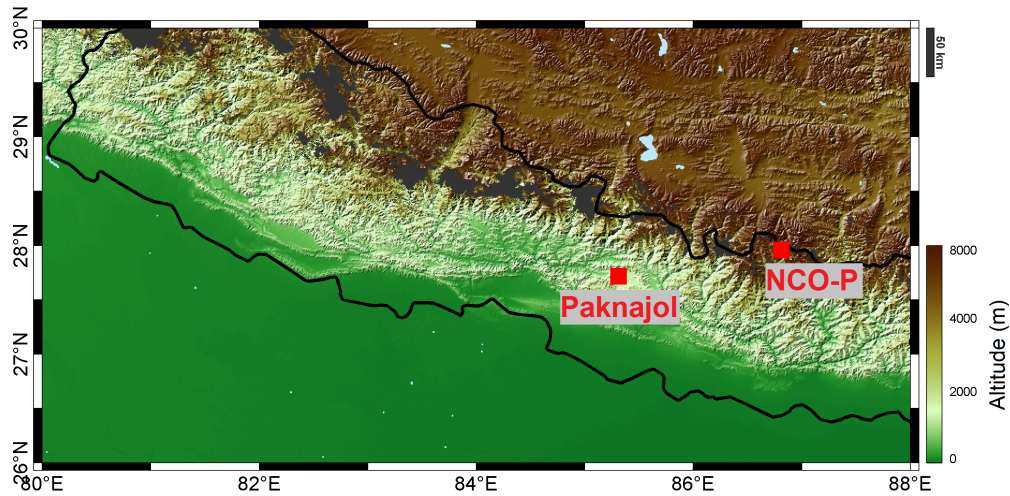


Figure 3.1: Geographic map of Nepal with the Paknajol and NCO-P locations.

the Kathmandu megacity in influencing the SLCF/P variability in the southern Himalayas.

3.2 Materials and methods

3.2.1 Measurement sites and instrumental setup

The Nepal Climate Observatory-Pyramid (NCO-P; 27.95° N, 86.82° E, 5079 m a.s.l.) is located at a remote site in the southern Himalayas, in the Sagarmatha National Park in Nepal (along the Khumbu Valley), near the base camp of Mt. Everest. The Observatory, installed in 2006, stands at the top of a hill, 200 m from the Pyramid International Laboratory (a multi-disciplinary high altitude research center, jointly founded by the Ev-K2-CNR Committee and the Nepal Academy of Science and Technology in 1990). NCO-P was one of the 31 global stations belonging to the Global Atmosphere Watch program of the World Meteorological Organization (WMO/GAW, see WMO, 2017). Because of its location, the site is not influenced by direct anthropogenic sources (only small villages are present along the valley), but the valley wind thermal regime systematically favors the transport of polluted air-masses from the lower troposphere/Himalayan foothills up to the measurement site (Bonasoni et al., 2010). Thus, this measurement site is an ideal location for investigating the impact of regional pollution up to the Himalayan environment. Unfortunately, the station stopped its activities on October 2015.

The Paknajol sampling site (27.72° N, 85.30° E, 1380 m a.s.l.) was already

introduced in Chapter 2, Sect. 2.2.1. As largely pointed out and described in Chapter 2, Paknajol observations are well representative of the anthropogenic emissions occurring in the Kathmandu Valley, hereby used as a benchmark for the polluted conditions of the Himalayan foothills region.

Measurements of surface O_3 (by using an UV-absorption analyzer, TEI 49i, Thermo Environmental), equivalent BC (simply referred to as BC, through a Multi Angle Absorption Photometer, MAAP 5012, Thermo Electron Corporation) and meteorological parameters (Weather Transmitter WXT 510, Vaisala) are available at both measurement sites (from 2006 at NCO-P, and from 2013 at Paknajol). Further details on the measurement sites and the instrumental setup are given in previous publications (Bonasoni et al., 2010; Cristofanelli et al., 2010; Marinoni et al., 2010; Putero et al., 2015).

Thus, simultaneous BC, O_3 and meteorological observations were continuously carried out over February 2013–January 2014. Unlike Chapter 2, data presented in this chapter refer to UTC: this was done to have coherence with the satellite and modeled PBL datasets. However, all of the other conditions presented in Chapter 2 remain true for both of the measurement sites, i.e.: (i) data are validated on a 1-min basis, then averaged to a common time base of 1 hour and 1 day; (ii) data are expressed as STP (0°C and 1013 hPa) conditions; and (iii) at least 50 % coverage was required to have each 1-h average.

3.2.2 Satellite datasets

CO values used in this analysis are the observations from the Atmospheric Infrared Sounder (AIRS) onboard the NASA Aqua satellite. The Level-3 daily $1^\circ \times 1^\circ$ gridded standard products (AIRX3STD, see McMillan et al., 2011), for the grid point closest to Paknajol coordinates, and at the vertical slice of 850 hPa, were chosen. To obtain a better spatial coverage, as well as to minimize the day/night difference, the daytime/ascending and the nighttime/descending retrievals are averaged to obtain the daily CO value.

Tropospheric NO_2 observations derive from the OMI/Aura retrievals (Levelt et al., 2006). In particular, the Level-3 daily $0.25^\circ \times 0.25^\circ$ global gridded total and tropospheric NO_2 product (OMNO2d, see Bucsela et al., 2006) was used. As for CO, the value closest to Paknajol coordinates was chosen; each NO_2 value reported refers to the number of molecules in an atmospheric column which extends from the surface to the top of the troposphere. Furthermore, only data for which cloud radiance fraction is less than 30 % were used.

3.2.3 Back-trajectories and PBL height

To evaluate the synoptic-scale variability of the air-masses reaching NCO-P, a set of 5-days back-trajectories starting at the measurement site was computed every 6 h (at 0:00, 6:00, 12:00 and 18:00 UTC), by using the Lagrangian analysis tool LAGRANTO (Wernli and Davies, 1997; Sprenger and Wernli, 2015). The model calculations are based on the 6-hourly operational analysis field of the ECMWF. Each set comprised of 12 back-trajectories, with endpoints shifted by $\pm 1^\circ$ in latitude/longitude and in a vertical range of ± 50 hPa with respect to NCO-P location, to partially compensate for uncertainties related to the absence of sub-grid scale processes (e.g., convection and turbulent diffusion) in LAGRANTO. The temporal resolution for the back-trajectories is one point every 2 h.

The PBL height over Kathmandu is retrieved from the ERA-Interim reanalysis dataset (Dee et al., 2011). The spatial resolution of the dataset is approximately 80 km (T255 spectral); since there is no exact value corresponding to Kathmandu coordinates, it was obtained by linearly interpolating the two grid points closest to Paknajol. The temporal resolution for the PBL dataset is one value every 3 h: these were then averaged to obtain an average daily value.

As also remarked in Raatikainen et al. (2014), it is well known that both back-trajectory calculations and modeled PBL heights suffer from uncertainties in mountainous environments. However, due to the lack of continuous direct observations (e.g., radiosondes) regarding the period under study in Kathmandu, the use of daily PBL averages is justified for linking the day-to-day observations between the two measurement sites.

3.3 Results

3.3.1 Meteorological characterization and transport patterns

Both measurement sites are affected by a synoptic-scale circulation modulated by the occurrence of the south Asian monsoon. This large-scale meteorological characterization was extensively treated (for NCO-P) in several works (see, e.g., Bonasoni et al., 2010; Cristofanelli et al., 2010; Putero et al., 2014; Balestrini et al., 2016). The large-scale circulation patterns over the period under study for the different seasons are presented in Fig. 3.2. During non-monsoon seasons (panels a, c, and d), due to the influence of the subtropical jet stream, a westerly circulation prevails, with limited vertical displacement of air-masses. As also presented in Schiemann et al. (2009), the large-scale circulation is steered by the subtropical jet stream and embedded synoptic disturbances travelling eastward towards the Himalayas. Conversely, the summer monsoon season is affected

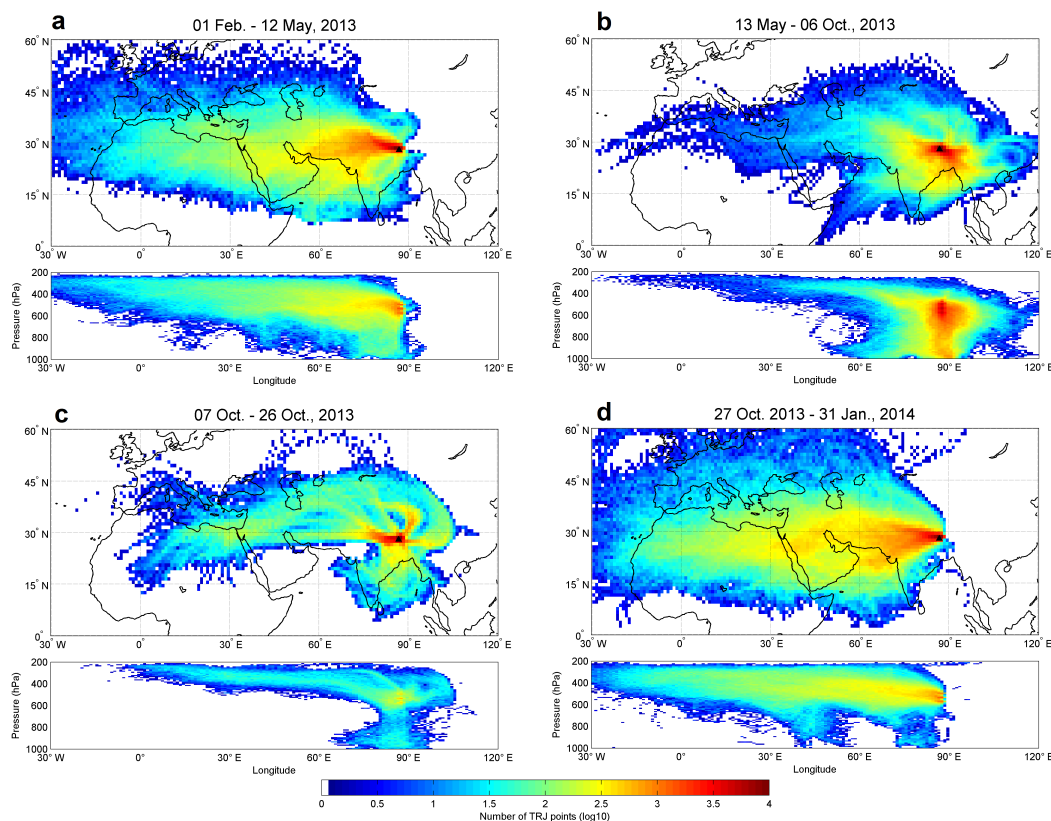


Figure 3.2: Concentration field for back-trajectories starting at NCO-P, for pre-monsoon (a), monsoon (b), post-monsoon (c), and winter (d). The season definition is the same given in Chap. 2. For each subplot, the upper panel represents the spatial aggregation of back-trajectory points over a $1^\circ \times 1^\circ$ grid, while the bottom panel indicates the vertical displacement (steps of 10 hPa) as a function of longitude.

by a prevalent southern circulation characterized by enhanced vertical uplift of air-masses from the Indian sub-continent and the Indian Ocean. Because the aim of this chapter is to investigate the impact of polluted air-mass transport from the Himalayan foothills region that encloses the Kathmandu Valley to NCO-P and the Himalayas, the seasonal onset and decay dates were defined according to the variability of the weather regime at NCO-P, as already done in Chapter 2 (Table 2.1).

Besides the synoptic-scale weather, both measurement sites are also affected by local circulation patterns, which can modulate BC and O_3 diurnal variability. In particular, as already presented in Chapter 2 (and references therein), Kathmandu (and, therefore, Paknajol) local meteorology is characterized by two very different circulation features: afternoon westerly/northwesterly winds that

intrude the valley through the western passes, and low speed katabatic winds that descend from the mountain slopes during the night. On the other hand, NCO-P is affected by the systematic occurrence of mountain/valley winds in two specific directions determined by the valley's topography (S-SW and N-NE). In particular, day-time up-valley winds are observed from October to May, while mountain winds prevail during night-time. In the summer months, the valley winds are predominant also during the night due to the influence of the monsoon (Bonasoni et al., 2010).

3.3.2 BC and O₃ variations at both stations

Figure 3.3 shows the temporal variation of the daily averages for the parameters considered in this study, as presented in Sect. 3.2. BC (panel a) is characterized by values differing nearly one order of magnitude between the two measurement sites (Fig. 3.3a), further indicating their very different nature: Paknajol presented an average value of $11.7 \pm 6.7 \mu\text{g m}^{-3}$ (average value ± 1 standard deviation, computed by considering daily averages), while at NCO-P the average BC was $0.3 \pm 0.4 \mu\text{g m}^{-3}$. Also the seasonality is changing: Paknajol recorded the highest BC values in winter ($18.3 \pm 6.8 \mu\text{g m}^{-3}$), while at NCO-P the highest concentrations were found in the pre-monsoon ($0.6 \pm 0.6 \mu\text{g m}^{-3}$). This indicates the specific role of meteorology and valley breeze transport in this latter season at NCO-P, while the highest wintertime values at Paknajol are representative of increased domestic heating emissions, and the occurrence of stable and dry meteorological conditions favoring the accumulation and trapping of pollutants emitted in the Kathmandu basin (Putero et al., 2015). Very low concentrations were found during the monsoon for both sites ($6.3 \pm 1.7 \mu\text{g m}^{-3}$ and $0.1 \pm 0.1 \mu\text{g m}^{-3}$, for Paknajol and NCO-P, respectively).

Also O₃ variations (Fig. 3.3b) were slightly different for the two measurement sites: both presented maximum values in the pre-monsoon ($38.1 \pm 13.1 \text{ nmol mol}^{-1}$ and $58.3 \pm 10.9 \text{ nmol mol}^{-1}$, for Paknajol and NCO-P, respectively), while minima were recorded in winter at Paknajol ($19.6 \pm 4.8 \text{ nmol mol}^{-1}$) and during the monsoon at NCO-P ($41.1 \pm 11.8 \text{ nmol mol}^{-1}$). However, NCO-P values resulted always higher than Paknajol ones (on average: $48.2 \pm 12.5 \text{ nmol mol}^{-1}$ and $26.9 \pm 11.6 \text{ nmol mol}^{-1}$); this is due to an atmospheric "background", which is higher in the free troposphere of the southern Himalayas with respect to the Kathmandu Valley, where removal processes related to dry deposition and night-time NO titration are enhanced.

In addition to the SLCF/P variability, additional satellite datasets were analyzed, i.e.: CO values from AIRS and tropospheric NO₂ from OMI (as introduced in Sect. 3.2.2). CO values (Fig. 3.3c) presented a clear seasonal cycle, being the highest in the pre-monsoon ($145.5 \pm 13.6 \text{ nmol mol}^{-1}$) and the lowest during

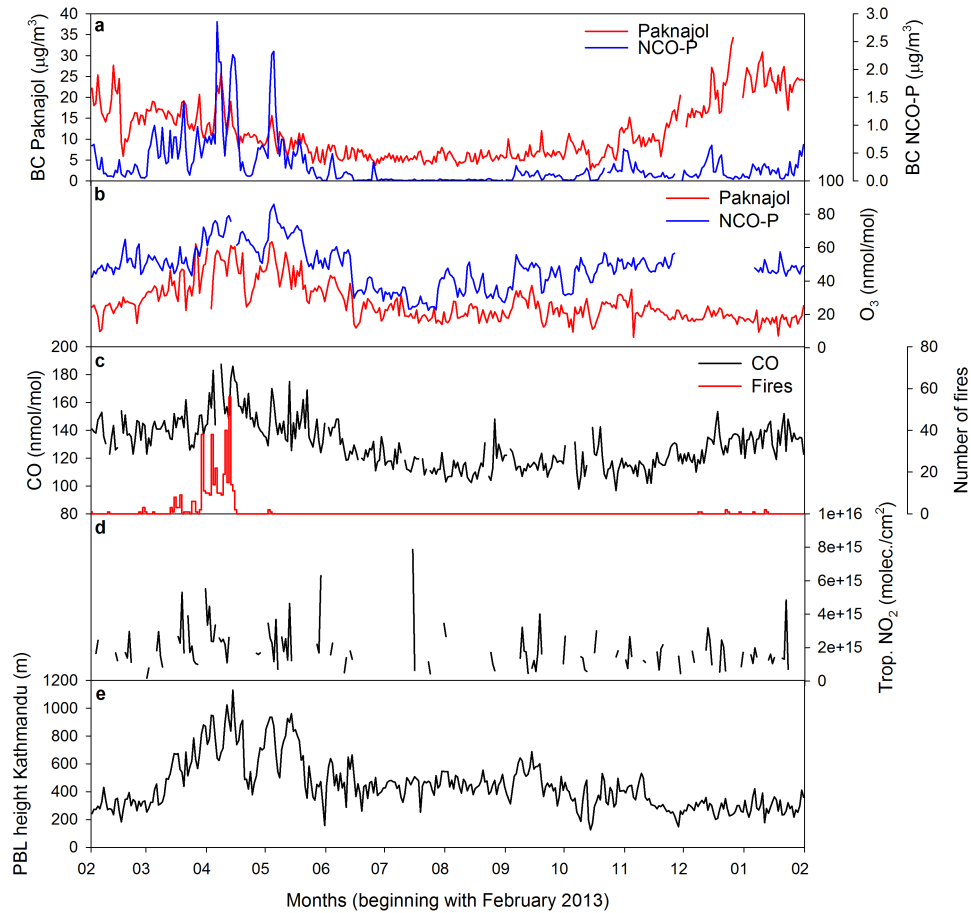


Figure 3.3: Time series of daily values for black carbon (BC, panel a) and surface ozone (O_3 , panel b) at both Paknajol (red line) and NCO-P (blue line) stations, CO (c), tropospheric NO_2 column (d), and planetary boundary layer (PBL) height over an area which comprises Kathmandu (e). Together with CO (c) is shown the number of fires observed by MODIS in a $2^\circ \times 2^\circ$ area enclosing the Kathmandu Valley (i.e., $27\text{--}29^\circ \text{N}$, $84\text{--}86^\circ \text{E}$).

the monsoon and post-monsoon seasons ($122.0 \pm 13.3 \text{ nmol mol}^{-1}$ and $117.0 \pm 12.2 \text{ nmol mol}^{-1}$, respectively). These CO values are lower than previous investigations in the Kathmandu Valley (e.g., Panday and Prinn, 2009; Rupakheti et al., 2016); this can be partially explained because the values hereby presented refer to an area wider than the Kathmandu urban area itself, thus including rural zones characterized by lower CO emissions. Nonetheless, being the Kathmandu Valley the major source of emissions of the pixel under study, and due to the lack of continuous in situ CO observations for the period of interest, the CO values by AIRS are hereby considered representative of the Kathmandu extended urban area. Despite most of CO in this area is produced by anthropogenic emissions (e.g., traffic, domestic heating, combustion of fossil fuels in industries), a non-negligible part derives from waste and biomass burning (Stockwell et al., 2016; Rupakheti et al., 2016). To better highlight the mutual variations along with CO, Fig. 3.3c shows the number of fires observed by MODIS (MCD14ML product, see Justice et al., 2002) in a $2^\circ \times 2^\circ$ area around Paknajol location (i.e., $27\text{--}29^\circ \text{ N}$, $84\text{--}86^\circ \text{ E}$). From a qualitative point of view, it is interesting to note the co-variability between CO and the number of fires: the period characterized by increased fire emissions (i.e., pre-monsoon) corresponded to peaks in CO.

The tropospheric NO_2 column (hereinafter referred to as NO_2 , for simplicity) variations, over an area built considering the Kathmandu Valley as center, are shown in Fig. 3.3d. NO_2 is hereby considered since it is a photochemical precursor of O_3 , being formed by combustion processes related to vehicular traffic or biomass burning. Although several gaps in the time series were present throughout the period under study, the NO_2 variations at Kathmandu followed a seasonality similar to that of CO: the highest values were found in the pre-monsoon ($2.0 \pm 1.1 \times 10^{15} \text{ molec. cm}^{-2}$), favored by low humidity values and mild temperatures that cause reduction in photolysis removal processes of NO_2 , and the lowest in the post-monsoon ($1.5 \pm 6.9 \times 10^{15} \text{ molec. cm}^{-2}$). These results appear higher than the tropospheric NO_2 values reported in a trend study computed over the last decade (i.e., $1.03 \pm 0.05 \times 10^{15} \text{ molec. cm}^{-2}$, see ul-Haq et al., 2015), and consistent with the increasing trends that were found to characterize the tropospheric NO_2 concentrations in both Nepal and south Asia (Ghude et al., 2009; ul-Haq et al., 2015).

3.3.3 Effects of PBL variability on BC and O_3 concentrations at NCO-P

To investigate the possible role of the PBL variability over the Himalayan foothills in favoring the transport of polluted air-masses rich in BC and O_3 towards NCO-P and the Himalayas, the BC and O_3 variability at NCO-P, as a function of the

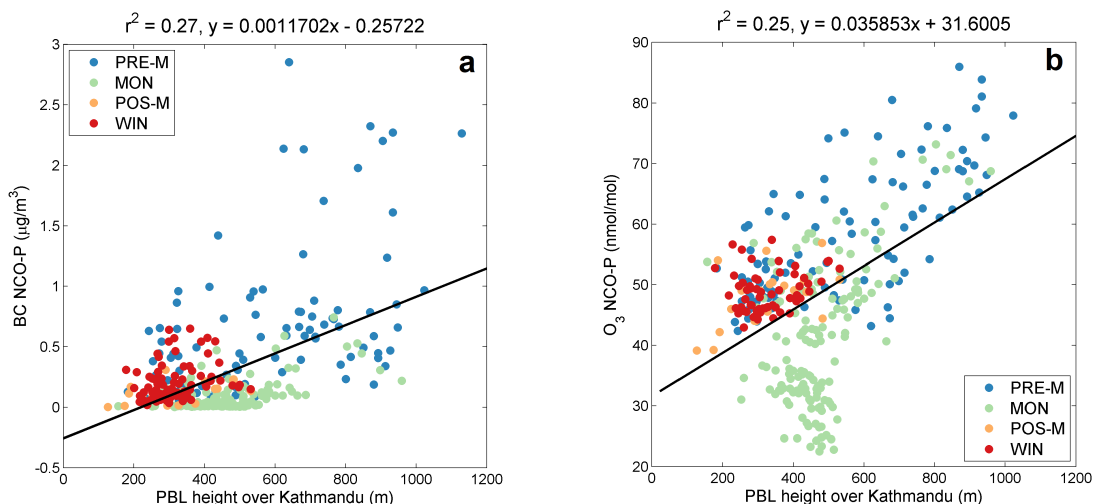


Figure 3.4: Scatter plots of daily average PBL height over Kathmandu, as a function of BC (a) and O_3 (b) concentrations at NCO-P. Colors indicate the different seasons. Also reported in the plot are the linear fits considering the entire datasets.

PBL height over a pixel that encloses the Kathmandu urban area, was analyzed. A similar approach was proposed by Raatikainen et al. (2014), who showed that the aerosol concentrations measured at the western Himalayan foothills were correlated with the spatially averaged PBL height over the Indo-Gangetic Plain. Carrying out a similar analysis for NCO-P is important for extending the findings by Raatikainen et al. (2014) to a broader Himalayan region.

Figure 3.4 shows the scatter plot of daily average PBL height over the Kathmandu urban area (as presented in Sect. 3.2.3) versus BC (panel a) and O_3 (panel b) concentrations at NCO-P, respectively. Colors in the plot indicate the different seasons, as defined in Sect. 3.3.1 and Table 2.1. Both parameters showed linear correlation ($r^2 = 0.27$ for BC, and $r^2 = 0.25$ for O_3 , respectively) with the PBL height over Kathmandu, suggesting that the latter can be an important parameter to explain the transport and SLCF/P variability at NCO-P. The linear correlation is maintained also when applied to each season separately. For BC, the seasonally-divided correlation is shown in Fig. 3.5, where colors indicate the CO values representative of the Kathmandu urban area (see Sect. 3.2.2). It has to be noted that the analysis for the post-monsoon is not as robust as in the other seasons, due to lower data availability, and thus will not be discussed here. The correlation remained high during pre-monsoon and monsoon ($r^2 = 0.27$ and $r^2 = 0.33$, respectively), with the highest BC values observed together with the highest CO retrievals, especially in the pre-monsoon. This suggests that the combustion processes occurring in the Kathmandu Valley can represent,

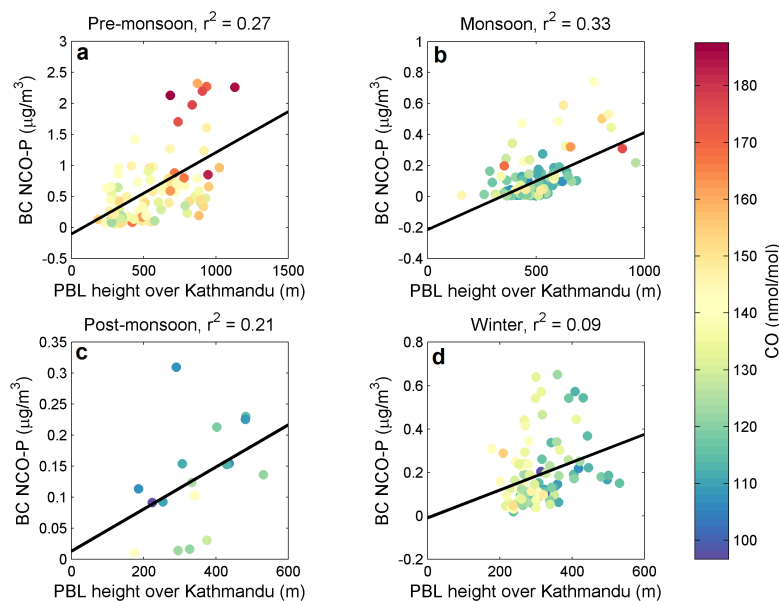


Figure 3.5: Seasonal scatter plots of daily average PBL height over Kathmandu as a function of BC concentrations at NCO-P. Colors indicate the CO value over Kathmandu, as retrieved by AIRS. Also reported in each plot are the linear fits.

under favorable PBL conditions, a source of BC at NCO-P. Similarly, seasonal O_3 correlations with PBL variations are shown in Fig. 3.6. Colors in this plot denote the NO_2 values over Kathmandu retrieved by OMI (see Sect. 3.2.2). As for BC, the highest correlation coefficients characterized the pre-monsoon and the monsoon ($r^2 = 0.49$ and $r^2 = 0.27$, respectively). Although the NO_2 levels showed large variability within each season (see Fig. 3.3d), the high NO_2 associated to high O_3 mixing ratios at NCO-P indicated the possibility that anthropogenic emissions occurring at Kathmandu could affect, after photochemical production and transport, the O_3 variability at NCO-P.

To provide a further evidence of the role played by the transport of polluted air-masses from Kathmandu towards NCO-P, back-trajectories were considered as a constraint in the correlation analysis. More specifically, the analysis was restricted only to days characterized by the presence of at least 3 % of daily back-trajectories from NCO-P which have crossed the PBL over Kathmandu. This was performed by checking, for each back-trajectory, if it crossed an idealized box of $0.5^\circ \times 0.5^\circ$ built considering Paknajol location as center, with the vertical extension given by the PBL height value. Since the temporal resolution for the back-trajectories is 2 h, at each point the altitude field was compared to the PBL height closest in time, thus resulting in a possible minor source of uncertainty.

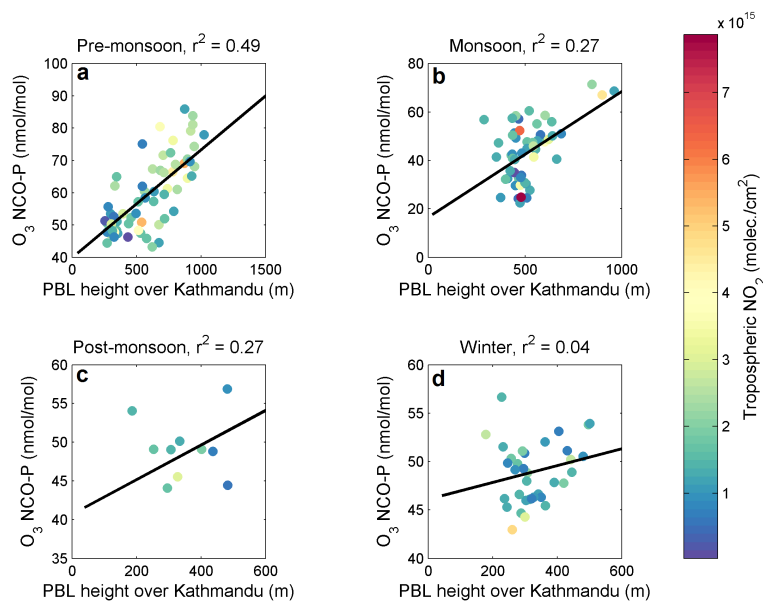


Figure 3.6: Seasonal scatter plots of daily average PBL height over Kathmandu as a function of O_3 concentrations at NCO-P. Colors indicate the tropospheric NO_2 column over Kathmandu, as retrieved by OMI. Also reported in each plot are the linear fits.

The choice of 3% was made after performing a sensitivity study, to partially compensate such uncertainties, as well as to give a robust identification of the possible transport.

Concerning the transport times, the frequency distribution of Δt , i.e., the time between the crossing of the PBL over Kathmandu and the arrival of the same air-mass at NCO-P (Fig. 3.7) showed that more than one quarter (26%) of the data presented values lower than one day, and 69% of the travel times were enclosed within 48 h. This is coherent with the results presented in Lüthi et al. (2015), who indicate that a relatively “fast” transport characterizes the travel of air-masses from the Indo-Gangetic Plain/Himalayan foothills to the Himalayas.

Fig. 3.8 shows the PBL height variations at Kathmandu, as a function of the BC and O_3 concentrations at NCO-P, on this selected subset of days only (9% of the period under study). To better represent the correct transport times for each x -th day, each BC and O_3 daily average at NCO-P was associated to the corresponding $(x + \overline{\Delta t})$ PBL height daily value, where $\overline{\Delta t}$ represents the median of all of the Δt values computed for each x -th day. Similarly, colors in the plots denote the BC and O_3 $(x + \overline{\Delta t})$ daily averages recorded at Paknajol. The value of the correlation coefficient between PBL height and BC at NCO-P increased from $r^2 = 0.27$ to $r^2 = 0.50$. The same behavior was observed for O_3 , with

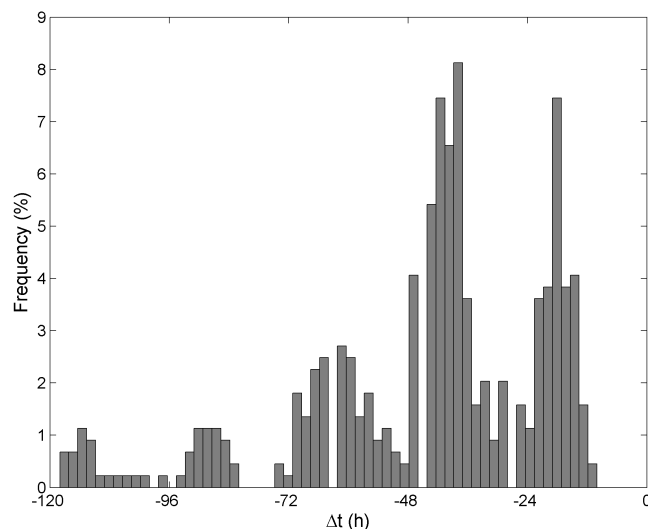


Figure 3.7: Distribution of Δt , i.e., the time difference (in hours) between the crossing of the PBL over Kathmandu and the arrival of the same air-mass at NCO-P.

an increase in the correlation coefficient from $r^2 = 0.25$ to $r^2 = 0.65$. Conversely, when considering days without back-trajectories crossing the PBL, the linear correlation was comparable to that considering all of the days, as displayed in Fig. 3.4 ($r^2 = 0.23$ and $r^2 = 0.22$ for BC and O_3 , respectively). It is interesting to note that the two points characterized by very high BC values at NCO-P in Fig. 3.8a correspond to the day (and the following one) in which the Nepali new year was celebrated in Kathmandu (i.e., April 14th, 2013). Indeed, in addition to the regular activities, increased emissions due to the celebrations (e.g., parades, festivals) can be observed at Kathmandu during these days. Under favorable transport conditions, these air-masses enriched in combustion by-products can travel up to the Himalayas and be detected at NCO-P.

3.4 Conclusions

This chapter reports the first full year (February 2013–January 2014) of continuous BC and O_3 measurements at two sites in Nepal, i.e., Paknajol in the Kathmandu Valley and the Nepal Climate Observatory-Pyramid in the southern Himalayas, and investigated the role of PBL and air-mass transport in affecting these SLCF/P variability over the southern Himalayas.

The two measurement sites are characterized by very different features: Paknajol is considered representative of the anthropogenic emissions that contribute

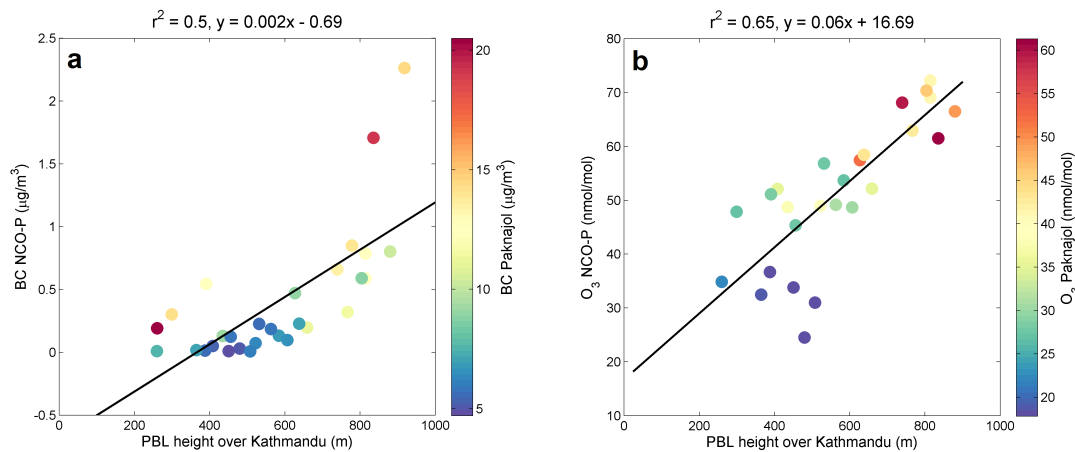


Figure 3.8: Scatter plots of daily average PBL height over Kathmandu as a function of BC (a) and O_3 (b) concentrations at NCO-P. Colors indicate the BC (a) and O_3 (b) daily values recorded at Paknajol. The displayed days are only those in which at least 3 % of back-trajectories starting at NCO-P have crossed the PBL over Kathmandu; moreover, for each day the median transport time was taken into account (as described in Sect. 3.3.3). Also reported in each plot are the linear fits.

to the poor air quality typical of the Kathmandu Valley, while NCO-P is a remote site, representative of the southern Himalayas free troposphere. BC and O_3 variations at both sites, which are characterized by a different seasonality, are naturally driven by the regional meteorology, and by “local” circulation systems (i.e., day-night wind variations).

A correlation study between the daily PBL height (derived from ERA-Interim) over a pixel that encloses the Kathmandu urban area, and the daily BC and O_3 concentrations at NCO-P, was conducted. The parameters showed linear correlation ($r^2 = 0.27$ for BC, and $r^2 = 0.25$ for O_3), that was maintained also within each season. Thus, the PBL height can be identified as a crucial parameter in determining the BC and O_3 variability at NCO-P. To provide a further indication of the role played by transport, another constraint in the analysis was included, i.e., back-trajectories starting at NCO-P. Despite the well-known limitations in using back-trajectories (calculated from meteorological fields with coarse horizontal and vertical resolution) in such a complex mountainous environment, they were adopted as an indicator of the possible transport between the two measurement sites. An increase in the correlation coefficients between the PBL height and BC and O_3 was observed, in days (9 % of the period under study) characterized by the arrival of air-masses at NCO-P, which have crossed the PBL over the Kathmandu urban area ($r^2 = 0.50$ and $r^2 = 0.65$ for BC and O_3 , respectively). Conversely, when transport was not observed, a decrease in r^2

was detected for both parameters.

The analysis of the linear correlation with daily PBL height values indicates that 50 % and 65 % of the BC and O₃ variability at NCO-P can be explained by the PBL variations over the Kathmandu urban area, in days in which air-masses crossing that source region and then arriving at NCO-P are observed. It is also worth noting that, during these days, the highest BC and O₃ values at NCO-P corresponded to the highest BC and O₃ concentrations measured at Paknajol, further indicating a clear evidence for what concerns the transport of such harmful air pollutants from a regional “hot spot” to a remote region in the Himalayas, representing a threat for the whole southern Himalayan environment.

STEFLUX, a tool for investigating stratospheric intrusions, and its application to NCO-P

Stratospheric intrusion (SI) events are a topic of ongoing research, especially because of their ability to change the oxidation capacity of the troposphere and the transport of O₃ from the stratosphere, with the consequent contribution to tropospheric O₃ levels. In this chapter, a novel tool called STEFLUX (Stratosphere-to-Troposphere Exchange Flux) is presented, discussed, and used to provide a first long-term investigation of SI over the southern Himalayas. The main purpose of STEFLUX is to obtain a fast-computing and reliable identification of the SI events occurring at a specific location and during a specified time window. It relies on a compiled stratosphere-to-troposphere exchange (STE) climatology, which makes use of the ERA-Interim reanalysis dataset from the ECMWF, as well as a refined version of a well-established Lagrangian methodology. STEFLUX results are compared to the SI observations (SIO) at the high-mountain WMO/GAW global station Nepal Climate Observatory-Pyramid (NCO-P, 5079 m a.s.l.), which is often affected by SI events. Compared to the observational dataset at this specific measurement site, STEFLUX is able to detect SI events on a regional scale. Furthermore, it has the advantage of retaining additional information concerning the pathway of stratospheric-affected air-masses, such as the location of

A modified version of this chapter has been published as: Putero, D., Cristofanelli, P., Sprenger, M., Škerlak, B., Tositti, L., and Bonasoni, P.: STEFLUX, a tool for investigating stratospheric intrusions: application to two WMO/GAW global stations, *Atmos. Chem. Phys.*, 16, 14203–14217, 2016.

tropopause crossing and other meteorological parameters along the trajectories. However, STEFLUX neglects mixing and dilution that air-masses undergo along their transport within the troposphere. Therefore, the regional-scale STEFLUX events cannot be expected to perfectly reproduce the point measurements at NCO-P, which are also affected by small-scale (orographic) circulations. Still, the seasonal variability in SI events according to SIO and STEFLUX agrees fairly well. By exploiting the fact that the ERA-Interim reanalysis extends back to 1979, the long-term climatology of SI events at NCO-P is also assessed in this chapter. The analysis of the 35-year record at NCO-P denies the existence of any significant trend in the SI frequency, except for winter seasons. Furthermore, for the first time, by using the STEFLUX outputs, the potential impact of specific climate factors (i.e., ENSO, QBO, and solar activity) on SI frequency variability over the Himalayas is investigated. Given the STEFLUX capability in reproducing the transport conditions, the SI influence on O₃ and BC concentrations at NCO-P is also assessed here, indicating statistically significant increases (decreases) in O₃ (BC) concentrations, in days not affected by acute pollution events due to the valley transport.

4.1 Introduction

Stratosphere-to-troposphere exchange (STE) represents one of the natural processes that have substantial impacts on meteorology and atmospheric chemistry, and is an important aspect of climate change (Appenzeller and Davies, 1992; Holton et al., 1995; Stohl et al., 2003; Stevenson et al., 2006). The definition of STE encompasses a two-way air-mass transport: the downward transport from the stratosphere to the troposphere (STT) and the upward transport from the troposphere to the stratosphere (TST). A specific type of STT is called stratospheric intrusion (SI), which is defined as the downward transport of stratospheric air-masses relatively deep into the troposphere. SI events are capable of changing the oxidation capacity of the troposphere (Gauss et al., 2003) and their contribution to the O₃ levels in the troposphere has been estimated to be as large as the net photochemical production (Roelofs et al., 1997), although models still show large uncertainties in the estimates (e.g., Stevenson et al., 2006; Naik et al., 2013). As pointed out in many studies (e.g., Reed, 1955; Appenzeller and Davies, 1992; Lamarque and Hess, 1994; Holton et al., 1995; Appenzeller et al., 1996; Stohl et al., 2003; Cooper et al., 2005; Sprenger et al., 2007) SI events can be caused by different mechanisms and are typically associated to distinct synoptic- and mesoscale features: tropopause folds and cutoff lows, subtropical jet streams and streaks, potential vorticity (PV) streamers, upper-level fronts, and anticyclonic areas.

High-mountain stations are appropriate sites for investigating the transport of stratospheric air-masses into the troposphere, because stratospheric air-masses can already be identified at mid-tropospheric levels. Furthermore, they are less influenced by polluted air-masses due to local or regional anthropogenic emissions (Stohl et al., 2000), which makes SI detection more straightforward. Several studies have been carried out in the past to assess the influence of SI at high-altitude remote sites, which also represent ideal locations for studying the background conditions of the troposphere (e.g., Stohl et al., 2000; Cristofanelli et al., 2006; Ordóñez et al., 2007; Cristofanelli et al., 2010; Trickl et al., 2010; Lin et al., 2012). Usually, stratospheric influence is detected at a measurement site by analyzing the variability of in situ “stratospheric” tracers (e.g., relative humidity, ^7Be , ^{10}Be , O_3 , atmospheric pressure variability) and profiling datasets (radio/ozonesondes), coupled with the analysis of satellite (e.g., total column of ozone) and various kinds of numerical weather prediction (NWP) model products. Many different methods, as thoroughly reviewed in Stohl et al. (2003), are based on this combined approach. Stohl et al. (2000) deployed a detection algorithm based on the in situ variation in experimental data and simulations with a passive stratospheric tracer. Similarly, other studies have analyzed STE by coupling experimental data and back-trajectories (e.g., Cristofanelli et al., 2006, 2010; Trickl et al., 2010). Usually, specific threshold values are applied to in situ tracers variability to detect the presence of air-masses with stratospheric “fingerprints”. Also, trajectory and dispersion models are extensively used to detect the occurrence of STE. For example, Cui et al. (2009) used the particle dispersion model FLEXPART (Stohl et al., 2005) and the trajectory model LAGRANTO (Wernli and Davies, 1997) to identify stratospheric transport at the high-altitude Alpine site Jungfraujoch (Switzerland), while Tarasova et al. (2009) deployed 3-D air-mass back-trajectories to trace the atmospheric transport at two high-mountain measurement sites over the Alps and Caucasus. As pointed out by Bourqui (2006), trajectory-based approaches can provide a lower-bound estimate for STE flux, while dispersion models can provide slightly larger estimates. Typically, when used to detect STE at specific locations at the Earth’s surface, all of these “observation-based” methodologies vary among different measurement sites, with respect to the number and types of stratospheric tracers available/considered and threshold values adopted, and often require a lot of time-consuming implementation to work. Moreover, it should be argued that none of the most diffused tracers have a “pure” stratospheric origin; for example, ^7Be and O_3 are affected by significant tropospheric sources. Furthermore, the compilation of proper long-term climatologies is very often hindered by the lack of long-term observations of “stratospheric” tracers.

This chapter presents a novel tool, which aims at objectively identifying SI

events reaching a “target” geographical region and during a specific time window. The tool, called STEFLUX (Stratosphere-to-Troposphere Exchange Flux), is a relatively fast-computing algorithm which makes use of the pre-computed trajectories composing the STE climatology by Škerlak et al. (2014). This climatology is available from 1979 and continuously updated. The Lagrangian approach on which it is based has been extensively used in previous studies (e.g., Wernli and Bourqui, 2002; Sprenger and Wernli, 2003; Bourqui, 2006; Sprenger et al., 2007; Škerlak et al., 2014) and has been confirmed to effectively identify SI events and to reproduce several of their related aspects. Its computational speed and user-friendly approach (it is sufficient to specify only a few parameters to work) make it suitable for obtaining a quick and reliable estimate of the SI events occurring at a specific place over the desired time window (including long periods which would otherwise require a lot of time-consuming calculations). A potential use of STEFLUX is to identify the SI occurrence in locations where a detection based on observational data is not available. To evaluate the STEFLUX skills in identifying the SI events, its outputs are compared with the SI identification based on observations at the high-altitude Nepal Climate Observatory-Pyramid WMO/GAW global station in Nepal. Then, STEFLUX is used to provide a first investigation on the long-term (i.e., 1979–2013) variability in SI occurrence at this measurement site. In particular, a first assessment of the possible impact of large-scale climate processes (i.e., ENSO, QBO, and solar activity) in modulating the long-term SI variability is given.

This chapter is structured as follows. Sect. 4.2 defines the selection methodologies that were used for identifying SI events at the two measurement sites, and Sect. 4.3 describes in detail the STEFLUX tool, along with a case study to show a potential application. STEFLUX time series is then compared to the in situ measurements in Sect. 4.4, followed by a critical discussion about the benefits and restrictions of the tool. Furthermore, trends and periodicities of the long-term SI time series at NCO-P are assessed, as well as the SI influence on O₃ and BC concentrations. Finally, Sect. 4.5 summarizes the main results.

4.2 Experimental dataset

Datasets of daily SI occurrences are available at the high-altitude WMO/GAW global station Nepal Climate Observatory-Pyramid (NCO-P, 5079 m a.s.l., Nepal) starting from 2006. In this section, a brief description of the measurement site is provided, together with the description of the methodology used to detect SI events based on the analysis of in situ stratospheric tracers’ variability (coupled with additional model data). Hereinafter, this dataset will be referred to as “stratospheric intrusion observations” (SIO). Technical details on the different

parameters considered are given in the Supplement (Sect. A.2) and in the paper by Cristofanelli et al. (2010).

To account for days likely affected by SI events at NCO-P (please refer to Chapter 3 for the measurement site description), a specifically designed statistical methodology was applied to the time series of observed and modeled variables. The parameters used consisted of in situ measurements (O_3 ; atmospheric pressure, P ; and relative humidity, RH), satellite observations (total column of O_3 , TCO, as retrieved by the Ozone Monitoring Instrument, OMI) and NWP-based back-trajectories (by using LAGRANTO, see Sprenger and Wernli, 2015; Wernli and Davies, 1997). The methodology is composed of four different criteria; at least one must be satisfied to identify a day as likely influenced by SI:

1. significant variations in daily P values and presence of back-trajectories with values of $PV > 1.6$ pvu;
2. significant daily TCO increases and presence of back-trajectories with values of $PV > 1.6$ pvu;
3. significant variations in daily P values and significant TCO daily increases;
4. the presence of RH values lower than 60 % and significant negative correlation of O_3 - RH and daily O_3 maximum higher than the seasonal value and significant variation in daily P , PV , or TCO values (this last criterion was introduced for taking into account the possible role of downward valley winds in transporting air-masses from aloft).

The identification of periods characterized by significant variations is obtained as follows: first, three iterations of a 21-day running mean (the so-called Kolmogorov-Zurbenko filter; see Sebald et al., 2000) is applied to the daily average time series, and residuals are calculated by subtracting these values from the daily averages; thereafter, a check is performed to determine whether residuals exceed the upper or lower endpoints of the 95 % confidence interval of the residuals distribution over the whole period. The period of study considered spans from March 2006 to December 2013.

SIO at this measurement site provide a unique opportunity to test the capacity of STEFLUX in reproducing the main features of SI occurrences (frequency, seasonality, long-term variations) at a location representative of the subtropics.

4.3 The STEFLUX tool

4.3.1 Description of the tool

The main purpose of STEFLUX is to obtain a fast-computing and reliable estimation of SI occurring at a specific location. The database used as input relies on the trajectories from the STE climatology presented in Škerlak et al. (2014), which makes use of the ERA-Interim reanalysis dataset from the ECMWF (Dee et al., 2011), as well as a refined version of a well-established Lagrangian methodology (Wernli and Bourqui, 2002), to calculate mass and ozone fluxes across the tropopause and several pressure surfaces. For further details, please refer to Škerlak et al. (2014).

STEFLUX detects the air parcels originating in the stratosphere and entering a tropospheric 3-D target box during a specific time window. For this reason, several parameters need to be defined for the STEFLUX tool to work: (i) the time period for which the analysis should be carried out, and (ii) the target box by means of its longitude and latitude boundaries and by its vertical extension from the surface up to the top boundary (defined as a pressure level, in hPa). On request, the PBL height can be used as the top boundary of the target box: this option takes into account the ERA-Interim PBL height, which is a parameter also available along each STE trajectory. In addition to this, another optional parameter allows the temporal resolution for the STE trajectories to be increased from its default value (6 h) up to 1 h. STEFLUX produces several output files; these enclose (i) the trajectory positions and timing found within the box, (ii) the first box crossing positions and timing for each trajectory, (iii) the tropopause crossing position and timing for each trajectory, and (iv) the complete list of the trajectories that have crossed the box.

4.3.2 Illustrative case study

To present an application of STEFLUX and its output files, a SI case in January 2007 is discussed. The period of study coincides with a case study discussed in Bracci et al. (2012), where the SI event was strongly related to the subtropical jet stream. A box with horizontal extension 85–88° E and 26–29° N, centered at NCO-P, was defined. The top boundary of the box was taken at 550 hPa (the average pressure at the station), while the STEFLUX tool was run for the time period 9–25 January 2007. All STE trajectories from the climatology by Škerlak et al. (2014), introduced in Sect. 4.3.1, were analyzed and their crossings of the target box boundaries determined.

Figure 4.1a shows as a time series the number of the daily crossings (derived from the STE trajectories) in the box, according to STEFLUX. Additionally, the

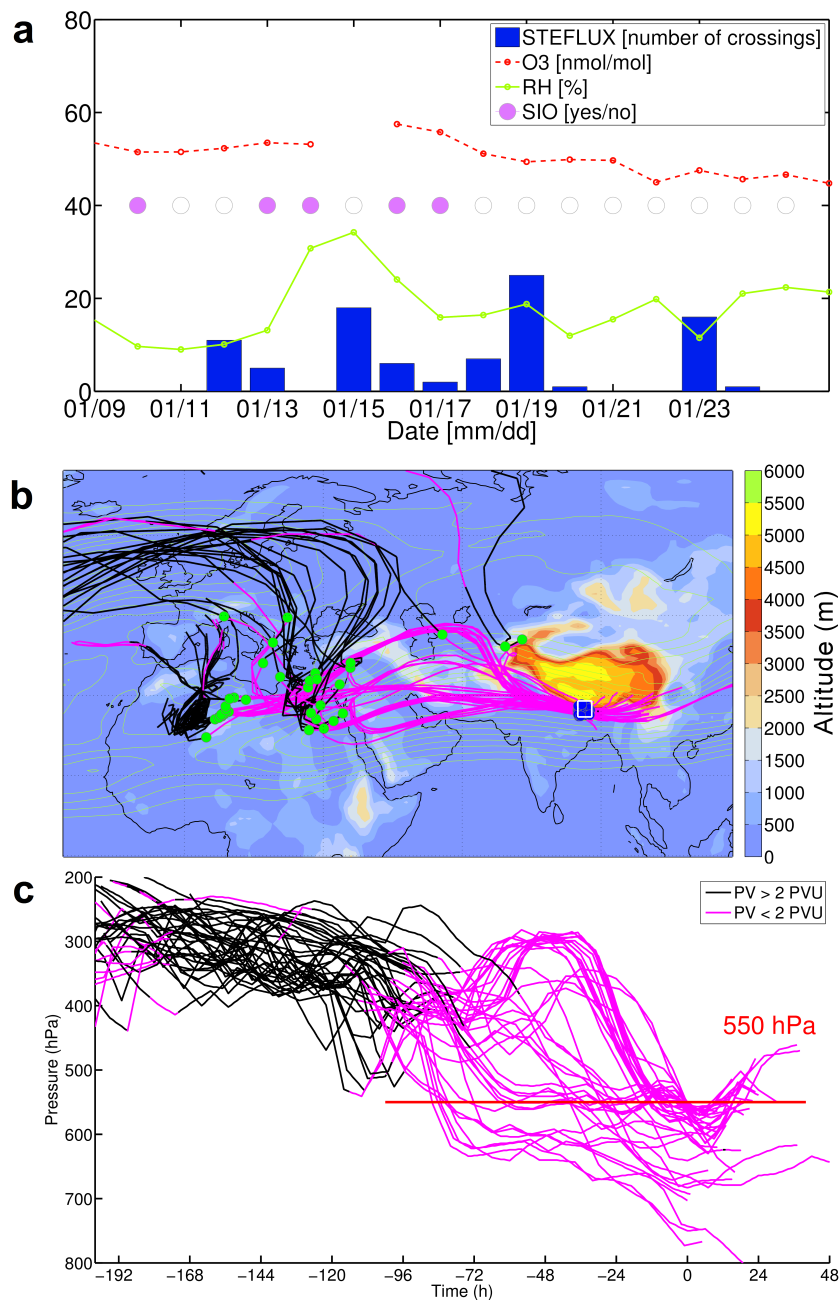


Figure 4.1: Example of application of STEFLUX, in a target box around NCO-P position over the period 9–25 January 2007. Panel (a) shows the daily averages for O₃ and RH at NCO-P, the days selected by the SIO methodology (see Sect. 4.2) and the number of STE trajectory points crossing the box. The STE trajectories are also displayed entirely in (b), where blue dots indicate the first crossings of the target box and green dots identify the tropopause crossing locations. Contour lines indicate the wind speed at 250 hPa, averaged over the case study period. Panel (c) shows the time–height evolution of the selected trajectories (0 is the time of arrival into the target box), as a function of the PV value along each trajectory point.

daily averaged values for O_3 and RH at NCO-P are shown, and each day is also marked as selected or not by the SIO methodology, according to the criteria introduced in Sect. 4.2. The study period was characterized by the presence of clean and dry (daily RH average always below 40 %) air-masses; moreover, the double-jet structure of wind speed at 250 hPa (contour lines in Fig. 4.1b) indicated the presence of the subtropical jet stream over south Asia and the Himalayas. SIO methodology identified a likely SI event, spanning from 13 to 17 January 2007 (the missing record of O_3 during 15 January was responsible for the gap in the SIO time series). This was confirmed by STEFLUX: from 12 to 24 January 2007, several STE trajectories passed through the target box; at its peak, 25 daily crossings were counted. This time series is directly based on two STEFLUX output files, which list the first and the entire trajectory positions found within the target box. In addition to the crossing time, the list of variables includes the position (longitude/latitude/pressure) and several meteorological parameters (e.g., potential temperature, specific and relative humidity, PBL height) at each point within the target box.

The first positions of the air parcels after entering the target box are marked in Fig. 4.1b as blue dots; additionally, the positions where the air parcels crossed the dynamical tropopause are shown as green dots. Interestingly, these crossings are mainly clustered into a region over north Africa, which is identified as a preferred region for tropopause crossing in previous studies (Sprenger and Wernli, 2003; Škerlak et al., 2014), and also in this study (see Sect. 4.4.2). The exact times and positions of the tropopause crossings are saved by STEFLUX in a third output file, together with atmospheric pressure, potential temperature, and O_3 concentration. The output files from STEFLUX allow the history of the STE air parcels to be studied along their way from the stratosphere to the target box. As an example, Fig. 4.1b reports all the trajectories from the tropopause crossings (green dots) to the target box (blue dots). These trajectories are colored according to their PV value, i.e., points below 2 pvu (magenta) and points greater than 2 pvu (black). Figure 4.1c shows the time–height evolution of the trajectories, where time is given relative to the arrival time in the target box. Additionally, the top boundary height of the target box (550 hPa) is reported in the figure (red horizontal line). It is discernible that most of air parcels slowly descended until 72–48 h before they reached the box. Previously, they were characterized by PV values above 2 pvu (black line) – i.e., they still followed the stratospheric circulation steered by the subtropical jet stream (as also discernible from the contour lines of wind speed at 250 hPa in Fig. 4.1b, which mark the double-jet structure). A rapid descent then set in before their arrival; hence, the PV falls below 2 pvu, indicating that the air parcels crossed the dynamical tropopause.

4.4 Results

4.4.1 STEFLUX vs. SIO

In this section, the SI occurrences from STEFLUX are compared to the ones from SIO at the WMO/GAW global station (see Sect. 4.2). STEFLUX was run by setting a target box with a horizontal extension of $3^\circ \times 3^\circ$ around the measurement site, after performing a sensitivity test on this parameter (not shown). Vertically, the box extended up to 550 hPa, corresponding to the average pressure level recorded at the station throughout the year. The selected time period was the same as in Sect. 4.2 (i.e., March 2006–December 2013), but the temporal resolution for the STE trajectories was increased to 1 h (see Table 4.1 listing all of the input parameters).

The aim of this part is twofold: first, seeing how STEFLUX compares to SIO. This comparison, which turns out not to be a perfect match, will lead to a critical discussion of what can and cannot be expected from STEFLUX. Hence, it is paramount to understand that both STEFLUX and SIO have complementary strong and weak points in identifying SI events and thus may not be exactly compared one to one.

Seasonal comparison and interannual variability

The seasonal frequency (in %) of SI days, derived from measurements (SIO), is presented in Fig. 4.2 as a red line. Additionally, the seasonally averaged percentage of available data from each criterion (hereinafter referred to as “criteria coverage”) is also reported in the plot (gray bars). Differently from Chapter 3, seasons in this chapter are defined (for simplicity) as: winter (DJF), pre-monsoon (MAM), monsoon (JJAS), and post-monsoon (ON). A clear seasonality characterized the SIO frequency at NCO-P, as highlighted by the seasonally averaged SI frequencies obtained. A maximum (Fig. 4.3a) was discernible in winter and a minimum during the monsoon season. The same time series of seasonal frequen-

Table 4.1: Input parameters for STEFLUX for the comparison with in situ measurements (SIO).

Parameter	
Lat_min, Lat_max	26° N, 29° N
Lon_min, Lon_max	85° E, 88° E
Box_top	550 hPa
Time span	01 Mar. 2006–31 Dec. 2013
Temporal resolution	1 h

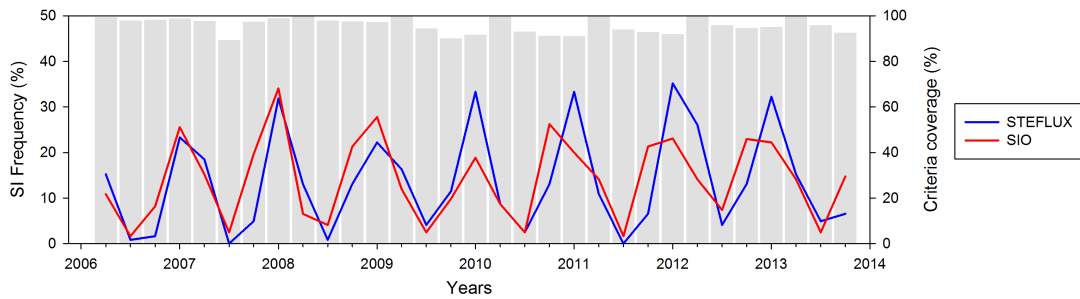


Figure 4.2: Seasonal graph of SI frequency at NCO-P. Blue lines indicate the STEFLUX outputs (for the configuration parameters see Table 4.1), while the red ones represent the results from the application of the criteria presented in Sect. 4.2 (SIO). Also shown in the plot is the percentage of criteria coverage (gray bars) for each season.

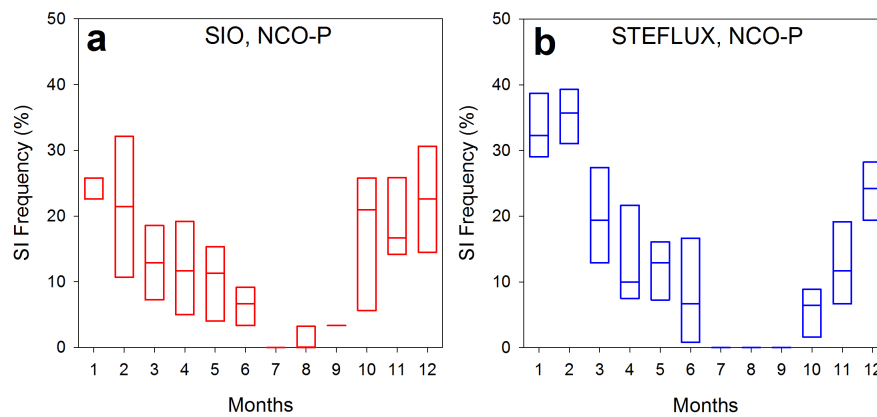


Figure 4.3: Box-and-whisker plot of the annual variation in SI frequency at NCO-P. Both the SIO (a) and STEFLUX (b) values are presented.

cies using STEFLUX (blue lines in Fig. 4.2) was computed, with a threshold of at least two box crossings per day, in order to retain robust information only and to discharge “erratic” events. It showed a clear average seasonality (Fig. 4.3b), comparable and consistent with that from SIO (Fig. 4.3a).

Although the seasonality was a feature well captured by STEFLUX, the interannual variability was less clearly identifiable. As shown in Fig. 4.2, the correlation between the two seasonal time series was rather high (Pearson’s $r = 0.7$), but for specific years STEFLUX and SIO results evidently differed in the amplitude and timing of the annual peaks. In particular, SIO showed much higher SI frequency than STEFLUX for post-monsoons during 2010–2012. When comparing seasons individually, the correlation coefficient was satisfying for pre-monsoon, monsoon, and post-monsoon ($r = 0.5$ on average). For winter, the

Table 4.2: The 2×2 contingency tables for the comparisons of the SI event time series, i.e., identified by the SIO and STEFLUX approaches. For each table the odds ratio skill score (ORSS) is also reported, along with the minimum ORSS required to have real skill at the 99 % confidence level (in parentheses; see Thornes and Stephenson, 2001). Capital letters are defined as follows: *A* indicates the number of SI events selected by both methodologies (STEFLUX and SIO), *B* represents the number of events selected as SI by the first methodology but as no-SI by the second one, *C* represents the number of events selected as no-SI by the first methodology but as SI by the second one, and *D* represents the number of no-SI events selected by both methodologies.

(a)		SIO vs. STEFLUX		(b)		STEFLUX vs. SIO	
		STEFLUX				SIO	
		SI	no-SI			SI	no-SI
SIO	SI	$A = 55$	$B = 148$	STEFLUX	SI	$A = 39$	$B = 116$
	no-SI	$C = 23$	$D = 181$		no-SI	$C = 16$	$D = 140$
ORSS		0.49 (0.35)		ORSS		0.49 (0.35)	

two time series are even anti-correlated ($r = -0.4$). This can be attributed to a significant decrease of SI detection by SIO during winter for the years 2009–2010.

Event-based comparison

In this section, the comparison is extended to a higher temporal resolution, i.e., by considering single SI events. More specifically, in this study, a SI event was defined (for both STEFLUX and SIO) as the aggregation of contiguous SI days. Furthermore, cases in which two distinct SI events were separated by a single no-SI day were treated like a single event covering the entire period. Generally, an event-based comparison between modeled and observed SI events and experimental detection is a very challenging task, as pointed out by previous investigations, concerning the transport and mixing of stratospheric air deep into the troposphere (e.g., Meloen et al., 2003; Cui et al., 2009; Bracci et al., 2012).

Based upon the SIO criteria, a total of 203 SI events (361 days influenced by SI, representing 13 % of the period) were identified, with duration ranging from 1 to 14 days and an average length of 1.9 days. On the other hand, STEFLUX identified 155 SI events (376 days, 13 %), with duration ranging from 1 to 10 days (average length: 2.6 days).

To assess the STEFLUX performance, the approach presented in Cui et al. (2009) was followed. First, all SI events as retrieved by SIO were considered, and then it was checked whether at least 50 % of the duration of each SIO event was confirmed by STEFLUX. If this was the case, STEFLUX was considered able to capture the selected SIO event. Hereinafter, this comparison will be referred to

as “SIO vs. STEFLUX”. Conversely, the “STEFLUX vs. SIO” comparison checked whether a SI event (as defined by STEFLUX) was confirmed by the SIO dataset.

For an overview of the results of this comparison, contingency tables were computed (Table 4.2). In these 2×2 tables, each entry encloses a list of SI or no-SI events, as defined by the methodology considered (STEFLUX and SIO). From the contingency tables it is possible to evaluate several skill scores, which are useful to measure the skill of one method in identifying SI events compared with the other one. The accuracy (ACC), false alarm ratio (FAR), and probability of false detection (POFD) skill scores are defined, according to Thornes and Stephenson (2001) and Wilks (2006), as

$$\text{ACC} = \frac{A + D}{A + B + C + D}, \quad (4.1)$$

$$\text{FAR} = \frac{B}{A + B}, \quad (4.2)$$

$$\text{POFD} = \frac{B}{B + D}, \quad (4.3)$$

where, for each contingency table, A represents the number of SI events selected by both methodologies (STEFLUX and SIO), B represents the number of events selected as SI by the first methodology but as no-SI by the second one, C represents the number of events selected as no-SI by the first methodology but as SI by the second one, and D represents the number of no-SI events selected by both methodologies. Both contingency tables give identical values of ACC (0.58) and POFD (0.45), while FAR was 0.73 and 0.75. The rather high FAR values and low POFD values can be partially explained by considering that the occurrence of SI is a relatively “unlikely” event with respect to the occurrence of no-SI. Also, for taking into account this point, an additional parameter was considered (i.e., the odds ratio skill score, ORSS; see Thornes and Stephenson, 2001), which is not influenced by the marginal totals (i.e., $A + C$ and $B + D$). This parameter is defined as

$$\text{ORSS} = \frac{A \times D - B \times C}{A \times D + B \times C}. \quad (4.4)$$

The ORSS varies between -1 and $+1$, where a score of 1 represents perfect skill and a score of 0 indicates no skill; negative values imply that values of one series are opposite to what observed by the other one. Also reported in each table is the minimum ORSS required to have real skill at the 99% confidence level (see Thornes and Stephenson, 2001). All of our combinations indicate that the agreement between the methodologies is not due to chance (i.e., is statistically significant).

Table 4.3: SIO vs. STEFLUX: agreement between STEFLUX and the measured SI events (SIO). STEFLUX vs. SIO: agreement between the measured and the modeled (by using STEFLUX) SI events, as a function of the different length of the SI events.

SI event duration	SIO vs. STEFLUX		STEFLUX vs. SIO	
	SI events by SIO	STEFLUX	SI events by STEFLUX	SIO
1 day	117	25 (22 %)	55	7 (13 %)
2 days	41	17 (42 %)	36	15 (42 %)
3 days	20	4 (20 %)	22	7 (32 %)
≥ 4 days	25	9 (36 %)	42	10 (24 %)
Total	203	55 (27 %)	155	39 (25 %)

The left side of Table 4.3 focuses on the SIO vs. STEFLUX comparison, as a function of the length of the different events. STEFLUX captured one-quarter of the measured events for NCO-P. The highest agreement was found for 2-day events (42 %). In particular, all the longest events were confirmed by STEFLUX (9- and 14-day-long events). Finally, the STEFLUX vs. SIO approach is correspondingly assessed in the right side of Table 4.3. One-quarter of the SI events observed by STEFLUX were confirmed by SIO (25 %). Again, the maximum agreement was found for events that lasted 2 days, while the minimum agreement was assessed for 1-day-long events.

STEFLUX and SIO: strong and weak points

Several possible reasons can explain the mismatch between the SIO and STEFLUX time series. For instance, STEFLUX is not fully able to capture subgrid-scale processes (like convection, turbulent diffusion, and mixing) along the path from the stratosphere to the target region. This deficiency becomes particularly pronounced over mountainous measurement sites, mostly because of the complex topography and the associated small-scale thermally and dynamically driven circulations that characterize the area. As shown in Bracci et al. (2012), it is common that stratospheric air-masses reach the upper tropospheric layers over NCO-P, without directly arriving at the station altitude. Then, the stratospheric air is entrained and mixed within the PBL and thus brought to the measurement station. It was for this reason that a specific criterion was introduced in the SIO detection methodology at NCO-P (see criterion 4 in Sect. 4.2). It is worth noting that for NCO-P the largest bias between STEFLUX and SIO was observed when this criterion dominated the detection of SI (post-monsoons 2010 and 2011). Since the mixing processes might take several hours, this could be the reason of the lower agreement between SIO and STEFLUX.

In the case of long travel times from the tropopause to the target region, a stronger impact of mixing and dilution processes on the air-mass properties is expected. Hence, when a SI actually affects a specific region, the SIO criteria might not be able to detect it, because mixing and dilution with tropospheric air-masses could lower stratospheric tracers concentrations below the thresholds used for detection. Then, the travel times (hereinafter called Δt , expressed in hours) between the tropopause crossing and the first box crossing, for each SI event, were computed. To evaluate the possible dependence from the travel time as a function of seasons, Δt was sorted into five categories (from 0 to 120 h, divided into 24 h intervals), and then the seasonal occurrence for each category was calculated (Fig. 4.4). The maximum value for Δt was chosen according to the typical lifetime values for a stratospheric intrusion into the troposphere (see Stohl et al., 2000; Bourqui and Trépanier, 2010; Trickl et al., 2014, 2016). On average, one-third (32 %) of the SI events identified by STEFLUX presented maximum travel times ($96 \text{ h} \leq \Delta t < 120 \text{ h}$). Furthermore, SI events characterized by relatively long (i.e., $\Delta t \geq 72 \text{ h}$) travel times usually dominated all the seasons. This suggests that a significant impact of dilution/turbulence small-scale processes along stratospheric air-mass transport is likely and might explain part of the mismatch between STEFLUX and SIO. This hypothesis was further confirmed by analyzing the events seen by STEFLUX, but not confirmed by SIO, as a function of Δt : most of them (86 %) were characterized by medium/long travel times (i.e., $\Delta t \geq 48 \text{ h}$).

A further point of discrepancy between STEFLUX and SIO results is related to the “overpasses” phenomenon, i.e., air-masses that overpass the station at altitudes high enough that there is no indication in the measurements record (but might be observed by STEFLUX). Indeed, during a study conducted at the Zugspitze (Germany, 2962 m a.s.l.), Trickl et al. (2010) showed that overpasses explained nearly the 20 % of occurrences that were not identified by the observations. Furthermore, for NCO-P, it should be considered that the station is located in a narrow valley. Thus, it is conceivable that, during the transport within the valley, O_3 (one of the stratospheric tracers considered by SIO) experiences deposition phenomena, thus decreasing the actual concentration that the stratospheric air-mass would have in the free troposphere (see, e.g., Furger et al., 2000; Wotawa and Kromp-Kolb, 2000).

In summary, although correctly depicting the typical seasonal variability in SI frequency, the STEFLUX and SIO time series differ for several reasons. These differences point out that the complete approach to study and assess SI is to deploy together modeling tools and observations, because they are complementary and address together several scientific questions. In particular, in situ observations have the advantage of capturing short and transient SI events

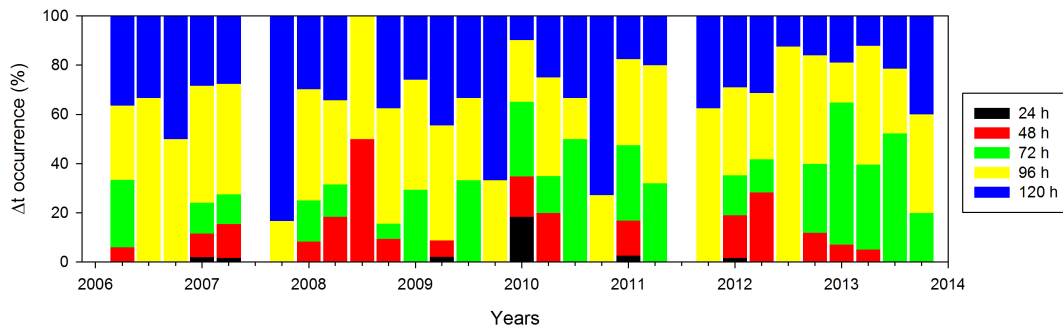


Figure 4.4: Seasonal graph of Δt occurrence (in %, Δt is defined as the time in hours between the tropopause crossing and the first box crossing) for the SI events identified by STEFLUX (blue line in Fig. 4.2). Colors in the legend refer to the upper limit of each Δt category, e.g., 24 h refers to $0 \text{ h} \leq \Delta t < 24 \text{ h}$.

associated to transport processes occurring at subgrid scales, while STEFLUX has the advantage of detecting the arrival of stratospheric-affected air-masses, irrespective of the degree of mixing and dilution along the transport within the troposphere.

4.4.2 Long-term evaluation of SI occurrences at NCO-P

SI events climatology

This section presents a climatology of SI events, as defined in Sect. 4.4.1, for the whole STEFLUX dataset (back to 1979, i.e., when the trajectories from the ERA-Interim reanalysis were first available). This allowed us to cover a 35-year period (1979–2013) of monthly SI frequency values. In total, 673 SI events at NCO-P were obtained (representing 13 % of the period), with an average length of 2.6 days. The percentage of events with length equal to or less than 4 days was very high (86 %), considering all data, with peaks up to 98 % in the summer season; on the other hand, the longest events were observed during winter. The seasonal cycle was also computed for this longer time series (see Fig. A.2, Supplement); the seasonality considering all monthly data was confirmed and comparable to that obtained in Fig. 4.3, for both measurement sites.

An important aspect of SI is where and when the SI trajectories actually crossed the tropopause. First, the location of the crossing is useful to determine the O_3 concentration of the air parcels at the start of their tropospheric path towards the target region. Second, as mentioned in Sect. 4.4.1, it is expected that a longer time since the tropopause crossing goes along with enhanced dilution

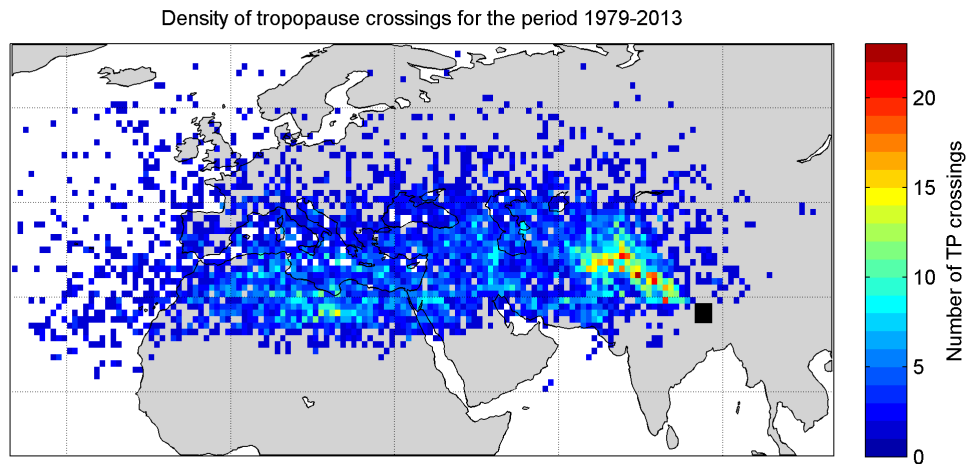


Figure 4.5: Density of tropopause (TP) crossings for the period 1979–2013, for NCO-P. Values for both figures were aggregated on a $1^\circ \times 1^\circ$ horizontal grid. The black square indicates the horizontal extension of the STEFLUX box.

until its arrival in the target region, although keeping in mind that the diluting processes along the path can be highly transient and nonlinear in time. As introduced in Sect. 4.3.2, STEFLUX allows the position and time of the tropopause crossings to be analyzed. This allowed us to compute a tropopause crossing density plot over the entire 35-year period, as presented in Fig. 4.5. The tropopause crossings associated with SI events are predominantly found over two areas, i.e., central Asia and northeastern Africa, close to the Mediterranean Sea. These results agree with previous climatological studies (Sprenger and Wernli, 2003; Škerlak et al., 2014), which indicated that the tropopause crossing predominantly occurs over the Atlantic and Pacific storm track regions (in winter, spring, and autumn), over the Mediterranean (in winter and spring) and over southeastern Europe and central Asia (in summer). The tropopause crossing locations were then categorized according to Δt (defined in Sect. 4.4.1) (see Fig. A.3, Supplement). The central Asia zone of tropopause crossing was pronounced for all Δt categories, up to 96 h, while the northeastern Africa cluster was absent for events with low Δt and clearly discernible for events with $48 \text{ h} \leq \Delta t < 72 \text{ h}$, stressing the importance, for the southern Himalayas, of the fast transport of stratospheric air-masses embedded within the subtropical jet stream (Bracci et al., 2012).

SI frequency long-term trends and variability

To detect potential trends in the SI frequencies, the same STEFLUX climatological dataset was adopted. Trends were calculated by using the Theil–Sen (Theil, 1950; Sen, 1968) regression method implemented in the Openair software (Carslaw and Ropkins, 2012), after having deseasonalized the time series. No significant trends in the SI frequency were discernible for NCO-P, which showed only a weak increase of $0.03\% \text{ yr}^{-1}$. In addition to this estimation, the trend analysis based on seasonal SI frequencies was performed. The only significant ($p < 0.1$) positive trend was found for winter ($+0.18\% \text{ yr}^{-1}$). The lack of an overall trend in SI events was in line with previous findings, such as Sprenger and Wernli (2003) and Škerlak et al. (2014).

The long-term variability in SI frequency at NCO-P was further analyzed with respect to potential oscillations and periodicities. To this aim, the complete ensemble empirical mode decomposition with adaptive noise method (CEEM-DAN; Torres et al., 2011) was applied. This technique is an improved version of the original empirical mode decomposition method (Huang et al., 1998) based on the Hilbert–Huang transform and practical for nonlinear and non-stationary time series. It aims at subtracting several components (i.e., the so-called intrinsic mode functions, IMFs) from the original signal, each of which explains a different cyclic variation, and a residual, which represents the overall trend in the original time series. The method has been recently used in atmospheric and climatic studies (e.g., Coughlin and Tung, 2004; Xu et al., 2016a), but none of these regarded trends in SI yet. The time series could be decomposed into seven IMFs, with very different timescales (Fig. 4.6). To focus on long-term variations, high-frequency oscillations with characteristic periods shorter than 1 year were neglected. Apart from an evident seasonal cycle (Fig. 4.6b), the time series presents an IMF with a clear period of 28 months (IMF 5, Fig. 4.6c) that is weakly anti-correlated ($r = -0.3$) to the Quasi-Biennial Oscillation (QBO); the anti-correlation is maximized during post-monsoon and winter seasons ($r = -0.5$ and $r = -0.4$, respectively). In this chapter, the QBO index (blue line in Fig. 4.6c), archived by the Free University of Berlin (<http://www.geo.fu-berlin.de/met/ag/strat/produkte/qbo/qbo.dat>), was adopted for comparison. It refers to the monthly equatorial zonal wind at 50 hPa. Signals relating STE and QBO were found by Hsu and Prather (2009), who indicated that 20% of the inter-annual STE variance in the Northern Hemisphere can be explained by the QBO. More generally, the mechanisms for which QBO affects the STE variability are both the direct modulation of the circulation through thermal wind balance and the impact on the strength of the overturning circulation by altering the propagation and dissipation of planetary-scale waves (Tung and Yang, 1994; Kinnersley and Tung, 1999; Neu et al., 2014). IMF 6 (Fig. 4.6d) exhibits two peaks in the

power spectrum, corresponding to periods of 3.5 and 5.8 years (not shown), potentially indicating an influence from the El-Niño–Southern Oscillation (ENSO). In fact, ENSO has been found to have an impact on the STE variability via the induced anomalous strong convective activity in the tropics (James et al., 2003). Moreover, a strong correlation between STE and ENSO was found by Zeng and Pyle (2005) and Voulgarakis et al. (2011), with the total modeled STE maximized during El Niño and minimized during La Niña years. The link is probably caused by modulations of the subtropical jet. Here, IMF 6 presents some periods of inverse variability with respect to the multivariate ENSO index (MEI; Wolter and Timlin, 1993), included as the red line in Fig. 4.6d. Similar relations were also reported in Neu et al. (2014), with the STE flux increased during El Niño/easterly-shear QBO, because of the strengthening of the stratospheric overturning circulation and the intensified transport of air from the ozone maximum poleward and downward to midlatitudes. Conversely, La Niña/westerly QBO phases are associated with a weakening of the circulation and hence reduced STE flux. The last IMF (IMF 7, Fig. 4.6e) shows a period of nearly 10 years, possibly related to the solar cycle. The time series of the 13-month smoothed monthly total sunspot number (orange line in Fig. 4.6e, retrieved by the Royal Observatory of Belgium, <http://www.sidc.be/silso/datafiles>) is positively correlated with IMF 7 ($r = 0.7$). Signals of influence of the sunspot cycle in the upper troposphere–lower stratosphere have been indicated in several works (e.g., Labitzke and Van Loon, 1997b,a; Coughlin and Tung, 2004), suggesting that the association between the Sun and stratospheric parameters (e.g., O_3) is due to solar-induced changes in the atmospheric circulation.

4.4.3 SI influence on O_3 and BC concentrations at NCO-P

Since STEFLUX represents an efficient methodology for simulating the transport conditions (as presented in Sect. 4.4.1), it can be used to evaluate the SI influence on O_3 and BC concentrations at NCO-P. The ERA-Interim O_3 value was not used in this estimate, because it is known to present several uncertainties, on the order of 10%; moreover, this O_3 field was shown to have better agreement with independent observations in the stratosphere than in the troposphere (Dragani, 2011).

Figure 4.7 shows the seasonal box-and-whisker plot for O_3 (4.7a) and BC (4.7b) for days affected or not by SI. SI days are selected by following the approach presented in Sect. 4.4.1; to neglect the possible influence of acute pollution events due to valley transport (which typically occur on 9% of the measurements, see Marinoni et al., 2013; Putero et al., 2014), the SI averages were computed only considering the hours which presented BC values less than 100 ng m^{-3} . On the other hand, the no-SI averages are computed by considering days not selected

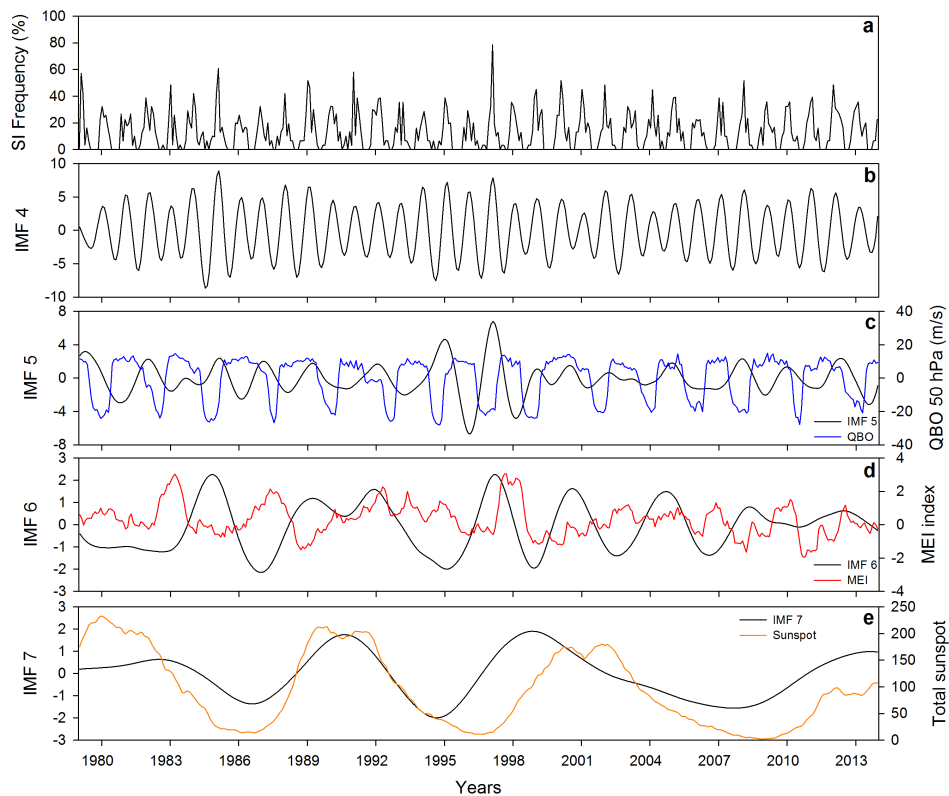


Figure 4.6: Time series of monthly averaged SI frequency, as retrieved by STEFLUX, at NCO-P (a), and some of its IMFs (i.e., IMF 4–7, b–e, respectively) resulting from the application of the CEEMDAN analysis. The blue line in (c) represents the equatorial zonal wind at 50 hPa, used as a measure of the QBO signal, the red line in (d) depicts the multivariate ENSO index (MEI), and the orange line in (e) indicates the 13-month smoothed monthly total sunspot number.

by STEFLUX. For O_3 , statistically significant increases (calculated by a Mann-Whitney “U test”; Mann and Whitney, 1947) during SI days were found in every season. Considering the entire dataset, an increase of 14 % was observed, with the maximum during the monsoon (+36 %). The overall increase observed is a bit underestimated, as compared to previous works (Cristofanelli et al., 2010; Bracci et al., 2012). Conversely, except for the monsoon season, BC always presented statistically significant decreases: –58 % considering the entire dataset. This value is in line with previous works (Marinoni et al., 2010; Bracci et al., 2012). The only increase in BC concentrations during SI days, with respect to the rest of the period, was found during the monsoon, although this value was not statistically significant. This is possibly related to a rather common phenomenon

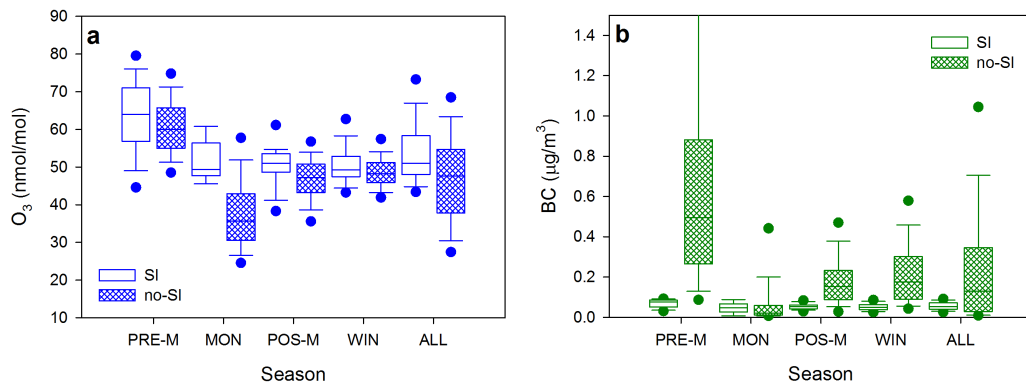


Figure 4.7: Seasonal box-and-whisker plot for O₃ (a) and BC (b), for days affected or not by SI (as identified by STEFLUX, see Sect. 4.4.1). SI averages are computed considering the hours which presented BC values less than 100 ng m⁻³.

occurring in the Himalayas, i.e., an increase in BC and O₃ concentrations during the summer monsoon onset. As thoroughly presented in Cristofanelli et al. (2014), this phenomenon is due to a change in the atmospheric circulation at NCO-P, from the typical monsoon conditions to westerly circulation, which favors: (i) a short period of very low (or nearly absent) rain precipitation in the central Himalayas, consequently weakening the wet scavenging removal process, and (ii) the arrival of air-masses crossing the central Pakistan, northwestern Indo-Gangetic Plain, and the Himalayan foothills (characterized by increased anthropogenic emissions).

4.5 Conclusions

This chapter presented a novel methodology (STEFLUX) to evaluate SI events in a user-defined region by using as input a Lagrangian STE climatology derived from the ERA-Interim reanalysis. Besides having shown an illustrative case study (Sect. 4.3.2) as a typical STEFLUX application, the STEFLUX skills in detecting SI were investigated, by comparing its time series with corresponding long-term SI time series derived from the observational dataset (SIO; see Sect. 4.2).

Our results showed that STEFLUX correctly represented the typical seasonal cycles of SI frequencies over this area, with the highest occurrence of SI in winter. The lowest SI occurrence was recorded during the monsoon season. STEFLUX had real skill in detecting single events at both regions, especially for robust (i.e., longer than 1 day) events. The identification of short events was more problematic; this is in agreement with a similar study by Cui et al. (2009),

who reported considerable difficulties for two Lagrangian models in capturing “inconspicuous” SI events. This issue is also reflected by a low agreement in the evaluation of the interannual variability in SI frequency (especially during winter). Hence, STEFLUX premium application is in determining the SI input at a larger, regional scale. Moreover, although not investigated hereby, STEFLUX might be deployed as a particularly relevant tool to investigate how SI long-term variability influences the atmospheric composition at these specific locations (e.g., by deploying the O_3 values that are available along each trajectory).

The observed mismatch between STEFLUX and SIO occurs for several reasons, such as the absence of representation of subgrid-scale processes in STEFLUX (e.g., convection, turbulent diffusion and mixing), along the path from the stratosphere to the target region. Furthermore, one should consider that these subgrid-scale processes can also lead to “local” or transient SI events captured by a single measurement point, which cannot be considered representative/significant for a whole region. In addition to this, another reason for the mismatch might be mixing and dilution processes occurring within air-masses from the tropopause crossing to the target region, expected to be maximized for greater travel times. Lastly, as also demonstrated in previous studies, the “overpasses” phenomenon might have a not negligible impact.

Another important feature of STEFLUX is its capability of climatologically assessing the SI occurrence at the chosen site, since the ERA-Interim reanalysis extends back to 1979. In this study, it allowed us to obtain a 35-year time series of SI events, which affected 13 % of the period. The tropopause crossings during the whole 35-year period, provided by STEFLUX, were further analyzed. NCO-P showed two main cluster regions, i.e., central Asia (maximized for events with short travel times between the tropopause and the target box, Δt) and northern Africa (which had its maximum for events with $48 \text{ h} \leq \Delta t < 72 \text{ h}$). Trends on this long time series were then evaluated: no trends in the SI occurrence were discernible, and the only statistically significant trend was observed for winter seasons ($+0.18 \% \text{ yr}^{-1}$). Furthermore, for the first time the CEEMDAN analysis has been performed on the SI time series characterizing this “hot spot” area in order to evaluate periodicities and their possible relation to climate factors. Signs of influence from the Quasi-Biennial Oscillation (QBO), the El-Niño–Southern Oscillation (ENSO) and the solar cycle were found. These results indicate the possible impact of anthropogenic climate change on SI occurrence via changes in the ENSO and QBO regimes.

Last but not least, STEFLUX can be a powerful tool for evaluating the SI influence on O_3 and BC concentrations at NCO-P. In days potentially affected by SI, after ruling out the effect of the acute pollution events due to valley transport, a statistically significant increase in O_3 concentrations ($+14 \%$, on average), and a

statistically significant decrease for BC (-58% , on average), was observed. This analysis further indicates the non-negligible role that such a natural process (i.e., SI) has in modulating the O_3 and BC concentrations at NCO-P.

Conclusions

As largely pointed out throughout the work, south Asia and the Himalayas are considered among the worldwide “hot spots” for the climate impacts of air pollution. The area is characterized by large amounts of short-lived climate forcers/pollutants (SLCF/P, among which BC and O₃), i.e., atmospheric substances with relatively short lifetimes, with harmful effects for climate, ecosystems and human health, produced from both anthropogenic and natural sources. The aim of this thesis was indeed to characterize several processes influencing BC and O₃ variability in the broad southern Himalayan region.

The Kathmandu Valley in the Himalayan foothills is certainly a crucial area for what concerns the anthropogenic activities. The persistent poor air quality conditions of the valley are dangerous for the environment and for the health of nearly 3 million people that inhabit the area. In Chapter 2, the BC and O₃ variability at Paknajol, an urban site in the Kathmandu Valley, was investigated. Very high BC and O₃ values characterized the entire period under study (February 2013–January 2014), with maxima in winter and pre-monsoon, and minima during the summer monsoon. BC levels were mostly related to road traffic, domestic emissions, use of numerous gensets, operations of brick kilns and refuse burning. Concerning the elevated O₃ levels, the application of a recurrent neural network model indicated that photochemistry contributes for 6–34 %, and that planetary boundary layer (PBL) dynamics and entrainment of free tropospheric air play a significant role in determining O₃ variability at Paknajol. Moreover, especially during the pre-monsoon, widespread biomass burning emissions can contribute to enhance the O₃ levels in the valley. During the study period, air quality in Kathmandu was so poor that 51.4 % of the available PM₁₀ data exceeded the 24 h limit of 120 µg m⁻³, while 37.5 % of the O₃ dataset exceeded the

air quality guidelines ($100 \mu\text{g m}^{-3}$) imposed by the World Health Organization. All of the information comprised in Chapter 2 make it necessary to study and implement efficient mitigation measures for the high pollution levels that affect the Kathmandu Valley, and potentially, the wider area that lies at the Himalayan foothills, likely posing a threat to the whole southern Himalayan environment.

The possible influence of the high pollution levels from the Kathmandu Valley to the wider Himalayan region was studied in Chapter 3. Here, the specific role played by air-mass transport from the PBL over the Himalayan foothills in affecting BC and O_3 variability in the southern Himalayas was investigated. Over the same time span as Chapter 2, the BC and O_3 variability at Paknajol and at the WMO/GAW global station Nepal Climate Observatory-Pyramid (NCO-P, 5079 m a.s.l., near the base camp of Mt. Everest) was compared. These two locations are characterized by very different conditions: in contrast to Paknajol, NCO-P is a remote site, representative of the background conditions of the high Himalayas and the free troposphere. A correlation study showed that BC and O_3 concentrations at NCO-P were linearly correlated with the daily PBL height over the Kathmandu urban area ($r^2 = 0.27$ for BC, and $r^2 = 0.25$ for O_3), suggesting that the latter can be an important parameter for linking the polluted air-masses between the two measurement sites. The linear correlation increased when considering an additional parameter in the analysis, i.e., back-trajectories: $r^2 = 0.50$ for BC, and $r^2 = 0.65$ for O_3 , in days characterized by the arrival of air-masses at NCO-P, which have crossed the PBL over the Kathmandu urban area. Thus, in this subset of days (representing 9% of the period under study), 50% and 65% of the BC and O_3 variability at NCO-P could be explained by the PBL variations over the Kathmandu megacity. Moreover, the highest BC and O_3 levels at NCO-P also corresponded to the highest BC and O_3 concentrations recorded at Paknajol, further indicating a clear evidence for these transport phenomena in affecting BC and O_3 variability at NCO-P. Improving all of the limitations of the study (e.g., the use of back-trajectories in mountainous environments, the coarse resolution of satellite/modeled datasets, the lack of continuous PBL height, CO and NO_2 in situ observations) would certainly provide a more accurate assessment of the impact of such transport processes for the high levels of pollution from a regional "hot spot" to remote Himalayan regions.

Along with transport and anthropogenic emissions, a significant natural contribution in modulating O_3 and BC variability at NCO-P is given by stratospheric intrusions (SI). This contribution was assessed in Chapter 4, where a novel tool called STEFLUX (Stratosphere-to-Troposphere Exchange Flux) was presented and applied to NCO-P. This relatively fast-computing tool is based on the stratosphere-to-troposphere (STE) climatology, which uses the trajectories from the ERA-Interim reanalysis dataset. STEFLUX is a powerful tool in rep-

representing the typical seasonal cycles of SI frequencies (which affected 13 % of the period 2006–2013) over NCO-P area, with maxima SI events in winter and minima during the monsoon. Another remarkable feature of STEFLUX is its capability of climatologically assessing the SI occurrence, since the ERA-Interim reanalysis extends back to 1979. At NCO-P, the percentage of days affected by SI (i.e., 13 %) was maintained also over the 35-year period (1979–2013). The main tropopause crossing regions associated to these events were located over northern Africa (maximized for “medium” events, i.e., between 2 and 3 days from the tropopause crossing to the arrival at NCO-P), and central Asia (maximized for “short” SI events, i.e., between 1 and 2 days). Lastly, the trend analysis was performed over this long time series, without observing any significant trend, except for winter seasons ($+0.18\% \text{ yr}^{-1}$). Last but not least, STEFLUX was used for evaluating the impact of SI on O_3 and BC concentrations at the measurement site, over 2006–2013. In days potentially affected by SI (13 % of the period), ruling out the acute pollution events due to valley transport (i.e., hours with a BC value greater than $100 \mu\text{g m}^{-3}$), which typically occur on 9 % of the measurements (Putero et al., 2014), a statistically significant increase in O_3 concentrations ($+14\%$, on average, over 2006–2013), and a statistically significant decrease for BC (-58%), was observed. This behavior was consistent throughout all the seasons, except for BC during the monsoon (although not statistically significant).

As also emerged from this thesis, quantifying the exact contributions from the different processes affecting BC and O_3 variability remains a challenging task, especially because there are no specific “fingerprints” able to assess the contributions separately. Despite this, and taking into account all of the limitations of this study (e.g., the relatively “short” time periods considered, the use of coarse resolution modeling tools in mountainous environments), the results presented in this thesis point out the necessity of implementing correct mitigation measures for limiting the occurrence of acute pollution events in the southern Himalayas, which have possible implications not only on a regional scale, but also for the global climate.



Supplementary material

A.1 Supplementary material for Chapter 2

Table A.1: Correlation coefficients (r) between several parameters (BC, O₃, accumulation and coarse particles, WS, T, and RAD) for hourly and daily (in parentheses) values, over the whole sampling period, computed during convective hours only (i.e., between 11:00 and 17:00).

	O ₃	BC	Acc.	Coarse	WS	T	RAD
O ₃	-	-0.20(0.17)	0.62 (0.61)	0.51 (0.52)	0.16 (0.49)	0.18 (0.16)	0.50 (0.53)
BC	0.20 (0.17)	-	0.82 (0.81)	0.79 (0.71)	-0.35 (-0.24)	-0.44 (-0.58)	-0.10 (-0.36)
Acc.	0.62 (0.61)	0.82 (0.81)	-	0.79 (0.79)	-0.03 (0.15)	-0.13 (-0.13)	0.03 (-0.01)
Coarse	0.51 (0.52)	0.79 (0.71)	0.79 (0.79)	-	-0.06 (0.21)	-0.03 (0.03)	0.03 (0.04)
WS	0.16 (0.49)	-0.35 (-0.24)	-0.03 (0.15)	-0.06 (0.21)	-	0.28 (0.37)	0.11 (0.72)
T	0.18 (0.16)	-0.44 (-0.58)	-0.13 (-0.13)	-0.03 (-0.03)	0.28 (0.37)	-	0.34 (0.50)
RAD	0.50 (0.53)	-0.10 (-0.36)	0.03 (-0.01)	0.03 (0.04)	0.11 (0.72)	0.34 (0.50)	-

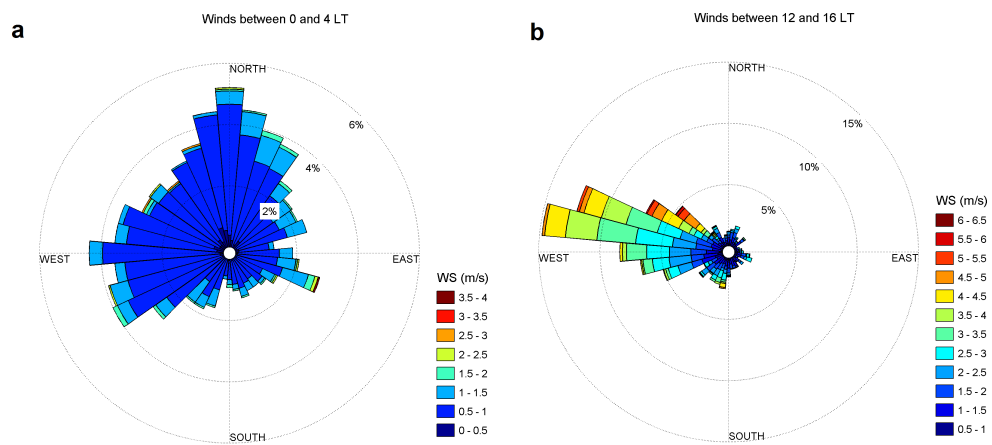


Figure A.1: Wind direction and intensities for Paknajol. Panel (a) shows winds between 0:00 and 4:00, while panel (b) encloses winds between 12:00 and 16:00.

A.2 Supplementary material for Chapter 4

A.2.1 Technical details on the methodology for the identification of SI events based on observations (SIO)

In this section, technical details on the SI selection methodology presented in Sect. 4.2 (i.e., “stratospheric intrusion observations”, SIO) are given. This methodology refers to that used in Cristofanelli et al. (2010).

In situ datasets

O₃ and meteorological parameters have been continuously monitored at NCO-P since 2006. Surface O₃ measurements were performed by using a UV-photometric analyser (Thermo Scientific–TEI 49i). All of the other parameters were sampled at 1-min time resolution and aggregated to a common time base of 1 h. All observations in Chapter 4 are expressed in standard temperature and pressure (0 °C and 1013 hPa) and refer to UTC, for avoiding biases when comparing the analyses to the STEFLUX outputs.

Total column O₃ retrievals

The daily total column of O₃ (TCO) generated by the NASA Ozone Monitoring Instrument (OMI, Levelt et al., 2006) science team was used. Data referred to the Version-003 of Level-3 Aura/OMI daily global TOMS-Like TCO gridded product (OMTO3e, Bhartia, 2012), calculated on a 1° × 1° pixel encompassing the measurement site location.

Potential vorticity values

Potential vorticity (PV) values were retrieved by the analysis of back-trajectories reaching both stations. LAGRANTO (Wernli and Davies, 1997; Sprenger and Wernli, 2015) was used as the Lagrangian model to calculate the path of air-masses reaching NCO-P. Its calculations are based on the 6-hourly meteorological 3-D grid composing the operational analysis composed by the ECMWF. A set of 5-day back-trajectories were computed (at 00:00, 06:00, 12:00 and 18:00 UTC); among these, only those starting at 490 hPa were retained, to minimize possible effects between the model and the real topography.

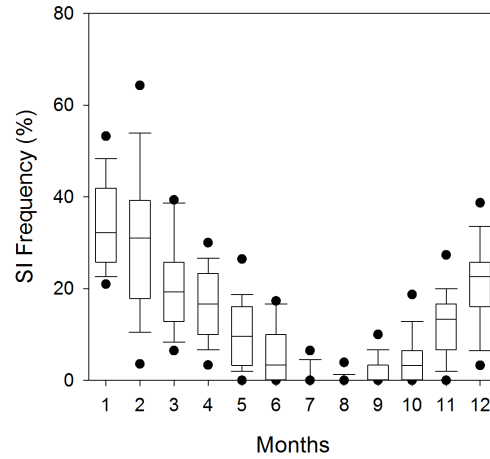


Figure A.2: Box-whiskers plot of the annual variation of SI frequency, computed by STEFLUX over the period 1979–2013.

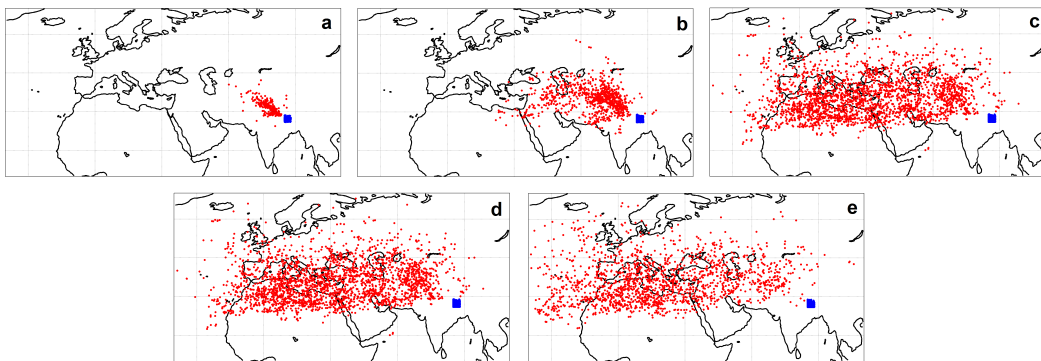


Figure A.3: Tropopause crossing (red dots) and first box crossing (blue dots) locations for the SI events at NCO-P over the period 1979–2013. The different panels indicate the Δt categories: $0 \text{ h} \leq \Delta t < 24 \text{ h}$ (a), $24 \text{ h} \leq \Delta t < 48 \text{ h}$ (b), $48 \text{ h} \leq \Delta t < 72 \text{ h}$ (c), $72 \text{ h} \leq \Delta t < 96 \text{ h}$ (d) and $96 \text{ h} \leq \Delta t < 120 \text{ h}$ (e).

Bibliography

- Agrawal, M., Auffhammer, M., Chopra, U., Emberson, L., Iyengararasan, M., Kalra, N., Ramana, M., Ramanathan, V., Singh, A., and Vincent, J.: Impacts of atmospheric brown clouds on agriculture, in: *Part II of Atmospheric Brown Clouds: Regional Assessment Report with Focus on Asia, Project Atmospheric Brown Cloud, UNEP, Nairobi, Kenya, 2008.*
- Alastuey, A., Querol, X., Castillo, S., Escudero, M., Avila, A., Cuevas, E., Torres, C., Romero, P.-M., Exposito, F., García, O., Diaz, J. P., Dingenen, R. V., and Putaud, J. P.: Characterisation of TSP and PM_{2.5} at Izaña and Sta. Cruz de Tenerife (Canary Islands, Spain) during a Saharan Dust Episode (July 2002), *Atmos. Environ.*, 39, 4715 – 4728, 2005.
- Anenberg, S. C., Talgo, K., Arunachalam, S., Dolwick, P., Jang, C., and West, J. J.: Impacts of global, regional, and sectoral black carbon emission reductions on surface air quality and human mortality, *Atmos. Chem. Phys.*, 11, 7253–7267, 2011.
- Anenberg, S. C., Schwartz, J., Shindell, D., Amann, M., Faluvegi, G., Klimont, Z., Janssens-Maenhout, G., Pozzoli, L., Van Dingenen, R., Vignati, E., Emberson, L., Muller, N. Z., West, J. J., Williams, M., Demkine, V., Hicks, W. K., Kuylestierna, J., Reas, F., and Ramanathan, V.: Global air quality and health co-benefits of mitigating near-term climate change through methane and black carbon emission controls, *Environ. Health Persp.*, 120, 831–839, 2012.
- Appenzeller, C. and Davies, H. C.: Structure of stratospheric intrusions into the troposphere, *Nature*, 358, 570–572, 1992.
- Appenzeller, C., Davies, H., and Norton, W.: Fragmentation of stratospheric intrusions, *J. Geophys. Res.*, 101, 1435–1456, 1996.

- Aryal, R. K., Lee, B.-K., Karki, R., Gurung, A., Kandasamy, J., Pathak, B. K., Sharma, S., and Giri, N.: Seasonal PM₁₀ dynamics in Kathmandu Valley, *Atmos. Environ.*, **42**, 8623–8633, 2008.
- Balestrini, R., Delconte, C. A., Sacchi, E., Wilson, A. M., Williams, M. W., Cristofanelli, P., and Putero, D.: Wet deposition at the base of Mt Everest: Seasonal evolution of the chemistry and isotopic composition, *Atmos. Environ.*, **146**, 100–112, 2016.
- Bell, M. L., McDermott, A., Zeger, S. L., Samet, J. M., and Dominici, F.: Ozone and short-term mortality in 95 US urban communities, 1987-2000, *JAMA-J. Am. Med. Assoc.*, **292**, 2372–2378, 2004.
- Bell, M. L., Peng, R. D., and Dominici, F.: The exposure-response curve for ozone and risk of mortality and the adequacy of current ozone regulations, *Environ. Health Persp.*, **114**, 532–536, 2006.
- Bhartia, P.: OMI/Aura TOMS-Like Ozone, Aerosol Index, Cloud Radiance Fraction Daily L3 Global 1.0× 1.0 deg, version 003, NASA Goddard Space Flight Center, 2012.
- Biancofiore, F., Verdecchia, M., Di Carlo, P., Tomassetti, B., Aruffo, E., Busilacchio, M., Bianco, S., Di Tommaso, S., and Colangeli, C.: Analysis of surface ozone using a recurrent neural network, *Sci. Total Environ.*, **514**, 379–387, 2015.
- Böhner, J.: General climatic controls and topoclimatic variations in Central and High Asia, *Boreas*, **35**, 279–295, 2006.
- Bolch, T., Kulkarni, A., Kääb, A., Huggel, C., Paul, F., Cogley, J., Frey, H., Kargel, J. S., Fujita, K., Scheel, M., Bajracharya, S., and Stoffel, M.: The state and fate of Himalayan glaciers, *Science*, **336**, 310–314, 2012.
- Bonasoni, P., Laj, P., Marinoni, A., Sprenger, M., Angelini, F., Arduini, J., Bonafè, U., Calzolari, F., Colombo, T., Decesari, S., Di Biagio, C., di Sarra, A. G., Evangelisti, F., Duchi, R., Facchini, M., Fuzzi, S., Gobbi, G. P., Maione, M., Panday, A., Roccato, F., Sellegri, K., Venzac, H., Verza, G., Villani, P., Vuillermoz, E., and Cristofanelli, P.: Atmospheric Brown Clouds in the Himalayas: first two years of continuous observations at the Nepal Climate Observatory-Pyramid (5079 m), *Atmos. Chem. Phys.*, **10**, 7515–7531, 2010.
- Bond, T. C., Doherty, S. J., Fahey, D. W., Forster, P. M., Berntsen, T., DeAngelo, B. J., Flanner, M. G., Ghan, S., Kärcher, B., Koch, D., Kinne, S., Kondo, Y., Quinn, P. K., Sarofim, M. C., Schultz, M. G., Schulz, M., Venkataraman, C., Zhang, H., Zhang, S., Bellouin, N., Guttikunda, S. K., Hopke, P. K., Jacobson, M. Z., Kaiser, J. W., Klimont, Z., Lohmann, U., Schwarz, J. P., Shindell, D., Storelvmo, T., Warren, S. G., and Zender, C. S.: Bounding the role of black carbon in the climate system: a scientific assessment, *J. Geophys. Res.*, **118**, 5380–5552, 2013.

- Borm, P. J., Schins, R. P., and Albrecht, C.: Inhaled particles and lung cancer, part B: paradigms and risk assessment, *Int. J. Cancer*, 110, 3–14, 2004.
- Bourqui, M.: Stratosphere-troposphere exchange from the Lagrangian perspective: a case study and method sensitivities, *Atmos. Chem. Phys.*, 6, 2651–2670, 2006.
- Bourqui, M. and Trépanier, P.-Y.: Descent of deep stratospheric intrusions during the IONS August 2006 campaign, *J. Geophys. Res.*, 115, 2010.
- Bracci, A., Cristofanelli, P., Sprenger, M., Bonafè, U., Calzolari, F., Duchi, R., Laj, P., Marinoni, A., Roccatò, F., Vuillermoz, E., and Bonasoni, P.: Transport of stratospheric air masses to the Nepal Climate Observatory-Pyramid (Himalaya; 5079 m MSL): a synoptic-scale investigation, *J. Appl. Meteorol. Clim.*, 51, 1489–1507, 2012.
- Bucsela, E. J., Celarier, E. A., Wenig, M. O., Gleason, J. F., Veefkind, J. P., Boersma, K. F., and Brinksma, E. J.: Algorithm for NO₂ vertical column retrieval from the Ozone Monitoring Instrument, *IEEE Trans. Geosci. Remote Sens.*, 44, 1245–1258, 2006.
- Carslaw, D. C. and Ropkins, K.: Openair—an R package for air quality data analysis, *Environ. Modell. Soft.*, 27, 52–61, 2012.
- Chevalier, A., Gheusi, F., Delmas, R., Ordóñez, C., Sarrat, C., Zbinden, R., Thouret, V., Athier, G., and Cousin, J.-M.: Influence of altitude on ozone levels and variability in the lower troposphere: a ground-based study for western Europe over the period 2001–2004, *Atmos. Chem. Phys.*, 7, 4311–4326, 2007.
- Claiborn, C. S., Finn, D., Larson, T. V., and Koenig, J. Q.: Windblown dust contributes to high PM_{2.5} concentrations, *J. Air Waste Ma.*, 50, 1440–1445, 2000.
- Colbeck, I., Nasir, Z. A., Ahmad, S., and Ali, Z.: Exposure to PM₁₀, PM_{2.5}, PM₁ and carbon monoxide on roads in Lahore, Pakistan, *Aerosol Air Qual. Res.*, 11, 689–695, 2011.
- Cooper, O., Stohl, A., Hübler, G., Hsie, E., Parrish, D., Tuck, A., Kiladis, G., Oltmans, S., Johnson, B., Shapiro, M., Moody, J., and AS, L.: Direct transport of midlatitude stratospheric ozone into the lower troposphere and marine boundary layer of the tropical Pacific Ocean, *J. Geophys. Res.*, 110, 2005.
- Coughlin, K. and Tung, K.-K.: 11-year solar cycle in the stratosphere extracted by the empirical mode decomposition method, *Adv. Space Res.*, 34, 323–329, 2004.
- Cozic, J., Verheggen, B., Mertes, S., Connolly, P., Bower, K., Petzold, A., Baltensperger, U., and Weingartner, E.: Scavenging of black carbon in mixed phase clouds at the high alpine site Jungfraujoch, *Atmos. Chem. Phys.*, 7, 1797–1807, 2007.

- Cristofanelli, P., Bonasoni, P., Tositti, L., Bonafe, U., Calzolari, F., Evangelisti, F., Sandrini, S., and Stohl, A.: A 6-year analysis of stratospheric intrusions and their influence on ozone at Mt. Cimone (2165 m above sea level), *J. Geophys. Res.*, 111, 2006.
- Cristofanelli, P., Bracci, A., Sprenger, M., Marinoni, A., Bonafè, U., Calzolari, F., Duchi, R., Laj, P., Pichon, J. M., Roccatò, F., Venzac, H., Vuillermoz, E., and Bonasoni, P.: Tropospheric ozone variations at the Nepal Climate Observatory-Pyramid (Himalayas, 5079 m a.s.l.) and influence of deep stratospheric intrusion events, *Atmos. Chem. Phys.*, 10, 6537–6549, 2010.
- Cristofanelli, P., Putero, D., Adhikary, B., Landi, T., Marinoni, A., Duchi, R., Calzolari, F., Laj, P., Stocchi, P., Verza, G., Vuillermoz, E., Kang, S., Ming, J., and Bonasoni, P.: Transport of short-lived climate forcers/pollutants (SLCF/P) to the Himalayas during the South Asian summer monsoon onset, *Environ. Res. Lett.*, 9, 084005, 2014.
- Cui, J., Sprenger, M., Staehelin, J., Siegrist, A., Kunz, M., Henne, S., and Steinbacher, M.: Impact of stratospheric intrusions and intercontinental transport on ozone at Jungfraujoch in 2005: comparison and validation of two Lagrangian approaches, *Atmos. Chem. Phys.*, 9, 3371–3383, 2009.
- Dee, D. P., Uppala, S. M., Simmons, A. J., Berrisford, P., Poli, P., Kobayashi, S., Andrae, U., Balmaseda, M. A., Balsamo, G., Bauer, P., Bechtold, P., Beljaars, A. C. M., van de Berg, L., Bidlot, J., Bormann, N., Delsol, C., Dragani, R., Fuentes, M., Geer, A. J., Haimberger, L., Healy, S. B., Hersbach, H., Hólm, E. V., Isaksen, I., Kållberg, P., Köhler, M., Matricardi, M., McNally, A. P., Monge-Sanz, B. M., Morcrette, J.-J., Park, B.-K., Peubey, C., de Rosnay, P., Tavolato, C., Thépaut, J.-N., and Vitart, F.: The ERA-Interim reanalysis: configuration and performance of the data assimilation system, *Q. J. R. Meteorol. Soc.*, 137, 553–597, 2011.
- Deshmukh, D., Deb, M., and Verma, S.: Distribution patterns of coarse, fine and ultra-fine atmospheric aerosol particulate matters in major cities of Chhattisgarh, *Indian J. Environ. Prot.*, 30, 184–197, 2010.
- Deshmukh, D. K., Deb, M. K., and Mkoma, S. L.: Size distribution and seasonal variation of size-segregated particulate matter in the ambient air of Raipur city, India, *Air Qual. Atmos. Health*, 6, 259–276, 2013.
- Di Carlo, P., Pitari, G., Mancini, E., Gentile, S., Pichelli, E., and Visconti, G.: Evolution of surface ozone in central Italy based on observations and statistical model, *J. Geophys. Res.*, 112, 2007.
- Dragani, R.: On the quality of the ERA-Interim ozone reanalyses: Comparisons with satellite data, *Q. J. R. Meteorol. Soc.*, 137, 1312–1326, 2011.
- Draxler, R. R. and Hess, G.: An overview of the HYSPLIT_4 modelling system for trajectories, *Aust. Meteorol. Mag.*, 47, 295–308, 1998.

- Draxler, R. R., Stunder, B., Rolph, G., and Taylor, A.: HYSPLIT4 user's guide, NOAA Tech. Memo. ERL ARL, 230, 35, 1999.
- Duchi, R., Cristofanelli, P., Marinoni, A., Bourcier, L., Laj, P., Calzolari, F., Adhikary, B., Verza, G., Vuillermoz, E., and Bonasoni, P.: Synoptic-scale dust transport events in the southern Himalaya, *Aeolian Res.*, 13, 51–57, 2014.
- Dumka, U. C., Kaskaoutis, D. G., Srivastava, M. K., and Devara, P. C. S.: Scattering and absorption properties of near-surface aerosol over Gangetic–Himalayan region: the role of boundary-layer dynamics and long-range transport, *Atmos. Chem. Phys.*, 15, 1555–1572, 2015.
- Elman, J. L.: Finding structure in time, *Cognitive Sci.*, 14, 179–211, 1990.
- Engling, G. and Gelencsér, A.: Atmospheric brown clouds: From local air pollution to climate change, *Elements*, 6, 223–228, 2010.
- Faiz, A., Ale, B. B., and Nagarkoti, R. K.: The role of inspection and maintenance in controlling vehicular emissions in Kathmandu valley, Nepal, *Atmos. Environ.*, 40, 5967–5975, 2006.
- Flanner, M. G., Zender, C. S., Randerson, J. T., and Rasch, P. J.: Present-day climate forcing and response from black carbon in snow, *J. Geophys. Res.*, 112, 2007.
- Fowler, D., Amann, M., Anderson, R., Ashmore, M., Cox, P., Depledge, M., Derwent, D., Grennfelt, P., Hewitt, N., Hov, O., Jenkin, M., Kelly, F., Liss, P., Pilling, M., Pyle, J., Slingo, J., and Stevenson, D.: *Ground-level ozone in the 21st century: future trends, impacts and policy implications*, vol. 15/08 of Royal Society Policy Document 15/08, The Royal Society, RS1276 edn., 2008.
- Friedl, M. A., Sulla-Menashe, D., Tan, B., Schneider, A., Ramankutty, N., Sibley, A., and Huang, X.: MODIS Collection 5 global land cover: Algorithm refinements and characterization of new datasets, *Rem. Sens. Environ.*, 114, 168–182, 2010.
- Furger, M., Dommen, J., Graber, W. K., Poggio, L., Prévôt, A. S., Emeis, S., Grell, G., Trickl, T., Gomiscek, B., Neininger, B., and Wotawa, G.: The VOTALP Mesolcina Valley Campaign 1996–concept, background and some highlights, *Atmos. Environ.*, 34, 1395–1412, 2000.
- Gauss, M., Myhre, G., Pitari, G., Prather, M., Isaksen, I., Berntsen, T., Brasseur, G. P., Dentener, F., Derwent, R., Hauglustaine, D., Horowitz, L. W., Jacob, D. J., Johnson, M., Law, K. S., Mickley, L. J., Müller, J.-F., Plantevin, P.-H., Pyle, J. A., Rogers, H. L., Stevenson, D. S., Sundet, J. K., van Weele, M., and Wild, O.: Radiative forcing in the 21st century due to ozone changes in the troposphere and the lower stratosphere, *J. Geophys. Res.*, 108, 2003.

- Ghude, S. D., van der A, R., Beig, G., Fadnavis, S., and Polade, S.: Satellite derived trends in NO₂ over the major global hotspot regions during the past decade and their inter-comparison, *Environ. Pollut.*, 157, 1873–1878, 2009.
- Gilge, S., Plass-Dülmer, C., Fricke, W., Kaiser, A., Ries, L., Buchmann, B., and Steinbacher, M.: Ozone, carbon monoxide and nitrogen oxides time series at four alpine GAW mountain stations in central Europe, *Atmos. Chem. Phys.*, 10, 12 295–12 316, 2010.
- Giri, D., Murthy, V. K., Adhikary, P. R., and Khanal, S. N.: Ambient air quality of Kathmandu valley as reflected by atmospheric particulate matter concentrations (PM10), *Int. J. Environ. Sci. Te.*, 3, 403–410, 2006.
- Gustafsson, Ö. and Ramanathan, V.: Convergence on climate warming by black carbon aerosols, *Proc. Natl. Acad. Sci. USA*, 113, 4243–4245, 2016.
- Gustafsson, Ö., Kruså, M., Zencak, Z., Sheesley, R. J., Granat, L., Engström, E., Praveen, P., Rao, P., Leck, C., and Rodhe, H.: Brown clouds over South Asia: biomass or fossil fuel combustion?, *Science*, 323, 495–498, 2009.
- Hansen, J. and Nazarenko, L.: Soot climate forcing via snow and ice albedos, *Proc. Natl. Acad. Sci. USA*, 101, 423–428, 2004.
- Highwood, E. J. and Kinnersley, R. P.: When smoke gets in our eyes: the multiple impacts of atmospheric black carbon on climate, air quality and health, *Environ. Int.*, 32, 560–566, 2006.
- HMG/MOPE: *Draft report on air emission inventory*, Kathmandu, Nepal, 2003.
- Holton, J. R., Haynes, P. H., McIntyre, M. E., Douglass, A. R., Rood, R. B., and Pfister, L.: Stratosphere-troposphere exchange, *Rev. Geophys.*, 33, 403–439, 1995.
- Hsu, J. and Prather, M. J.: Stratospheric variability and tropospheric ozone, *J. Geophys. Res.*, 114, 2009.
- Huang, N. E., Shen, Z., Long, S. R., Wu, M. C., Shih, H. H., Zheng, Q., Yen, N.-C., Tung, C. C., and Liu, H. H.: The empirical mode decomposition and the Hilbert spectrum for nonlinear and non-stationary time series analysis, in: *Proceedings of the Royal Society of London A: Mathematical, Physical and Engineering Sciences*, vol. 454, pp. 903–995, The Royal Society, 1998.
- Hyvärinen, A.-P., Raatikainen, T., Brus, D., Komppula, M., Panwar, T. S., Hooda, R. K., Sharma, V. P., and Lihavainen, H.: Effect of the summer monsoon on aerosols at two measurement stations in Northern India – Part 1: PM and BC concentrations, *Atmos. Chem. Phys.*, 11, 8271–8282, 2011.

- Hyvärinen, A.-P., Vakkari, V., Laakso, L., Hooda, R. K., Sharma, V. P., Panwar, T. S., Beukes, J. P., van Zyl, P. G., Josipovic, M., Garland, R. M., Andreae, M. O., Pöschl, U., and Petzold, A.: Correction for a measurement artifact of the Multi-Angle Absorption Photometer (MAAP) at high black carbon mass concentration levels, *Atmos. Meas. Tech.*, 6, 81–90, 2013.
- IMD: *Monsoon report 2013*, edited by: Pai, D. S. and Bhan, S. C., India Meteorological Department, Pune, India, 2014.
- IPCC: *Climate Change 2013: The Physical Science Basis. Contribution of Working Group I to the Fifth Assessment Report of the Intergovernmental Panel on Climate Change*, Cambridge University Press, Cambridge, United Kingdom and New York, NY, USA, 2013.
- Jacobson, M. Z.: *Atmospheric pollution: history, science, and regulation*, Cambridge University Press, 2002.
- James, P., Stohl, A., Forster, C., Eckhardt, S., Seibert, P., and Frank, A.: A 15-year climatology of stratosphere–troposphere exchange with a Lagrangian particle dispersion model 2. Mean climate and seasonal variability, *J. Geophys. Res.*, 108, 2003.
- Jansen, K. L., Larson, T. V., Koenig, J. Q., Mar, T. F., Fields, C., Stewart, J., and Lippmann, M.: Associations between health effects and particulate matter and black carbon in subjects with respiratory disease, *Environ. Health Persp.*, 113, 1741–1746, 2005.
- Janssen, N. A., Gerlofs-Nijland, M. E., Lanki, T., Salonen, R. O., Cassee, F., Hoek, G., Fischer, P., Brunekreef, B., and Krzyzanowski, M.: *Health effects of black carbon*, WHO Regional Office for Europe, Copenhagen, Denmark, 2012.
- Justice, C., Giglio, L., Korontzi, S., Owens, J., Morisette, J., Roy, D., Descloitres, J., Alleaume, S., Petitcolin, F., and Kaufman, Y.: The MODIS fire products, *Rem. Sens. Environ.*, 83, 244–262, 2002.
- Kinnersley, J. S. and Tung, K. K.: Mechanisms for the extratropical QBO in circulation and ozone, *J. Atmos. Sci.*, 56, 1942–1962, 1999.
- Klausen, J., Zellweger, C., Buchmann, B., and Hofer, P.: Uncertainty and bias of surface ozone measurements at selected Global Atmosphere Watch sites, *J. Geophys. Res.*, 108, 2003.
- Kleinman, L., Lee, Y.-N., Springston, S. R., Nunnermacker, L., Zhou, X., Brown, R., Hallock, K., Klotz, P., Leahy, D., Lee, J. H., and Newman, L.: Ozone formation at a rural site in the southeastern United States, *J. Geophys. Res.*, 99, 3469–3482, 1994.
- Labitzke, K. and Van Loon, H.: Total ozone and the 11-yr sunspot cycle, *J. Atmos. Sol.-Terr. Phys.*, 59, 9–19, 1997a.

- Labitzke, K. and Van Loon, H.: The signal of the 11-year sunspot cycle in the upper troposphere-lower stratosphere, *Space Sci. Rev.*, 80, 393–410, 1997b.
- Lamarque, J.-F. and Hess, P. G.: Cross-tropopause mass exchange and potential vorticity budget in a simulated tropopause folding, *J. Atmos. Sci.*, 51, 2246–2269, 1994.
- Lelieveld, J., Evans, J., Fnais, M., Giannadaki, D., and Pozzer, A.: The contribution of outdoor air pollution sources to premature mortality on a global scale, *Nature*, 525, 367–371, 2015.
- Levelt, P. F., van den Oord, G. H., Dobber, M. R., Malkki, A., Visser, H., de Vries, J., Stammes, P., Lundell, J. O., and Saari, H.: The Ozone Monitoring Instrument, *IEEE Trans. Geosci. Remote Sens.*, 44, 1093–1101, 2006.
- Levy, J. I., Chemerynski, S. M., and Sarnat, J. A.: Ozone exposure and mortality: an empiric bayes metaregression analysis, *Epidemiology*, 16, 458–468, 2005.
- Lin, M., Fiore, A. M., Cooper, O. R., Horowitz, L. W., Langford, A. O., Levy, H., Johnson, B. J., Naik, V., Oltmans, S. J., and Senff, C. J.: Springtime high surface ozone events over the western United States: quantifying the role of stratospheric intrusions, *J. Geophys. Res.*, 117, 2012.
- Lönblad, L., Peterson, C., and Rögngvalsson, T.: Pattern recognition in high energy physics with artificial neural networks—JETNET 2.0, *Comput. Phys. Commun.*, 70, 167–182, 1992.
- Lu, Z., Zhang, Q., and Streets, D. G.: Sulfur dioxide and primary carbonaceous aerosol emissions in China and India, 1996–2010, *Atmos. Chem. Phys.*, 11, 9839–9864, 2011.
- Lundgren, D. A., Hlaing, D. N., Rich, T. A., and Marple, V. A.: PM10/PM2.5/PM1 data from a trichotomous sampler, *Aerosol Sci. Tech.*, 25, 353–357, 1996.
- Lüthi, Z. L., Škerlak, B., Kim, S.-W., Lauer, A., Mues, A., Rupakheti, M., and Kang, S.: Atmospheric brown clouds reach the Tibetan Plateau by crossing the Himalayas, *Atmos. Chem. Phys.*, 15, 6007–6021, 2015.
- Mann, H. and Whitney, D.: On a test of whether one of two random variables is stochastically larger than the other, *Ann. Math. Statist.*, 18, 50–60, 1947.
- Marinoni, A., Cristofanelli, P., Laj, P., Duchi, R., Calzolari, F., Decesari, S., Sellegri, K., Vuillermoz, E., Verza, G. P., Villani, P., and Bonasoni, P.: Aerosol mass and black carbon concentrations, a two year record at NCO-P (5079 m, Southern Himalayas), *Atmos. Chem. Phys.*, 10, 8551–8562, 2010.
- Marinoni, A., Cristofanelli, P., Laj, P., Duchi, R., Putero, D., Calzolari, F., Landi, T. C., Vuillermoz, E., Maione, M., and Bonasoni, P.: High black carbon and ozone concentrations during pollution transport in the Himalayas: five years of continuous observations at NCO-P global GAW station, *J. Environ. Sci.*, 25, 1618–1625, 2013.

- Mauzerall, D. L. and Wang, X.: Protecting agricultural crops from the effects of tropospheric ozone exposure: reconciling science and standard setting in the United States, Europe, and Asia, *Annu. Rev. Energy Environ.*, 26, 237–268, 2001.
- McMillan, W. W., Evans, K. D., Barnet, C. D., Maddy, E. S., Sachse, G. W., and Diskin, G. S.: Validating the AIRS Version 5 CO retrieval with DACOM in situ measurements during INTEX-A and-B, *IEEE Trans. Geosci. Remote Sens.*, 49, 2802–2813, 2011.
- Meloen, J., Siegmund, P., Van Velthoven, P., Kelder, H., Sprenger, M., Wernli, H., Kentarchos, A., Roelofs, G., Feichter, J., Land, C., Forster, C., James, P., Stohl, A., Collins, W., and Cristofanelli, P.: Stratosphere-troposphere exchange: A model and method intercomparison, *J. Geophys. Res.*, 108, 2003.
- Ménégoz, M., Krinner, G., Balkanski, Y., Boucher, O., Cozic, A., Lim, S., Ginot, P., Laj, P., Gallée, H., Wagon, P., Marinoni, A., and Jacobi, H. W.: Snow cover sensitivity to black carbon deposition in the Himalayas: from atmospheric and ice core measurements to regional climate simulations, *Atmos. Chem. Phys.*, 14, 4237–4249, 2014.
- Menon, S., Koch, D., Beig, G., Sahu, S., Fasullo, J., and Orlikowski, D.: Black carbon aerosols and the third polar ice cap, *Atmos. Chem. Phys.*, 10, 4559–4571, 2010.
- Monks, P. S., Archibald, A. T., Colette, A., Cooper, O., Coyle, M., Derwent, R., Fowler, D., Granier, C., Law, K. S., Mills, G. E., Stevenson, D. S., Tarasova, O., Thouret, V., von Schneidemesser, E., Sommariva, R., Wild, O., and Williams, M. L.: Tropospheric ozone and its precursors from the urban to the global scale from air quality to short-lived climate forcer, *Atmos. Chem. Phys.*, 15, 8889–8973, 2015.
- Naik, V., Voulgarakis, A., Fiore, A. M., Horowitz, L. W., Lamarque, J.-F., Lin, M., Prather, M. J., Young, P. J., Bergmann, D., Cameron-Smith, P. J., Cionni, I., Collins, W. J., Dalsøren, S. B., Doherty, R., Eyring, V., Faluvegi, G., Folberth, G. A., Josse, B., Lee, Y. H., MacKenzie, I. A., Nagashima, T., van Noije, T. P. C., Plummer, D. A., Righi, M., Rumbold, S. T., Skeie, R., Shindell, D. T., Stevenson, D. S., Strode, S., Sudo, K., Szopa, S., and Zeng, G.: Preindustrial to present-day changes in tropospheric hydroxyl radical and methane lifetime from the Atmospheric Chemistry and Climate Model Intercomparison Project (ACCMIP), *Atmos. Chem. Phys.*, 13, 5277–5298, 2013.
- Neu, J. L., Flury, T., Manney, G. L., Santee, M. L., Livesey, N. J., and Worden, J.: Tropospheric ozone variations governed by changes in stratospheric circulation, *Nat. Geosci.*, 7, 340–344, 2014.
- Ordóñez, C., Brunner, D., Staehelin, J., Hadjinicolaou, P., Pyle, J., Jonas, M., Wernli, H., and Prévôt, A.: Strong influence of lowermost stratospheric ozone on lower tropospheric background ozone changes over Europe, *Geophys. Res. Lett.*, 34, 2007.
- Panday, A. K. and Prinn, R. G.: Diurnal cycle of air pollution in the Kathmandu Valley, Nepal: Observations, *J. Geophys. Res.*, 114, 2009.

- Panday, A. K., Prinn, R. G., and Schär, C.: Diurnal cycle of air pollution in the Kathmandu Valley, Nepal: 2. Modeling results, *J. Geophys. Res.*, 114, 2009.
- Pope III, C. A., Ezzati, M., and Dockery, D. W.: Fine-particulate air pollution and life expectancy in the United States, *New Engl. J. Med.*, 360, 376–386, 2009.
- Pudasainee, D., Sapkota, B., Shrestha, M. L., Kaga, A., Kondo, A., and Inoue, Y.: Ground level ozone concentrations and its association with NO_x and meteorological parameters in Kathmandu valley, Nepal, *Atmos. Environ.*, 40, 8081–8087, 2006.
- Putero, D., Landi, T., Cristofanelli, P., Marinoni, A., Laj, P., Duchi, R., Calzolari, F., Verza, G., and Bonasoni, P.: Influence of open vegetation fires on black carbon and ozone variability in the southern Himalayas (NCO-P, 5079 m asl), *Environ. Pollut.*, 184, 597–604, 2014.
- Putero, D., Cristofanelli, P., Marinoni, A., Adhikary, B., Duchi, R., Shrestha, S. D., Verza, G. P., Landi, T. C., Calzolari, F., Busetto, M., Agrillo, G., Biancofiore, F., Di Carlo, P., Panday, A. K., Rupakheti, M., and Bonasoni, P.: Seasonal variation of ozone and black carbon observed at Paknajol, an urban site in the Kathmandu Valley, Nepal, *Atmos. Chem. Phys.*, 15, 13 957–13 971, 2015.
- Putero, D., Cristofanelli, P., Sprenger, M., Škerlak, B., Tositti, L., and Bonasoni, P.: STEFLUX, a tool for investigating stratospheric intrusions: application to two WMO/GAW global stations, *Atmos. Chem. Phys.*, 16, 14 203–14 217, 2016.
- Putero, D., Marinoni, A., Bonasoni, P., Calzolari, F., and Cristofanelli, P.: Comparison of black carbon and ozone variability at the Kathmandu “hot spot” and at the southern Himalayas, *Aerosol Air Qual. Res.*, in preparation, 2017.
- Raatikainen, T., Hyvärinen, A.-P., Hatakka, J., Panwar, T., Hooda, R., Sharma, V., and Lihavainen, H.: The effect of boundary layer dynamics on aerosol properties at the Indo-Gangetic plains and at the foothills of the Himalayas, *Atmos. Environ.*, 89, 548–555, 2014.
- Ramanathan, V. and Carmichael, G.: Global and regional climate changes due to black carbon, *Nat. Geosci.*, 1, 221–227, 2008.
- Ramanathan, V. and Crutzen, P.: New directions: atmospheric brown “clouds”, *Atmos. Environ.*, 37, 4033–4035, 2003.
- Ramanathan, V., Chung, C., Kim, D., Bettge, T., Buja, L., Kiehl, J., Washington, W., Fu, Q., Sikka, D., and Wild, M.: Atmospheric brown clouds: impacts on South Asian climate and hydrological cycle, *Proc. Natl. Acad. Sci. USA*, 102, 5326–5333, 2005.
- Ramanathan, V., Li, F., Ramana, M., Praveen, P., Kim, D., Corrigan, C., Nguyen, H., Stone, E. A., Schauer, J. J., Carmichael, G., Adhikary, B., and Yoon, S.: Atmospheric brown

- clouds: hemispherical and regional variations in long-range transport, absorption, and radiative forcing, *J. Geophys. Res.*, 112, 2007.
- Reed, R. J.: A study of a characteristic type of upper-level frontogenesis, *J. Meteorol.*, 12, 226–237, 1955.
- Roelofs, G.-J., Lelieveld, J., and van Dorland, R.: A three-dimensional chemistry/general circulation model simulation of anthropogenically derived ozone in the troposphere and its radiative climate forcing, *J. Geophys. Res.*, 102, 23 389–23 401, 1997.
- Romieu, I., Castro-Giner, F., Kunzli, N., and Sunyer, J.: Air pollution, oxidative stress and dietary supplementation: a review, *Eur. Respir. J.*, 31, 179–197, 2008.
- Rupakheti, D., Adhikary, B., Praveen, P. S., Rupakheti, M., Kang, S., Mahata, K. S., Naja, M., Zhang, Q., Panday, A. K., and Lawrence, M. G.: Pre-monsoon air quality over Lumbini, a world heritage site along the Himalayan foothills, *Atmos. Chem. Phys. Discuss.*, in review, 2016.
- Rupakheti, M., Panday, A. K., Lawrence, M. G., Kim, S., Sinha, V., Kang, S. C., Naja, M., Park, J. S., Hoor, P., Holben, B., Bonasoni, P., Sharma, R. K., Mues, A., Mahata, K., Bhardwaj, P., Sarkar, C., Rupakheti, D., Regmi, R. P., and Gustafsson, Ö.: Air pollution in the Himalayan foothills: overview of the SusKat-ABC international air pollution measurement campaign in Nepal, *Atmos. Chem. Phys. Discuss.*, in preparation, 2017.
- Schiemann, R., Lüthi, D., and Schär, C.: Seasonality and interannual variability of the westerly jet in the Tibetan Plateau region, *J. Clim.*, 22, 2940–2957, 2009.
- Schmale, J., Shindell, D., von Schneidmesser, E., Chabay, I., and Lawrence, M.: Air pollution: clean up our skies, *Nature*, 515, 335–337, 2014.
- Sebald, L., Treffeisen, R., Reimer, E., and Hies, T.: Spectral analysis of air pollutants. Part 2: ozone time series, *Atmos. Environ.*, 34, 3503–3509, 2000.
- Sen, P. K.: Estimates of the regression coefficient based on Kendall's tau, *J. Am. Stat. Assoc.*, 63, 1379–1389, 1968.
- Shahsavani, A., Naddafi, K., Haghhighifard, N. J., Mesdaghinia, A., Yunesian, M., Nabizadeh, R., Arahami, M., Sowlat, M., Yarahmadi, M., Saki, H., Alimohamadi, M., Nazmara, S., Motevalian, S., and Goudarzi, G.: The evaluation of PM₁₀, PM_{2.5}, and PM₁ concentrations during the Middle Eastern Dust (MED) events in Ahvaz, Iran, from April through September 2010, *J. Arid Environ.*, 77, 72–83, 2012.
- Sharma, C.: Urban air quality of Kathmandu Valley “Kingdom of Nepal”, *Atmos. Environ.*, 31, 2877–2883, 1997.
- Sharma, R., Bhattarai, B., Sapkota, B., Gewali, M., and Kjeldstad, B.: Black carbon aerosols variation in Kathmandu valley, Nepal, *Atmos. Environ.*, 63, 282–288, 2012.

- Shindell, D., Kuylenstierna, J. C. I., Vignati, E., van Dingenen, R., Amann, M., Klimont, Z., Anenberg, S. C., Muller, N., Janssens-Maenhout, G., Raes, F., Schwartz, J., Faluvegi, G., Pozzoli, L., Kupiainen, K., Höglund-Isaksson, L., Emberson, L., Streets, D., Ramanathan, V., Hicks, K., Oanh, N. T. K., Milly, G., Williams, M., Demkine, V., and Fowler, D.: Simultaneously mitigating near-term climate change and improving human health and food security, *Science*, 335, 183–189, 2012.
- Shrestha, P., Barros, A., and Khlystov, A.: Chemical composition and aerosol size distribution of the middle mountain range in the Nepal Himalayas during the 2009 pre-monsoon season, *Atmos. Chem. Phys.*, 10, 11 605–11 621, 2010.
- Shrestha, R. M. and Malla, S.: Air pollution from energy use in a developing country city: the case of Kathmandu Valley, Nepal, *Energy*, 21, 785–794, 1996.
- Shrestha, R. M. and Rajbhandari, S.: Energy and environmental implications of carbon emission reduction targets: case of Kathmandu Valley, Nepal, *Energ. Policy*, 38, 4818–4827, 2010.
- Shrestha, S. R., Oanh, N. T. K., Xu, Q., Rupakheti, M., and Lawrence, M. G.: Analysis of the vehicle fleet in the Kathmandu Valley for estimation of environment and climate co-benefits of technology intrusions, *Atmos. Environ.*, 81, 579–590, 2013.
- Sinha, B., Singh Sangwan, K., Maurya, Y., Kumar, V., Sarkar, C., Chandra, B. P., and Sinha, V.: Assessment of crop yield losses in Punjab and Haryana using 2 years of continuous in situ ozone measurements, *Atmos. Chem. Phys.*, 15, 9555–9576, 2015.
- Škerlak, B., Sprenger, M., and Wernli, H.: A global climatology of stratosphere–troposphere exchange using the ERA-Interim data set from 1979 to 2011, *Atmos. Chem. Phys.*, 14, 913–937, 2014.
- Sprenger, M. and Wernli, H.: A Northern Hemispheric climatology of cross-tropopause exchange for the ERA15 time period (1979–1993), *J. Geophys. Res.*, 108, 2003.
- Sprenger, M. and Wernli, H.: The LAGRANTO Lagrangian analysis tool – version 2.0, *Geosci. Model Dev.*, 8, 2569–2586, 2015.
- Sprenger, M., Wernli, H., and Bourqui, M.: Stratosphere-troposphere exchange and its relation to potential vorticity streamers and cutoffs near the extratropical tropopause, *J. Atmos. Sci.*, 64, 1587–1602, 2007.
- Stevenson, D., Dentener, F., Schultz, M., Ellingsen, K., Van Noije, T., Wild, O., Zeng, G., Amann, M., Atherton, C., Bell, N., Bergmann, D., Bey, I., Butler, T., Cofala, J., Collins, W. J., Derwent, R. G., Doherty, R. M., Drevet, J., Eskes, H. J., Fiore, A. M., Gauss, M., Hauglustaine, D. A., Horowitz, L. W., Isaksen, I. S. A., Krol, M. C., Lamarque, J.-F., Lawrence, M. G., Montanaro, V., Müller, J.-F., Pitari, G., Prather, M. J., Pyle, J. A., Rast, S., Rodriguez, J. M., Sanderson, M. G., Savage, N. H., Shindell, D. T., Strahan,

- S. E., Sudo, K., and Szopa, S.: Multimodel ensemble simulations of present-day and near-future tropospheric ozone, *J. Geophys. Res.*, 111, 2006.
- Stockwell, C. E., Christian, T. J., Goetz, J. D., Jayarathne, T., Bhave, P. V., Praveen, P. S., Adhikari, S., Maharjan, R., DeCarlo, P. F., Stone, E. A., Saikawa, E., Blake, D. R., Simpson, I. J., Yokelson, R. J., and Panday, A. K.: Nepal Ambient Monitoring and Source Testing Experiment (NAMaSTE): emissions of trace gases and light-absorbing carbon from wood and dung cooking fires, garbage and crop residue burning, brick kilns, and other sources, *Atmos. Chem. Phys.*, 16, 11 043–11 081, 2016.
- Stohl, A., Spichtinger-Rakowsky, N., Bonasoni, P., Feldmann, H., Memmesheimer, M., Scheel, H., Trickl, T., Hübener, S., Ringer, W., and Mandl, M.: The influence of stratospheric intrusions on alpine ozone concentrations, *Atmos. Environ.*, 34, 1323–1354, 2000.
- Stohl, A., Bonasoni, P., Cristofanelli, P., Collins, W., Feichter, J., Frank, A., Forster, C., Gerasopoulos, E., Gäggeler, H., James, P., Kentarchos, T., Kromp-Kolb, H., Krüger, B., Land, C., Meloan, J., Papayannis, A., Priller, A., Seibert, P., Sprenger, M., Roelofs, G. J., Scheel, H. E., Schnabel, C., Siegmund, P., Tobler, L., Trickl, T., Wernli, H., Wirth, V., Zanis, P., and Zerefos, C.: Stratosphere-troposphere exchange: a review, and what we have learned from STACCATO, *J. Geophys. Res.*, 108, 2003.
- Stohl, A., Forster, C., Frank, A., Seibert, P., and Wotawa, G.: Technical note: The Lagrangian particle dispersion model FLEXPART version 6.2, *Atmos. Chem. Phys.*, 5, 2461–2474, 2005.
- Stohl, A., Aamaas, B., Amann, M., Baker, L. H., Bellouin, N., Berntsen, T. K., Boucher, O., Cherian, R., Collins, W., Daskalakis, N., Dusinska, M., Eckhardt, S., Fuglestvedt, J. S., Harju, M., Heyes, C., Hodnebrog, Ø., Hao, J., Im, U., Kanakidou, M., Klimont, Z., Kupiainen, K., Law, K. S., Lund, M. T., Maas, R., MacIntosh, C. R., Myhre, G., Myriokefalitakis, S., Olivie, D., Quaas, J., Quennehen, B., Raut, J.-C., Rumbold, S. T., Samset, B. H., Schulz, M., Seland, Ø., Shine, K. P., Skeie, R. B., Wang, S., Yttri, K. E., and Zhu, T.: Evaluating the climate and air quality impacts of short-lived pollutants, *Atmos. Chem. Phys.*, 15, 10 529–10 566, 2015.
- Tarasova, O. A., Senik, I. A., Sosonkin, M. G., Cui, J., Staehelin, J., and Prévôt, A. S. H.: Surface ozone at the Caucasian site Kislovodsk High Mountain Station and the Swiss Alpine site Jungfrauoch: data analysis and trends (1990–2006), *Atmos. Chem. Phys.*, 9, 4157–4175, 2009.
- Theil, H.: A rank-invariant method of linear and polynomial regression analysis, Part 3, in: *P. K. Ned. Akad. A Math.*, vol. 53, pp. 1397–1412, 1950.
- Thornes, J. E. and Stephenson, D. B.: How to judge the quality and value of weather forecast products, *Meteorol. Appl.*, 8, 307–314, 2001.

- Torres, M. E., Colominas, M. A., Schlotthauer, G., and Flandrin, P.: A complete ensemble empirical mode decomposition with adaptive noise, in: *Acoustics, speech and signal processing (ICASSP), 2011 IEEE international conference on*, pp. 4144–4147, IEEE, 2011.
- Trickl, T., Feldmann, H., Kanter, H.-J., Scheel, H.-E., Sprenger, M., Stohl, A., and Wernli, H.: Forecasted deep stratospheric intrusions over Central Europe: case studies and climatologies, *Atmos. Chem. Phys.*, 10, 499–524, 2010.
- Trickl, T., Vogelmann, H., Giehl, H., Scheel, H.-E., Sprenger, M., and Stohl, A.: How stratospheric are deep stratospheric intrusions?, *Atmos. Chem. Phys.*, 14, 9941–9961, 2014.
- Trickl, T., Vogelmann, H., Fix, A., Schäfler, A., Wirth, M., Calpini, B., Levrat, G., Romanens, G., Apituley, A., Wilson, K. M., Begbie, R., Reichardt, J., Vömel, H., and Sprenger, M.: How stratospheric are deep stratospheric intrusions? LUAMI 2008, *Atmos. Chem. Phys.*, 16, 8791–8815, 2016.
- Tung, K. and Yang, H.: Global QBO in circulation and ozone. Part II: a simple mechanistic model, *J. Atmos. Sci.*, 51, 2708–2721, 1994.
- ul-Haq, Z., Tariq, S., and Ali, M.: Tropospheric NO₂ trends over South Asia during the last decade (2004–2014) using OMI data, *Adv. Meteorol.*, 2015, 1–18, 2015.
- UNEP: Near-term climate protection and clean air benefits: actions for controlling short-lived climate forcers, Nairobi, Kenya, 2011.
- UNEP and WMO: Integrated assessment of black carbon and tropospheric ozone, Nairobi, Kenya, 2011.
- Voulgarakis, A., Hadjinicolaou, P., and Pyle, J.: Increases in global tropospheric ozone following an El Niño event: examining stratospheric ozone variability as a potential driver, *Atmos. Sci. Lett.*, 12, 228–232, 2011.
- Wang, G., Wang, H., Yu, Y., Gao, S., Feng, J., Gao, S., and Wang, L.: Chemical characterization of water-soluble components of PM₁₀ and PM_{2.5} atmospheric aerosols in five locations of Nanjing, China, *Atmos. Environ.*, 37, 2893–2902, 2003.
- Wernli, B. H. and Davies, H. C.: A Lagrangian-based analysis of extratropical cyclones. I: the method and some applications, *Q. J. R. Meteorol. Soc.*, 123, 467–489, 1997.
- Wernli, H. and Bourqui, M.: A Lagrangian “1-year climatology” of (deep) cross-tropopause exchange in the extratropical Northern Hemisphere, *J. Geophys. Res.*, 107, 2002.
- WHO: WHO Air quality guidelines for particulate matter, ozone, nitrogen dioxide and sulfur dioxide: global update 2005: summary of risk assessment, Geneva, Switzerland, 2006.

- Wilks, D. S.: *Statistical methods in the atmospheric sciences: an introduction, 2nd edition*, Academic press, 2006.
- WMO: WMO Global Atmosphere Watch (GAW) implementation plan: 2016–2023. GAW Report No. 228, Geneva, Switzerland, 2017.
- Wolter, K. and Timlin, M. S.: Monitoring ENSO in COADS with a seasonally adjusted principal component index, in: *Proc. of the 17th Climate Diagnostics Workshop*, pp. 52–57, 1993.
- Wotawa, G. and Kromp-Kolb, H.: The research project VOTALP—general objectives and main results, *Atmos. Environ.*, 34, 1319–1322, 2000.
- Xu, W., Lin, W., Xu, X., Tang, J., Huang, J., Wu, H., and Zhang, X.: Long-term trends of surface ozone and its influencing factors at the Mt. Waliguan GAW station, China—Part 1: overall trends and characteristics, *Atmos. Chem. Phys.*, 16, 6191–6205, 2016a.
- Xu, Y., Ramanathan, V., and Washington, W. M.: Observed high-altitude warming and snow cover retreat over Tibet and the Himalayas enhanced by black carbon aerosols, *Atmos. Chem. Phys.*, 16, 1303–1315, 2016b.
- Yasunari, T. J., Tan, Q., Lau, K.-M., Bonasoni, P., Marinoni, A., Laj, P., Ménégoz, M., Takemura, T., and Chin, M.: Estimated range of black carbon dry deposition and the related snow albedo reduction over Himalayan glaciers during dry pre-monsoon periods, *Atmos. Environ.*, 78, 259–267, 2013.
- Zeng, G. and Pyle, J. A.: Influence of El Nino Southern Oscillation on stratosphere/troposphere exchange and the global tropospheric ozone budget, *Geophys. Res. Lett.*, 32, 2005.

Acknowledgments

First of all, I would like to thank Dr. Paolo Cristofanelli for following me during the entire PhD project, for the constant support and all of the stimulating discussions that we had. Thanks also to Dr. Paolo Bonasoni, Dr. Angela Marinoni and Francescopiero Calzolari for the interest expressed in this project and for all of the suggestions given. Thanks to Mauro, Daniele, Angelo, Paolo, Maurizio, Boyan and all of the other guys at CNR-ISAC for the good moments spent, even outside of work.

Thanks to Dr. Michael Sprenger for being my tutor during my stay at the IAC-ETH, for the fruitful and valuable discussions, and for his kind assistance in the development of the STEFLUX tool. Thanks also to Prof. Heini Wernli, to Dr. Bojan Škerlak for the useful discussions when setting up the basis for STEFLUX, and to the whole atmospheric dynamics group and all the people that I met in Zurich, that made the whole stay an unforgettable experience.

This PhD project gave me the opportunity to share knowledge with a lot of national and international scientists: thanks to all of them for the inputs received and for being an active part of several collaborations.

Thanks to my parents, my brother and all of my friends, for the constant support and for always being there, even during the difficult times.

And, last but not least, thanks to Raffaella, because it wouldn't have been the same without her patience and support.